



### 저작자표시-비영리-변경금지 2.0 대한민국

이용자는 아래의 조건을 따르는 경우에 한하여 자유롭게

- 이 저작물을 복제, 배포, 전송, 전시, 공연 및 방송할 수 있습니다.

다음과 같은 조건을 따라야 합니다:



저작자표시. 귀하는 원 저작자를 표시하여야 합니다.



비영리. 귀하는 이 저작물을 영리 목적으로 이용할 수 없습니다.



변경금지. 귀하는 이 저작물을 개작, 변형 또는 가공할 수 없습니다.

- 귀하는, 이 저작물의 재이용이나 배포의 경우, 이 저작물에 적용된 이용허락조건을 명확하게 나타내어야 합니다.
- 저작권자로부터 별도의 허가를 받으면 이러한 조건들은 적용되지 않습니다.

저작권법에 따른 이용자의 권리와 책임은 위의 내용에 의하여 영향을 받지 않습니다.

이것은 [이용허락규약\(Legal Code\)](#)을 이해하기 쉽게 요약한 것입니다.

[Disclaimer](#)



공학박사학위논문

계면 에너지 구배로 발생하는 얇은  
액막 역학에 대한 연구

Dynamics of thin liquid films under gradient of  
interfacial energy

2016 년 2 월

서울대학교 대학원  
기계항공공학부  
김 승 호

계면 에너지 구배로 발생하는 얇은  
액막 역학에 대한 연구

Dynamics of thin liquid films under gradient of  
interfacial energy

지도교수 김 호 영

이 논문을 공학박사 학위논문으로 제출함

2016년 2월

서울대학교 대학원  
기계항공공학부  
김승호

김승호의 공학박사 학위논문을 인준함

2016년 2월

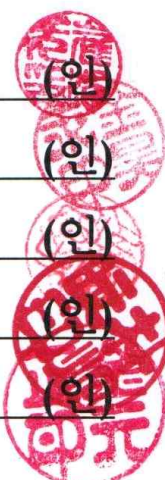
위 원 장 최 해 천 (인)

부 위 원 장 김 호 영 (인)

위 원 전 누 리 (인)

위 원 박 형 민 (인)

위 원 김 원 정 (인)



# Dynamics of thin liquid films under gradient of interfacial energy

Seungho Kim

Department of Mechanical Engineering  
Seoul National University

A thesis submitted for the degree of

*Doctor of Philosophy*

February 2016

## Abstract

Dynamics of thin liquid films under gradient of interfacial energy

Seungho Kim

Department of Mechanical Engineering  
The Graduate School  
Seoul National University

In the present thesis, we conducted hydrodynamic analysis of thin liquid films in the presence of gradients of interfacial energy, which were achieved by patterning wettability of a film-deposited solid surface or generating Marangoni stress on the free surface of thin liquid film. The first two phenomena resulted from gradient of the solid-liquid interfacial energy and the last one was attributed to that of the liquid-gas interfacial energy. We visualized such novel interfacial dynamics with a high-speed camera and rationalized their salient features by combining experimental and scaling analysis.

We first considered thin film behaviors under gradient of the solid-liquid interfacial energy, where the extreme wetting properties were coupled in such a way that a superhydrophilic annulus (region of low solid-liquid interfacial energy) was patterned on a superhydrophobic background (region of high solid-liquid interfacial energy). Drop impact on such a wettability-patterned surface showed that the drop initially spread on the

inner superhydrophobic region was arrested by the superhydrophilic annulus, leading to formation of thin liquid film, which we term a liquid lens. The liquid lens became destabilized because of the strong water repellence of the inner superhydrophobic region, exhibiting bursting of film on the superhydrophobic inner region. The bursting phenomena was initiated from nucleation of a tiny hole, whose size expanded with time. These bursting phenomena were so energetic that the film bounced off the inner superhydrophobic region by leaving liquid deposit on the pre-defined hydrophilic annulus, leading to the formation of a liquid ring. Here, we presented a theoretical consideration for predicting threshold volume of bursting and scaling laws for the bursting velocity, take-off angle of bouncing drop, and thickness of the liquid ring.

Next, we also investigated the effects of the solid-liquid interfacial energy gradient on the thin film, but we varied an injection method of the liquid. When we gently deposited liquid hanging from a capillary tube on the superhydrophilic line pattern, which was surrounded by superhydrophobic background, the liquid spread only along the superhydrophilic line, while superhydrophobic background maintained solid-gas contact mode. The spreading behaviors differed depending on the width of the superhydrophilic rails. For the narrow width of the hydrophilic rail, because of a high entrance resistance, which was inversely proportional to the width of the hydrophilic rail, a bulk liquid could not penetrate into the hydrophilic rail. Instead, the liquid started to wick into the nanostructures of the superhydrophilic substrate, thus leading to spreading of nanoscale film. For the wide width of the hydrophilic rail, the bulk liquid entirely infiltrated into the rail and spread along the hydrophilic region. A variety of power laws governing growth of the bulk front could be observed, such as  $x \sim t$ ,  $x \sim t^{1/4}$ , and  $x \sim t^{1/2}$ , with  $x$ ,  $t$  being

spreading distance, elapsed time, respectively. The power laws differed depending on the width of the hydrophilic rail, supplying pressure, and spreading extents. Here, we analyzed critical conditions for bulk film penetration by comparing the resisting pressure exerted on entrance region and supplying pressure generated by liquid column in capillary tube and we also suggested several power laws based on the physical understanding in each spreading regime.

Next, we analyzed the motion of thin liquid film under gradient of the liquid-gas interfacial energy. Here, we found that Marangoni stress on the water film was remotely triggered by alcohol liquid. When we placed alcohol liquid hanging from the capillary tube over water film, alcohol vapor emitted from the tube end condensed on water interface and changed water-air interfacial energy. Thus, although the alcohol liquid did not contact with water, the gradients of alcohol vapor generated the gradients of water-air interfacial energy, thereby leading to dewetting phenomena. The dewetting tendencies differed depending on the thickness of the deposited water film. For a thin water film, the thickness of the dewetting film was separated into two different regimes: where the bulk part immediately receded owing to the gradients of the water-liquid interfacial energy due to the alcohol vapor, and the nanoscale fringe film was dewetted by spontaneous evaporation. For a thick liquid film, dewetting did not occur continuously but had a maximum dewetting distance where the gravitational force was balanced with the interfacial energies and capillary forces, both of which were induced by the gradients of the alcohol vapor. Here, we presented scaling laws for the dewetting velocity of thin water film and the degree of maximum radius of thick water film by analyzing dewetting motions of deposited water film.

This thesis provided three noble phenomena of thin film such as bursting, spreading, and dewetting, and their salient hydrodynamic features in the presence of interfacial energy gradient. Based on such phenomena, we demonstrated that liquid deposits could be manipulated to achieve certain morphologies. By using gradients of the solid-liquid interfacial energy, we showed that the shape of liquid could be rapidly patterned on solid surface via bursting and spreading phenomena. The gradient of liquid-gas interfacial energy could puncture liquid film on solid surface and make a hole on it, whose size could be determined depending on the thickness of liquid film. Thus, This thesis will not only be helpful in understanding roles of interfacial energy gradient in thin liquid film, but also provide practical implications related to rapid liquid and hole patterning fields, which have potential applications in printed electronics.

Keywords :Thin film, capillarity, interfacial tension, Marangoni, hole, bursting, rupture, wetting, dewetting, spreading

Student Number : 2010-20659

# Contents

<b>Abstract</b>	<b>i</b>
<b>Contents</b>	<b>v</b>
<b>List of Figures</b>	<b>vii</b>
<b>1 Introduction</b>	<b>1</b>
1.1 Overview . . . . .	1
1.2 Backgrounds & motivations . . . . .	2
<b>2 Drop impact on super-wettability-contrast annular patterns</b>	<b>8</b>
2.1 Introduction . . . . .	8
2.2 Experiments . . . . .	10
2.3 Types of drop impact behavior . . . . .	12
2.4 Film bursting, liquid ejection, and water ring . . . . .	18
2.5 A practical implication . . . . .	28
2.6 Conclusions . . . . .	29
<b>3 Liquid spreading along wettable rails</b>	<b>31</b>
3.1 Introduction . . . . .	31
3.2 Experimental apparatuses . . . . .	33
3.3 Liquid spreading along microstripes . . . . .	34
3.4 Spreading with thin precursor film . . . . .	36
3.5 Spreading with bulk film . . . . .	39
3.5.1 Inertial regime . . . . .	40
3.5.2 Capillary bending regime . . . . .	41

---

## CONTENTS

3.5.3	Viscous spreading regime . . . . .	47
3.5.4	Characteristic time of bifurcation . . . . .	50
3.6	Conclusions . . . . .	52
<b>4</b>	<b>Dewetting of liquid film via vapor-mediated Marangoni effect</b>	<b>55</b>
4.1	Introduction . . . . .	55
4.2	Experiments . . . . .	57
4.3	Variation in interfacial tension with alcohol vapor . . . . .	58
4.4	Types of dewetting behavior . . . . .	62
4.5	Thin film regime . . . . .	67
4.6	Thick film regime . . . . .	72
4.7	Conclusions . . . . .	76
<b>5</b>	<b>Concluding remarks</b>	<b>78</b>
5.1	Conclusions . . . . .	78
5.2	Future work . . . . .	81
<b>A</b>	<b>Dynamic thickness of bulk film</b>	<b>82</b>
<b>B</b>	<b>Relation between alcohol vapor and liquid-gas interfacial tension</b>	<b>86</b>
<b>C</b>	<b>Distribution of alcohol vapor emitted from source in spherical coordinates</b>	<b>88</b>
<b>References</b>		<b>90</b>
<b>Abstract (in Korean)</b>		<b>98</b>

# List of Figures

1.1	Morphologies of thin liquid films under homogeneous wettability surfaces. (a) Circular liquid film on a flat surface (Tanner, 1979). (b) Polygonal liquid film on a microtextured surface (Courbin <i>et al.</i> , 2007).	3
1.2	Morphologies of thin liquid films under nonhomogeneous wettability surfaces. (a) Liquid filaments flowing along a hydrophilic stripe. (Ledesma-Aguilar <i>et al.</i> , 2011). (b) Spreading of silicon oil film only on a hydrophilic region (Kataoka & Troian, 1999). (c) Liquid arms radiating from a center (Lee <i>et al.</i> , 2010). (d) Patterning of liquid deposit only along a hydrophilic region (Darhuber <i>et al.</i> , 2000). (e) Liquid annulus and lens formation with a help of hydrophilic annulus (Jokinen <i>et al.</i> , 2008).	4
2.1	Fabrication process of the surface with extreme wettability contrast.	11
2.2	Scanning electron microscopy (SEM) image of nanograsses formed on a PET substrate.	11
2.3	Different types of drop impact behavior. (a) Rebound for $R_m < R_i$ . (b) Lens formation for $R_i < R_m < R_o$ . (c) Lens rupture, droplet ejection, and generation of a ring for $R_m > R_o$ . $[R_i, R_o] = [4.0, 4.2], [2.5, 7.5]$ and $[5.0, 5.2]$ mm for (a), (b) and (c), respectively. The impact Weber number $We=25$ and 106 for (a, b) and (c), respectively.	14

---

## LIST OF FIGURES

- 2.4 Temporal evolution of the base radius of a water drop with the initial radius  $a=1.3$  mm impacting with the speed of  $U = 1.2 \text{ m s}^{-1}$  on a uniformly superhydrophobic surface (triangles) and a wettability-patterned surface with  $R_i = 2.5$  mm (circles). . . . . 15
- 2.5 Air bubble entrainment during spreading. (a) Schematic process of entrainment of air due to instability of the contact line advancing on the hydrophobic surface and abrupt encounter of the hydrophilic region. The abrupt switch of the contact mode at the annular region from that of Cassie-Baxter to Wenzel occurs between the second and third panels, by which a large bubble is trapped. The large bubble formed at the wettability boundary (the third panel) moves into the superhydrophobic region because of a strong affinity for gas and liquid of the superhydrophobic and superhydrophilic region, respectively. In the last panel, the contact line has receded back to  $R = R_o$ . (b) Magnified images near the wettability boundary visualizing the formation process of air bubbles illustrated in (a). The times are measured from the moment that the drop hits the substrate. The dashed lines correspond to the inner and outer edges of the wettable annulus. The liquid front advances from the upper left to the lower right. In the last panel (10.73 ms), the small bubbles inside the inner wettability boundary are distinguished from the irregularly shaped large bubbles at the wettability boundary. . . . . 17
- 2.6 Bursting of a thin lens due to decrease of volume by evaporation, which eventually leads to the formation of a liquid ring. A bubble (indicated by an arrow) entrained in a liquid film at 0 ms generates a hole, which is detected by a high-speed camera in the next frame (0.1 ms). . . . . 19

## LIST OF FIGURES

---

## LIST OF FIGURES

---

3.1	(a) Scanning electron microscopy (SEM) image of nanograsses formed on a silicon wafer. The inset is a side view of the substrate. (b) Experimental apparatuses for letting a liquid flow along a hydrophilic rail. . . . .	35
3.2	Liquid spreading on superhydrophilic rails. (a) Thin film spreading for $[w, h_{L,o}] = [0.4, 28.5]$ mm. (b) Thick film spreading for $[w, h_{L,o}] = [0.8, 33.2]$ mm. In the first panels of (a, b), The dashed lines correspond to the edges of hydrophilic rails. The liquid front spreads along the predefined hydrophilic rail when the liquid hanging from a capillary tube is brought into contact with a hydrophilic surface. (c) Linear and (d) log-log plot of experimentally measured spreading extents $x$ versus time $t$ . . . . .	37
3.3	(a) Propagation of a thin precursor film emerging from a bulk liquid beneath the capillary tube. (b) Magnified view of the precursor film spreading corresponding the dashed box in the sixth panel of a. The liquid front penetrates into the gaps of the nanopillars by forming sharp protrusions at the contact line. . . . .	38
3.4	(a) Log-log plot of experimentally measured spreading extents of a precursor film $x - x_b$ versus time $t$ . (b) The scaled spreading distance, $(x - x_b)/h_p$ plotted according to the scaling law. Here, $T_{p,v}$ is the viscous-capillary time scale, which is defined as $\mu h_p/\gamma$ by using the characteristic length of hemi-wicking, $h_p$ . . . . .	38
3.5	Critical boundary between thin precursor film and bulk film spreadings. . . . .	40
3.6	Side view of early film spreading in an inertia dominant stage for $[w, h_{L,o}] = [1.0, 38.4]$ mm. . . . .	41
3.7	Schematic model for describing inertial film spreading. . . . .	41

---

## LIST OF FIGURES

---

3.8 Spreading extents of bulk film $x$ versus time $t$ (a) Linear plot. (b) Scaled spreading extents $x/h_p$ versus scaled spreading time $(f - 1)^{1/2}t/T_{p,i}$ plotted according to the scaling law, where $T_{p,i}$ is the inertial-capillary time scale, which is defined as $(\rho h_p^3/\gamma)$ . . . . .	42
3.9 Schematic profile of spreading film. The capillary tube influences the film profile near the tube, thus forming highly curved meniscus region (static region). Above the static region, the film is stretched by advancing front, thus leading to relatively constant film thickness (dynamic region). . . . .	43
3.10 High-speed imaging results of film spreading in the capillary bending regime. As time elapses, the curvature near the capillary tube end (dashed circle) is relaxed by forming smooth meniscus between a ridge of liquid film and the tube end. . . . .	45
3.11 Spreading extents of bulk film in capillary bending regime. (a) Log-log plot. (b) The scaled spreading distances $x/h_f$ plotted according to the scaling law, where $T_f$ is viscous-capillary time scale, $\mu h_f/\gamma$ . . . . .	46
3.12 Comparison of spreading behaviors depending on the types of substrates. (a) The spreading extents $x$ versus time for $[w, h_{L,o}] = [0.8, \sim 35]$ mm. The inset shows spreading of film on a prewetted surface whose thickness is measured to be $\sim 4 \pm 2 \mu\text{m}$ . The scaled spreading extents $x/a$ plotted according to the scaling law (b) without considering $\Gamma$ and (c) with considering $\Gamma$ . . . . .	48
3.13 High-speed imaging results of film spreading in the viscous spreading regime for $[w, h_{L,o}] = [1.2, 29.2]$ mm. A bulk film is prewetted by a precursor film, as shown in the dashed box in the third panel. The distance between the bulk and precursor film can be neglected due to the its small length and growth rate. . . . .	48

---

## LIST OF FIGURES

---

3.14 (a) Log-log plot of spreading extents $x$ versus time $t$ in viscous spreading regime. (b) The scaled spreading extents $xw/h_f^2$ plotted according to the scaling law. . . . .	49
3.15 The scaled spreading extents $x/a$ plotted according to the scaling law depending on the characteristic of surfaces. . . . .	50
3.16 Log-log plots of (a) the scaled characteristic inertia-bending time $\tau_{i,b}/T_{i,b}$ versus dimensionless film thickness $h_f/R_c$ and (b) the scaled characteristic bending-spreading time $\tau_{b,s}/T_{b,s}$ versus aspect ratio of film $w/h_f$ and (c) the scaled characteristic inertia-spreading time $\tau_{i,s}/T_{i,s}$ versus aspect ratio of film $w/h_f$ . . . . .	51
3.17 The dependence of $w$ on time scale of characteristic spreading. (a) $h_{L,o} = 37$ mm. (b) $h_{L,o} = 33$ mm. As $w$ decreases, viscous spreading is retarded. . . . .	52
4.1 (a) Experimental devices to measure the interfacial tension between liquid and gas with different IPA vapor concentrations, where $h_G$ is the gap distance between the IPA free surface and water surface. (b) Swelling of the water balloon with increasing IPA vapor concentration at $h_G = 22$ mm. (c) Shrinking of water drop on the substrate at $h_G = 35$ mm	58
4.2 (a) Liquid-gas interfacial tension $\gamma/\gamma_o$ versus IPA vapor concentration $c/c_s$ . (b) Contact angle $\theta$ of water drop within mixture of IPA vapor and air $\theta$ versus IPA vapor concentration $c/c_s$ . . . . .	61
4.3 Different types of film dewetting driven by Marangoni effect (a) $h \simeq 30 \mu\text{m}$ . (b) $h \simeq 50 \mu\text{m}$ . (c) $h \simeq 270 \mu\text{m}$ . . . . .	64
4.4 (a) Diffusion contour of IPA molecules emitted from tube end at $[t, h_G] = [5 \text{ s}, 3 \text{ mm}]$ . The time was measured after the IPA molecules were allowed to diffuse out of the tube end. (b) Comparison between diffusion profiles calculated with numerical and theoretical models. . . . .	65

---

## LIST OF FIGURES

---

4.5 Dewetting of thin film regime with $h_o \simeq 30 \mu\text{m}$ . Temporal evolution of dewetting radius of bulk film ( <i>a</i> ) and fringe film ( <i>b</i> ) . . . . .	68
4.6 The radius of bulk film, $r_b$ versus time plotted according to the our scaling law. . . . .	70
4.7 The profile of fringe film corresponding to $t - t_d = 1.0 \text{ s}$ (squares), $2.3 \text{ s}$ (circles), $5.0 \text{ s}$ (triangles), and $7.5 \text{ s}$ (diamonds). . . . .	71
4.8 The radius of bulk film, $r_f$ versus time plotted according to the our scaling law. . . . .	72
4.9 The growth of hole radius $r_B$ versus time. ( <i>a</i> ) The differences of hole growth depending on the initial film thickness. ( <i>b</i> ) Hole growth at $h_o = 290 \mu\text{m}$ , where the power laws of hole radius change from $r_B \sim t$ to $r_B \sim t^{1/2}$ . . . . .	73
4.10 ( <i>a</i> ) Early-stage growth of hole radius $r_B$ versus time plotted according to the our scaling law. ( <i>b</i> ) Late-stage growth of the scaled hole radius $r_B/(h_c - h_o)$ versus time plotted according to the our scaling law. . . . .	74
4.11 ( <i>a</i> ) Dewetting of thick film with $h_g = 2 \text{ mm}$ for different initial film thicknesses. The arrows indicate the moment that the source of the IPA vapor was detached. ( <i>b</i> ) Log-log plot of the scaled maximum hole radius $l_c/r_{B,m}$ versus film thickness plotted according to the our scaling law. . . . .	76
A.1 Schematic of spreading film emitting from a tube on hydrophilic microstripe. A curved and relatively flat meniscus are formed depending on a spreading extents $x$ , and thus static, dynamic, and overlap region is existed. . . . .	83
A.2 Log-log plot of ( <i>a</i> ) dimensional film thickness $h_f$ plotted according to capillary number $Ca$ , and ( <i>b</i> ) the scaled film thickness $h_f(h_L - h_J)/l_c^2$ plotted according to the scaling law. Plot legends as in the bottom. . . . .	85

## LIST OF FIGURES

## List of Tables

# Chapter 1

## Introduction

### 1.1 Overview

The main target of this thesis is to analyze novel findings of liquid film behaviors under the gradient of interfacial energy, which give rise to dynamic motions of the film. We first mention research backgrounds & motivations, and then we deals with the present studies, which are distinguished into two parts. The first part deals with thin film hydrodynamics subjected to the gradient of interfacial energy exerted on the liquid-solid interface, and the second part does on the liquid-gas interface.

In the first part, we cover the dynamics of thin liquid film on the wettability-patterned surface where the region of the low liquid-solid interfacial energy is patterned on the background region of the high liquid-solid interfacial energy, which will be listed in chapter 2 and 3. In chapter 2, we use drop impact technique for making thin film on the wettability-patterned surface where the superhydrophilic annulus (low liquid-solid interfacial energy) is surrounded by superhydrophobic background (high liquid-solid interfacial energy). Abilities of film formation via drop impact on the surface are employed and hitherto unreported behaviors of thin liquid film are reported, such as spontaneous film bursting and ejection followed by liquid annulus formation. In chapter 3, we deals with thin film spreading when we gently deposit liquid on a superhydrophilic region among the wettability-

## **1.2 Backgrounds & motivations**

---

patterned surface. Spreading abilities and velocities are discussed depending on the experimental conditions such as width of the superhydrophilic strips, supplying pressure, and liquid properties.

In the second part, we suggest the behaviors of thin liquid film in the presence of the gradient of liquid-gas interfacial energy. Here, we find a method of inducing dewetting motion of stationary liquid film by using vapor-mediated Marangoni effect. Then, we analyze the dewetting motions of thin film depending on the deposited film thickness, which will be in chapter 4.

In the end of this thesis, we conclude this thesis with concluding remarks in chapter 5, where we provide the summary of these researches and practical aspects.

## **1.2 Backgrounds & motivations**

A thin liquid film consists of a layer of liquid, whose thickness ranges between a nanometer and several hundred micrometers. Such thin liquid films can be formed by depositing a small liquid drop on the wettable solid surface. Several power laws have been proposed to predict the increase of spreading radius of deposited drop with time (Biance *et al.*, 2004; Huppert, 1982; Lopez & Miller, 1976; Tanner, 1979). Thin liquid films can also be produced by withdrawing the solid substrates out of stationary liquid. Starting from the first experimental study (Goucher & Ward, 1922), Derjaguin (1943); Landau & Levich (1942, 1962) developed the classical Landau-Levich-Derjaguin formula,  $h \sim Ca^{2/3}$ , where  $h$  and  $Ca$  are the thickness of deposited film and capillary number  $\mu U_w / \gamma$ . Here,  $\mu$ ,  $\gamma$ , and  $U_w$  are liquid viscosity, surface tension, and withdrawn velocity, respectively. Later, the previous model has been modified to cover the whole range of  $Ca$  (de Ryck & Quéré, 1996; Quéré, 1999; Teletzke *et al.*, 1988) and the effects of substrate texture (Seiwert *et al.*, 2011). The deposited thin liquid films on the solid surface were usually vulnerable to the disturbance that could lead to a nucleation of a hole. Taylor & Michael (1973) presented

## 1.2 Backgrounds & motivations

---

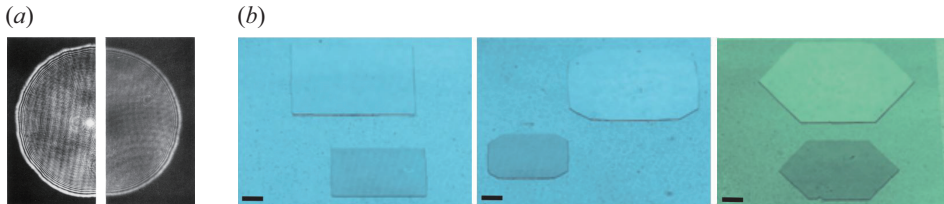


Figure 1.1: Morphologies of thin liquid films under homogeneous wettability surfaces. (a) Circular liquid film on a flat surface (Tanner, 1979). (b) Polygonal liquid film on a microtextured surface (Courbin *et al.*, 2007).

theoretical model for the rupture depending on the degree of exerted disturbance. Spontaneous film rupture via decreasing the film thickness have also been discussed (Padday, 1970; Sharma & Ruckenstein, 1989). Once the hole emerges, thin liquid films easily dewet to minimize the surface area exposure of liquid films (de Gennes *et al.*, 2004). The dewetting velocities have been extensively discussed, depending on the exerted driving, resisting force, and the film thickness (Culick, 1960; Redon *et al.*, 1991; Reiter, 1992; Taylor, 1959).

Thus, the researches ranging from the formation to the rupture of thin film have been the subject of intense study for last century, but the hydrodynamic analysis of thin film shape has been studied only for a few decades. Besides a circular liquid film, which is usual final shape of spreading droplet on a flat surface, as shown in figure 1.1(a), recent studies have showed that the shape of liquid films could be tailored by designing micropillar arrays on the solid surface, where the detailed film shape depended on the spacing and dimensions of pillars, as shown in figure 1.1(b), (Bico *et al.*, 2001; Courbin *et al.*, 2007; Kim *et al.*, 2011a; Sbragaglia *et al.*, 2007). Limitations still occur in obtaining complex morphologies of liquid films, which is important characteristics in the lab-on-a-chip (Zhang, 2011), lab-on-paper technologies (Li *et al.*, 2014), and printed electronics (Russo *et al.*, 2011).

Complicated shape of liquid films can be achieved on the surface with a nonhomogeneous wettability surface in such a way that hydrophilic regions are selectively patterned on a hydrophobic region, as shown in figure 1.2.

## 1.2 Backgrounds & motivations

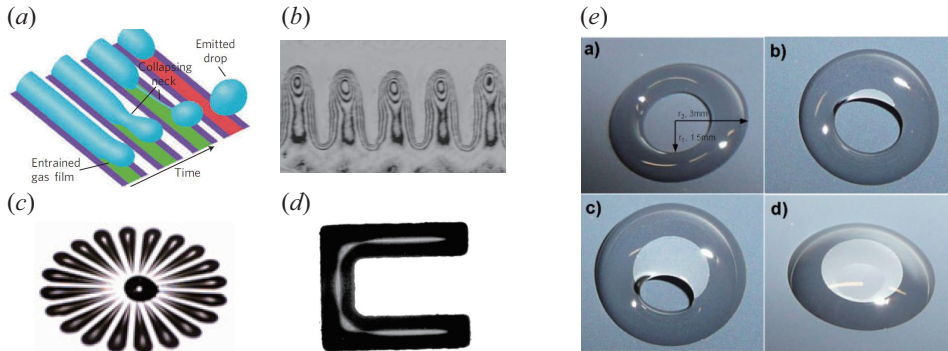


Figure 1.2: Morphologies of thin liquid films under nonhomogeneous wettability surfaces. (a) Liquid filaments flowing along a hydrophilic stripe. (Ledesma-Aguilar *et al.*, 2011). (b) Spreading of silicon oil film only on a hydrophilic region (Kataoka & Troian, 1999). (c) Liquid arms radiating from a center (Lee *et al.*, 2010). (d) Patterning of liquid deposit only along a hydrophilic region (Darhuber *et al.*, 2000). (e) Liquid annulus and lens formation with a help of hydrophilic annulus (Jokinen *et al.*, 2008).

Ledesma-Aguilar *et al.* (2011) demonstrated a gravity-driven flow guided along a wettable stripe bounded by a nonwettable medium that remained dry, thereby leading to the filament shape of liquid film, as shown in figure 1.2(a). A more sophisticated film morphologies were gained via complex wettability-patterned surfaces (Darhuber *et al.*, 2000, 2001; Kataoka & Troian, 1999; Lee *et al.*, 2012, 2010). Kataoka & Troian (1999) showed finger shapes of liquid film on alternating stripes of hydrophilic and hydrophobic region, which are thermally manipulated, as shown in figure 1.2(b). Thin liquid microarms radiating from a center were generated by impact of drop (Lee *et al.*, 2010) and a U-shape of liquid film was drawn by withdrawing the wettability-patterned surface out of liquid (Darhuber *et al.*, 2000), as shown in figure 1.2(c, d). Thus, patterns of wettability easily control the shape of the deposited film by letting the film deposit only on the hydrophilic region, but a problem arose from drawing liquid on hydrophilic closed curve surrounded by hydrophobic background, as shown in figure 1.2(d). Jokinen *et al.* (2008) showed that a liquid ring was suc-

## 1.2 Backgrounds & motivations

---

cessfully drawn by injecting multiple droplet on the hydrophilically treated annulus, but it was transformed into a liquid lens with increasing the volume of the liquid ring, leading to the failure of liquid patterning only on the hydrophilic annulus, where the liquid film covered the inner hydrophobic circle.

Besides the shape control, wettability-patterned surface also brings about intriguing hydrodynamic behaviors due to the complex morphologies of liquid films. Ledesma-Aguilar *et al.* (2011) suggested that the liquid filament was destabilized to generate the periodic emission of droplets when the velocity of filament flowing down the stripe exceeded a critical wetting velocity, which was expected to be  $U^* \sim \gamma(\pi - \theta_A)^3/\mu$  (Duez *et al.*, 2007), with  $\theta_A$  being the advancing contact angle of liquid filament. The size and location of emitted droplet were precisely controlled by changing the geometries of the wettable stripes and  $U^*$  and such abilities was not acquired from the homogeneous wettability surface, where the roughened contact line was observed even when the velocity of advancing film was larger than  $U^*$  (Blake & Ruschak, 1979; Eggers, 2004). Darhuber *et al.* (2000) showed that the thickness of withdrawing film on the wettable microstripe differed from that on the chemically homogeneous surface. They considered the width of microstrip,  $w$ , and developed the following model,  $h \sim wCa^{1/3}$ , which was in slight disagreement with the aforementioned Landau-Levich-Derjaguin model due to the effect of lateral confinement of the film. Darhuber *et al.* (2001) presented the model for spreading liquid film on the wettable stripe,  $x \sim \sqrt{\gamma w^4/\mu t^{1/2}}$ , where  $x$  and  $t$  are the spreading extents and time, respectively. The power law slightly disagreed with the spreading on the chemically homogeneous surface (Biance *et al.*, 2004; Huppert, 1982; Lopez & Miller, 1976; Tanner, 1979). Lee *et al.* (2010) showed that the finger growth at the film edge was manipulated by the chemically modified patterns and Lee *et al.* (2012) suggested that the condensed water film was effectively drained with a help of wettable pattern.

Thus, we started the present researches to reveal the salient features of thin liquid film and analyze the hydrodynamics of the characteristics

## 1.2 Backgrounds & motivations

---

on the nonhomogeneous wettability surface for achieving the tailored film morphologies toward direct printing of microscale liquid.

We first consider thin film behaviors on the wettability-coupled surface that a superhydrophilic annulus is surrounded by superhydrophobic backgrounds. Here, we discuss the abilities of thin film formation depending on the impacting conditions of a liquid drop and the rupture dynamics of the deposited film, which lead to the formation of a liquid ring defined by the wettable annulus pattern. Based on this study, we can directly print the thin liquid film even if the wettable curve is closed, which can be extended to print liquid on a rectangular wettable loop. The dynamics of the rupture threshold, speed, and the associated phenomena will be discussed in chapter 2.

Thin liquid film can be printed by using spreading phenomena as mentioned earlier, and thus we deal with the spreading abilities on the wettability-patterned surface in chapter 3. Here we use an elementary wettable geometry to reveal fundamental dynamics of spreading on the wettability-patterned surface, where the superhydrophilic microstripe is patterned on superhydrophobic background. We observe the different spreading behaviors depending on the width of the wettable stripe, which slightly differs from the previous study (Darhuber *et al.*, 2001). We show that a bulk film does not penetrate into the wettable rail for the narrow wettable stripe, but for the wide wettable stripe and a variety of power laws are engaged in the spreading. Thus, we analyze such spreading dynamics and develop the several models to predict the velocity of spreading in chapter 3.

Those two studies focus on the thin film behaviors on the wettability-patterned surface, where we control the liquid-solid interfacial energy on the solid surface. Next, we deal with another liquid patterning method, which is manipulated under the nonhomogeneous interfacial energy on the liquid-gas interface. Previously, a contactless movement of liquid drops has been experimentally observed (Bahadur *et al.*, 2009; Bangham & Sawyer, 1938; Carles & Cazabat, 1989), but Cira *et al.* (2015) recently showed that a volatile vapor generated the gradient of the liquid-gas interfacial energy

## **1.2 Backgrounds & motivations**

---

and caused the motion of droplets. Based on those studies, we find that the vapor emitted from alcohol liquid can vary the water-air interfacial energy and thus induce a dewetting motion of a water film despite the noncontact of two liquids, leading to a hole patterning in the liquid film. The size of the hole are closely related to the thickness of the deposited water film. The high-speed imaging of the hole formation and the the detailed dewetting dynamics will be discussed in chapter 4.

In the end, we finalize this thesis with concluding remarks in chapter 5. We anticipate this thesis to provide inspiration on the physics of thin film flow under the nonhomogeneous interfacial energies and also expect that these researches can be applied to direct printing of microliquid and analysis of tear film rupture, which will be concretely explained in chapter 5.

# Chapter 2

## Drop impact on super-wettability-contrast annular patterns

### 2.1 Introduction

Although the drop impact on solid surfaces has been a subject of intense study for more than a century (Rein, 1993; Worthington, 1877; Yarin, 2006), the hydrodynamic analysis of liquid drop behavior on surfaces with extreme wettability conditions, whether superhydrophobic or superhydrophilic, began only recently (Clanet *et al.*, 2004; Ishino *et al.*, 2007; Kim *et al.*, 2011a; Tsai *et al.*, 2009). In general, the wettability of microscopically rough surfaces is magnified compared to that of smooth surfaces, thus rough hydrophobic (hydrophilic) surfaces become superhydrophobic (superhydrophilic). The tailored topography of solid surfaces as well as wide range of wettability, made possible thanks to recent developments of micro- and nanofabrication technology, has enabled the formation of some novel liquid deposit shapes. On superhydrophobic surfaces, a water drop retains an almost spherical shape (Onda *et al.*, 1996), whereas superhydrophilic surfaces cause drops to wick through the surface protrusions, resulting in an extremely thin film (Quéré, 2008). In addition to axisymmetric de-

## 2.1 Introduction

---

positis, polygonal spreading was observed on micropillar arrays with the detailed shape depending on the pillar wettability, distribution and dimensions (Bico *et al.*, 2001; Courbin *et al.*, 2007; Cubaud & Fermigier, 2001; Sbragaglia *et al.*, 2007). Still, limitations exist in achieving complicated morphologies of liquid deposit, which play important roles in the lab-on-a-chip technology (Zhang, 2011) and printable electronics (Russo *et al.*, 2011).

Besides the surface topography, patterns of wettability can control the shape of a liquid deposit. Kataoka & Troian (1999) demonstrated a thermocapillary flow guided along a hydrophilic lane while the neighbouring hydrophobic region remained dry. Zhao *et al.* (2001) realized liquid streams following virtual conduits of hydrophilic lines inside microchannels. Jokinen *et al.* (2008) showed that a sessile drop containing an air bubble in its interior can be generated on a superhydrophobic surface with a wettable annular pattern by slowly increasing the deposit volume. Thin spokes or narrow fans of liquids radiating from a centre were generated by drop impact on the surface with microscale wettability patterns (Lee *et al.*, 2010). These previous studies show that patterning the wettability of solid surfaces can provide a fairly sophisticated way to controlling the drop morphology.

Here we investigate the dynamic behavior of a drop impacting on super-wettability-contrast patterns where a wettable annulus is surrounded by superhydrophobic background to effectively combine the aforementioned capabilities of extreme wettability conditions and of microwetting patterns in deposit shape control. We find hitherto unreported drop dynamics, such as spontaneous film rupture followed by liquid ejection and water annulus formation, which may lead to novel microfluidic applications. In the following, we start with description of experimental procedures and then report the observation of different behaviors of liquid drops on the annular wettability patterns depending on the impact conditions and the annulus dimensions. We then provide hydrodynamic analysis for several salient features in the process. Finally we demonstrate the practical implications of the phenomena investigated here.

## 2.2 Experiments

---

### 2.2 Experiments

We use PET (polyethylene terephthalate) substrates to fabricate super-water-repellent surfaces with wettable annular patterns. We first clean the substrate with Ar gas and then follow the steps illustrated in figure 2.1. We create nanoscale roughness on the surface through O<sub>2</sub> etching in a plasma-assisted chemical vapor deposition (PACVD) chamber for 30 min. Then it is coated with an amorphous C<sub>6</sub>H<sub>18</sub>Si<sub>2</sub>O film using hexamethyl-disiloxane (HMDSO) gas via PACVD process. For detailed conditions of the plasma process, see Shin *et al.* (2012). (Shin *et al.*, 2012) The resulting surface is covered with nanograsses as shown in figure 2.2, and the root-mean-square (RMS) surface roughness is measured to be 150 nm with 5.3% of standard deviation by scanning area of 25  $\mu\text{m}^2$  using an atomic force microscope (Park Systems XE-70). The surface roughness, defined as the ratio of the actual surface area to the projected area, is 1.8. To selectively hydrophilicize an annular area, the surface is spin-coated with a photoresist (AZ 1512) and exposed to ultraviolet radiation with a photomask on it. After removing the irradiated photoresist region with a developer, the photoresist-patterned substrate is treated with air plasma, which makes the exposed area superhydrophilic (Kim *et al.* 2011b). Finally, removing the residual photoresist with acetone, we are left with a surface with extreme wettability contrast: superhydrophilic in the air-plasma-treated annulus and superhydrophobic elsewhere. We vary the size of the annulus so that the inner radius  $R_i$  ranges between 1.5 and 5.0 mm and the outer radius  $R_o$  between 2.0 and 7.5 mm. By imaging water drops of 2  $\mu\text{l}$  volume, the static contact angle  $\theta_s$  of the superhydrophilic and the superhydrophobic surface is measured to be nearly zero and  $160 \pm 2^\circ$ , respectively. The critical advancing contact angle,  $\theta_a$ , and the critical receding contact angle,  $\theta_r$ , of the superhydrophobic surface are measured by increasing ( $\theta_a$ ) or decreasing ( $\theta_r$ ) the drop volume until the contact line starts to move with an aid of a syringe needle immersed in the drop (de Gennes *et al.*, 2004). Then we find the contact angle hysteresis,  $\theta_a - \theta_r$ , to be  $5^\circ \pm 2^\circ$ .

## 2.2 Experiments

---

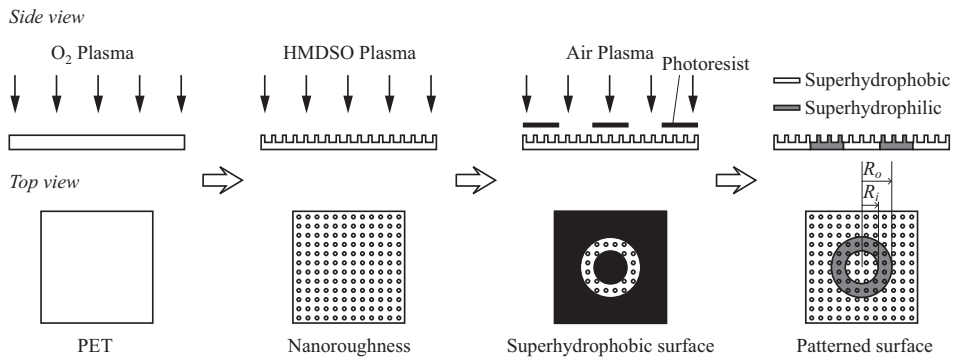


Figure 2.1: Fabrication process of the surface with extreme wettability contrast.

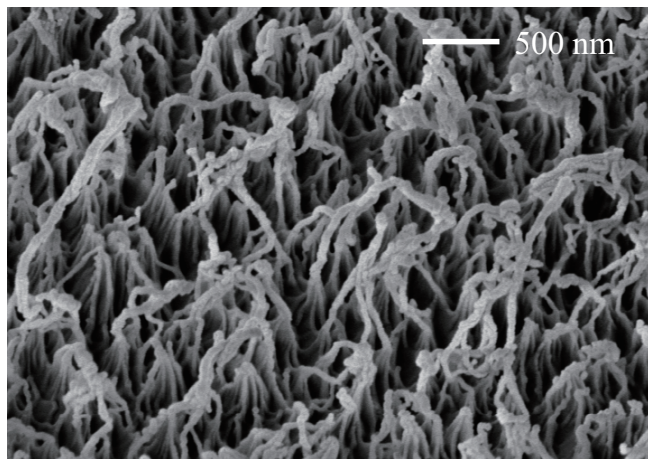


Figure 2.2: Scanning electron microscopy (SEM) image of nanograsses formed on a PET substrate.

### **2.3 Types of drop impact behavior**

---

We use deionized water emitting from a micropipette to create liquid drops of radius  $a$  ranging between 1.2 and 1.9 mm. They fall under gravity to impact on the horizontal surface. They hit the center of superhydrophobic region surrounded by the annulus. The impact velocity of a drop,  $U$ , is varied by changing the distance it travels:  $U$  ranges between 0.44 and 2.65  $\text{m s}^{-1}$ . The shape evolution of the drop is recorded by a high-speed camera (Photron Fastcam SA1.1) at a rate ranging between 3000 and 20000 frames per second with the pixel resolution of  $512 \times 512$ . In the experiments, the substrate is located on the precision balance (Mettler Toledo XS205) to measure the temporal change of drop mass. We deduce the thickness of a thin liquid lens from its mass assuming that the lens is a part of sphere due to negligible gravitational effects.

## **2.3 Types of drop impact behavior**

Figure 2.3 shows different types of drop impact behavior depending on how a liquid drop interacts with the hydrophilic annulus surrounded by the super-water-repellent background. The effects of the hydrophilic region manifest themselves only when the maximum spread radius of the drop,  $R_m$ , is greater than  $R_i$ . We first varied  $R_i$  and  $R_o$ , while the drops of  $a = 1.3$  mm have the impact velocity  $U = 1.2 \text{ m s}^{-1}$  and  $2.5 \text{ m s}^{-1}$  for (a, b) and (c), respectively. Thus, the Weber number  $We = \rho U^2 a / \gamma = 25$  and 106 for (a, b) and (c), respectively. Here  $\rho$  is the liquid density and  $\gamma$  the surface tension. The corresponding Reynolds numbers  $Re_a = \rho U a / \mu$ , with  $\mu$  being the viscosity, are 1560 and 3250 for (a, b) and (c), respectively. Clanet *et al.* (2004) showed that it is the parameter  $P = 1.15 We / Re_a^{4/5}$  that determines whether the impact inertia is balanced by the interfacial tension or the viscosity. In our cases with  $P$  being much smaller than unity, the drop impact is in the capillary regime where the drop inertia is balanced with the interfacial tension.

For  $R_m < R_i$ , figure 2.3(a), the water drop recoils and eventually disengages from the super-water-repellent area upon reaching the maximum

### **2.3 Types of drop impact behavior**

---

radius  $R_m = 3.1$  mm, which is typical of drops with  $We \in [0.1 - 30]$  (Rioboo, 2008). In this  $We$  range,  $R_m$  is determined by the balance of inertia of the decelerated drop with the interfacial tension as  $R_m/a \sim We^{1/4}$  (Clanet *et al.*, 2004).

For  $R_i < R_m < R_o$ , the spreading front is arrested in the hydrophilic annulus, thereby allowing the drop to rest on the water-repellent surface in a thin lens shape as shown in figure 2.3(b). Although the contact line does not retract, a ridge formed around the rim returns to the centre, much like a drop impinging on a uniformly hydrophilic surface (Mao *et al.* 1997). However, two salient flow characteristics are observed as delineated in the following.

First, the spreading front continues to advance even as the ridge retracts (3.0 - 4.7 ms in figure 2.3(b)) unless the contact line has reached the outer edge of the hydrophilic annulus corresponding to  $R_m = R_o$ . Figure 2.4 compares the temporal evolution of the drop base radius on a uniformly superhydrophobic surface and a superhydrophobic surface with a wettable annular pattern. On the uniformly hydrophobic surface, the drop rapidly recoils upon reaching the maximum spread radius at around 3.5 ms. On the wettability-patterned surface, however, the base radius,  $R$ , plateaus after the first spreading phase that lasts till 0.01 s. In this constant-spread-radius stage, the flow induced by the inward propagation of the capillary wave of the top surface appears to balance the outward spreading driven by the high wettability of the substrate. While the contact line remains immobile, the capillary wave subsides and the drop smoothens its shape into lens. Then, the second-phase spreading (after 0.15 s) within the wettable annulus is driven by wicking of a liquid film over rough superhydrophilic surface rather than by the impact inertia.

Second, microscopic air bubbles are trapped between the liquid and the superhydrophobic surface as clearly seen in the last panel of figure 2.3(b). These tiny bubbles are formed by entrainment of air as the contact line rapidly advances. Scrutinizing the microscopic bubbles generated in this work, we find two distinct sizes of bubbles to exist: relatively small ones

### 2.3 Types of drop impact behavior

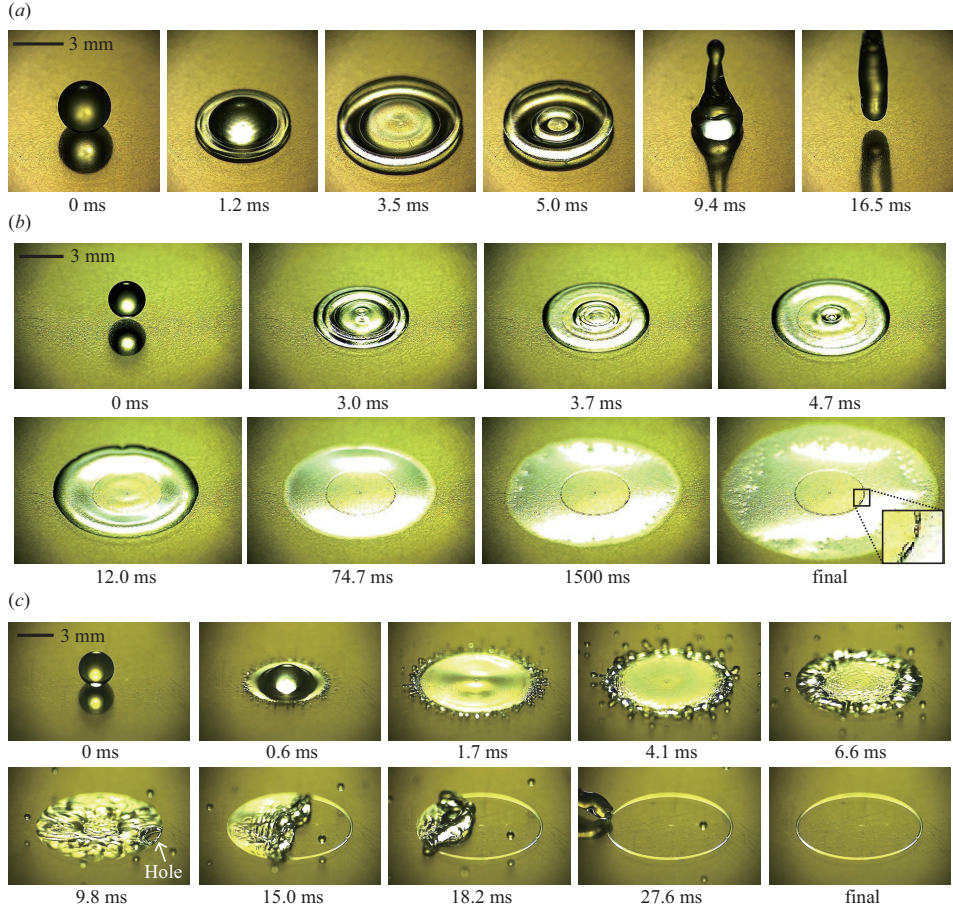


Figure 2.3: Different types of drop impact behavior. (a) Rebound for  $R_m < R_i$ . (b) Lens formation for  $R_i < R_m < R_o$ . (c) Lens rupture, droplet ejection, and generation of a ring for  $R_m > R_o$ .  $[R_i, R_o] = [4.0, 4.2], [2.5, 7.5]$  and  $[5.0, 5.2]$  mm for (a), (b) and (c), respectively. The impact Weber number  $We=25$  and 106 for (a, b) and (c), respectively.

### 2.3 Types of drop impact behavior

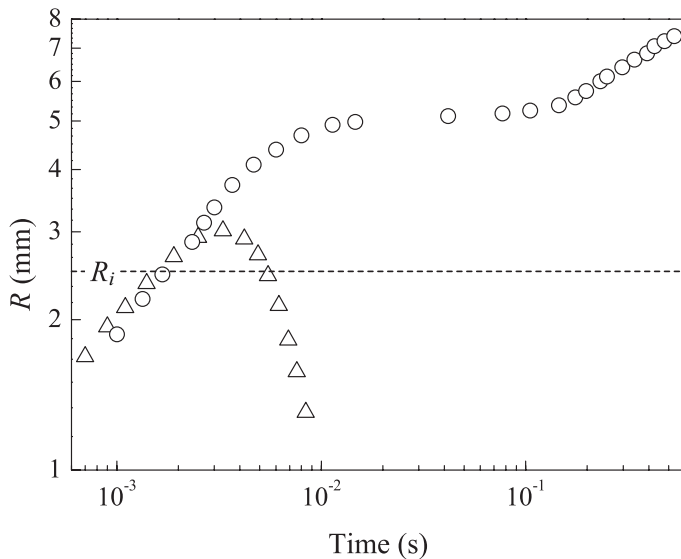


Figure 2.4: Temporal evolution of the base radius of a water drop with the initial radius  $a=1.3$  mm impacting with the speed of  $U = 1.2 \text{ m s}^{-1}$  on a uniformly superhydrophobic surface (triangles) and a wettability-patterned surface with  $R_i = 2.5$  mm (circles).

with the radius (viewed from the top) ranging between approximately 5 and  $15 \mu\text{m}$  are distributed inside the hydrophobic area, whereas larger ones are located close to the inner edge of the annulus.

The small bubbles are generated because the contact line advancing on a hydrophobic surface becomes unstable and roughened (Blake & Ruschak, 1979; Eggers, 2004) when its speed exceeds a critical value,  $U_c$ , which is predicted to be  $U_c = c\gamma(\pi - \theta_A)^3/\mu$  (Duez *et al.*, 2007), where  $c$  is a constant of the order of  $10^{-2}$ . Substituting the properties of water and  $\theta_A \approx 160^\circ$ , we find that  $U_c$  ranges between  $10^{-2}$  and  $10^{-1} \text{ m s}^{-1}$ , which is significantly lower than the typical spreading speed of the contact line in this work,  $\sim 1 \text{ m s}^{-1}$ . Therefore, the unstable contact line roughens to entrain small air bubbles until it meets the hydrophilic annulus. The process is schematically illustrated in the first two panels of figure 2.5(a) with the corresponding images shown in (b). The small bubbles with a circular top view hardly change their shapes with time. On the other hand, the formation of rela-

### **2.3 Types of drop impact behavior**

---

tively large bubbles begins when the contact line encounters the boundary of the hydrophobic-hydrophilic regions ( $R_i$ ), the second and third panels of figure 2.5(a) and (b). A strip of bubble is trapped at the boundary while the abrupt change of the liquid-solid contact mode from that of Cassie & Baxter (1944) to Wenzel (1936) occurs (Cassie & Baxter, 1944; Wenzel, 1936). We suppose that the air flow through the forest of nanopillars following the liquid flow (Cassie-Baxter state) is trapped at the wettability boundary as the liquid suddenly starts to intimately contact the rough hydrophilic area (Wenzel state). The detailed dynamics of this air trapping process leading to formation of large bubbles is worth further study but not pursued further here. The annular air strip in 0.73 ms of figure 2.5(b) evolves into a series of relatively large bubbles by capillary action, as shown in the fourth to fifth panels in figure 2.5(b). The bubbles appear rather irregular in their top views. Measuring 129 bubbles within 8 drops, we get the average area of  $0.057 \text{ mm}^2$  with the standard deviation of  $0.035 \text{ mm}^2$ . The typical range of error in the bubble area measurements is  $\pm 0.004 \text{ mm}^2$ . Once the discrete large bubbles are formed, no appreciable changes of their size and shape were detected.

To achieve  $R_m > R_o$ , as shown in figure 2.3(c), we increase the Weber number from 25 to 106 as mentioned earlier. Then the spreading front gets unstable because of a high Weber number (Kim *et al.*, 2000) and recedes upon reaching the maximum radius until it stops at the outer edge of the hydrophilic annulus ( $R_o$ ). The entrainment of air takes place similar to the process delineated above. Because this drop retains a higher kinetic energy than the previous one, its recoiling tends to be more vigorous, leaving the thin lens more vulnerable to disturbances that can lead to instability of the entire drop morphology. It is the trapped air bubbles that trigger the instability - a through hole is nucleated by one of the bubbles as shown in 9.8 ms in figure 2.3(c), which then exposes the superhydrophobic area surrounded by the wettable annulus. The liquid that has covered the superhydrophobic area is completely disengaged from the surface (27.6 ms), leaving a water ring defined by the hydrophilic annulus.

## 2.3 Types of drop impact behavior

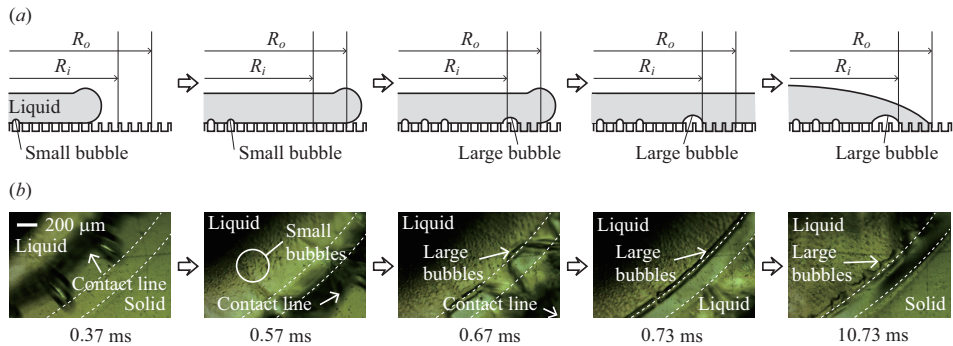


Figure 2.5: Air bubble entrainment during spreading. (a) Schematic process of entrainment of air due to instability of the contact line advancing on the hydrophobic surface and abrupt encounter of the hydrophilic region. The abrupt switch of the contact mode at the annular region from that of Cassie-Baxter to Wenzel occurs between the second and third panels, by which a large bubble is trapped. The large bubble formed at the wettability boundary (the third panel) moves into the superhydrophobic region because of a strong affinity for gas and liquid of the superhydrophobic and superhydrophilic region, respectively. In the last panel, the contact line has receded back to  $R = R_o$ . (b) Magnified images near the wettability boundary visualizing the formation process of air bubbles illustrated in (a). The times are measured from the moment that the drop hits the substrate. The dashed lines correspond to the inner and outer edges of the wettable annulus. The liquid front advances from the upper left to the lower right. In the last panel (10.73 ms), the small bubbles inside the inner wettability boundary are distinguished from the irregularly shaped large bubbles at the wettability boundary.

## **2.4 Film bursting, liquid ejection, and water ring**

---

The formation of a water ring followed by the ejection of liquid from a thin lens is the most peculiar aspect of the drop impact behavior observed on a super-wettability-contrast annular pattern. Since liquid lenses containing air bubbles are commonly subjected to this instability, the lens shown in the last panel of figure 2.3(b) is also prone to burst. In section §4, it will be explained under what conditions this bursting takes place.

## **2.4 Film bursting, liquid ejection, and water ring**

On hydrophobic surfaces, thin water films easily dewet and break up into multiple sessile droplets when subjected to external disturbances. Any films with a thickness less than the critical value  $h_c = 2l_c \sin(\theta_e/2)$ , where the capillary length  $l_c = \sqrt{\gamma/(\rho g)}$  and  $\theta_e$  is the equilibrium contact angle, are unstable (de Gennes *et al.*, 2004). For water repellent surfaces,  $h_c \approx 2l_c = 5.4$  mm, thus the thin lenses obtained in this work, e.g. figures 2.3(b,c), with the maximum lens thickness of  $\sim 80$   $\mu\text{m}$  can be destabilized easily. Furthermore, microbubbles trapped during the spreading phase aggravate the instabilities. For the drop of figure 2.3(c), a significant amount of kinetic energy remains even after initial spreading, which tends to perturb the drop leading to the immediate burst of a hole. For water drops that do not burst upon spreading into a film as the one in figure 2.3(b), we waited to see if any conformational change occurs while measuring the drop weight with a precision balance. The result was that every drop that formed a thin lens burst, so that the inner superhydrophobic area was exposed to air as shown in figure 2.6. The lens ruptures because the evaporating lens becomes unstable when its volume reaches a certain threshold value, which we estimate in the following.

We assume that the film instabilities manifest themselves when the free energy of a liquid lens penetrated with a hole,  $E_h$ , becomes lower than that of an undamaged lens,  $E_u$ , along the same line as Sharma & Ruckenstein (1989) (Sharma & Ruckenstein, 1989). Figure 2.7 shows the schematics of the liquid lenses sitting on surfaces with extreme wettability contrast.

## 2.4 Film bursting, liquid ejection, and water ring

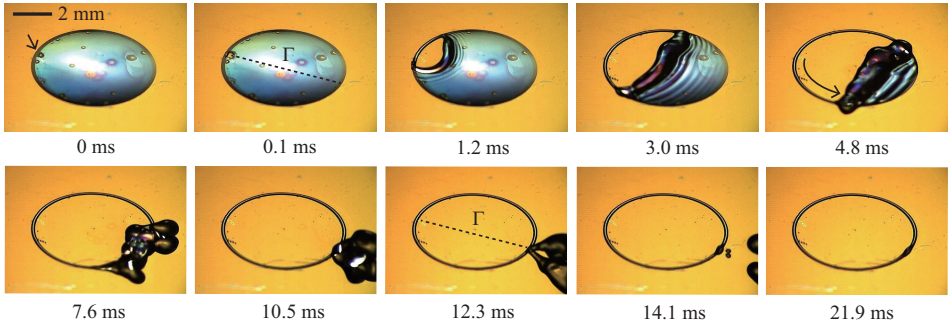


Figure 2.6: Bursting of a thin lens due to decrease of volume by evaporation, which eventually leads to the formation of a liquid ring. A bubble (indicated by an arrow) entrained in a liquid film at 0 ms generates a hole, which is detected by a high-speed camera in the next frame (0.1 ms).

The radius of the liquid drop  $a$  having the same volume as the bursting lens in this work ranges from 1.06 to 1.53 mm and the maximum height of the lenses is less than 470  $\mu\text{m}$ . Therefore, the capillary forces dominate the gravitational forces in determining the lens shape ( $l_c=2.7$  mm). This allows us to assume the lenses as truncated spheres (de Gennes *et al.*, 2004), consistent with our observation of their side views.

The undamaged lens, figure 2.7(a), is in contact with air at its top surface and touches the superhydrophilic annulus while supported by the tips of protrusions in the superhydrophobic area, locally achieving the Cassie-Baxter state. For the damaged lens, figure 2.7(b), we assume that a cylindrical hole with the bottom area,  $A_1$ , and the side area,  $A_2$ , emerges near the edge of the inner superhydrophobic area, based on our experimental observation that relatively large air bubbles are trapped at the wettability boundary. Neglecting the change of the overall lens shape with a hole, whose volume is very small compared to that of the lens, we write

$$\Delta E = E_h - E_u = \gamma [A_2 - A_1(1 - \cos \theta_C)] \quad (2.1)$$

Here we used the Cassie-Baxter equation that gives the apparent contact angle of the Cassie-Baxter state,  $\theta_C$ , as  $\gamma \cos \theta_C = \phi(\gamma_{SG} - \gamma_{SL}) - (1 - \phi)\gamma$ , where  $\phi$  is the wetted fraction of the solid area, and  $\gamma_{SL}$  and  $\gamma_{SG}$  are

## 2.4 Film bursting, liquid ejection, and water ring

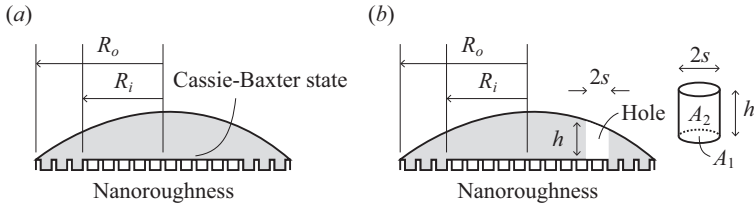


Figure 2.7: Schematic illustrations of liquid lenses on a super-wettability contrast surface with a wettable annular pattern. (a) Undamaged lens. (b) Lens penetrated with a hole of radius  $s$  located at the edge of the superhydrophobic circle.

the solid-liquid and solid-gas interfacial energy per unit area, respectively. Above we ignored gravitational potential energies in view of small thickness of the drop compared to the capillary length. Also the hole was assumed to be a circular cylinder to facilitate the evaluation of  $A_2$ . For a cylindrical hole with a radius  $s$ ,  $A_1 = \pi s^2$  and  $A_2 = 2\pi s h$ . Here  $h$  is taken to be a representative height of the cylindrical hole, as shown in figure 2.7(b):

$$h = \sqrt{R_c^2 - (R_i - s)^2} - R_c + H \quad (2.2)$$

where  $R_c$  and  $H$  are the radius of curvature and the maximum height of the drop at its critical volume for hole nucleation, respectively.

Plotting  $\Delta E$  versus the lens volume  $V$  in figure 2.8(a), we find that  $\Delta E$  becomes negative as  $V$  decreases, indicating that a small lens with a hole becomes energetically more favourable than undamaged ones. We compare the experimentally measured critical volumes that initiate the hole burst with the theoretical predictions (solid and dotted lines) in figure 2.8(b), which shows reasonable agreement between experiment and theory with a fitting parameter  $s = 75 \mu\text{m}$ , which is slightly smaller than the radius of a hole ( $\sim 90 \mu\text{m}$ ) first detected by the high-speed camera (0.1 ms in figure 2.6). We also included the theoretical results with the hole shape obtained by solving the Young-Laplace equation (dashed and dot-and-dash lines) in figure 2.8(b). In the calculation, the bottom of the hole was assumed to retain the contact angle of  $160^\circ$ , the interfacial energies of the lenses with

## **2.4 Film bursting, liquid ejection, and water ring**

and without the hole were set to be identical, and the average hole radius was taken to be 75  $\mu\text{m}$ . A hole satisfying the Young-Laplace equation for a lens on the annulus pattern with  $[R_i, R_o] = [3.5, 4.1]$  mm is shown in the inset of figure 2.8(b). The modelling results using a cylindrical hole and a hole satisfying the Young-Laplace equation are shown to differ at most 14% for the same annulus dimensions. At fixed  $R_i$ , the critical volume decreases as  $R_o$  increases; thus a lens formed on a wider annulus (large  $R_o/R_i$ ) can get thinner before burst than one formed on a narrower annulus (small  $R_o/R_i$ ).

Once a hole emerges, it expands along the inner edge of the hydrophilic annulus as it cannot interrupt the intimate contact between the liquid and the hydrophilic solid. The distance that the hole sweeps along the inner edge, as indicated by an arrow in the fifth panel of figure 2.6, turns out to increase linearly with time, giving a constant hole expansion speed,  $U_h$ , for each experimental condition.  $U_h$  ranges from 1.5 to 3  $\text{m s}^{-1}$  in this work. The corresponding Reynolds number  $Re_h = \rho U_h h / \mu$  ranges from 41 to 96. The hole opening is driven by the capillarity but resisted by inertia. If a hole is nucleated at the centre of a liquid disk, the capillary force driving the hole expansion is given by  $F_d = 2\pi r_h \gamma (1 - \cos \theta_C)$ , where  $r_h$  is the hole radius. Balancing  $F_d$  with the resisting force due to inertia,  $F_r = 2\pi \rho r_h \tilde{h} U_h^2$ , gives the hole opening speed  $U_h = [\gamma(1 - \cos \theta_C) / (\rho \tilde{h})]^{1/2}$ , where  $\tilde{h}$  is the nominal film thickness. For a film floating in the air ( $\theta_C = 180^\circ$ ), we get the Taylor-Culick formula,  $U_h = [2\gamma / (\rho \tilde{h})]^{1/2}$  (Culick, 1960; de Gennes *et al.*, 2004; Taylor, 1959). For the present superhydrophobic surface with  $\theta_C = 160^\circ$ , the numerical prefactor changes but slightly, giving  $U_h \approx 12\tilde{h}^{-1/2}$  with  $U_h$  and  $\tilde{h}$  having the units of  $\text{cm s}^{-1}$  and cm, respectively. Although the hole in this work is nucleated near the edge of lens rather than the centre, our experimental measurements of  $U_h$  indeed reveal that  $U_h$  is scaled as  $h^{-1/2}$  as shown in figure 2.9. Here we have taken  $\tilde{h} = h$ . The inset of the figure finds the proportionality constant to be 11.5 through the least-square method, a value surprisingly close to the one derived for a hole opening from the centre.

## 2.4 Film bursting, liquid ejection, and water ring

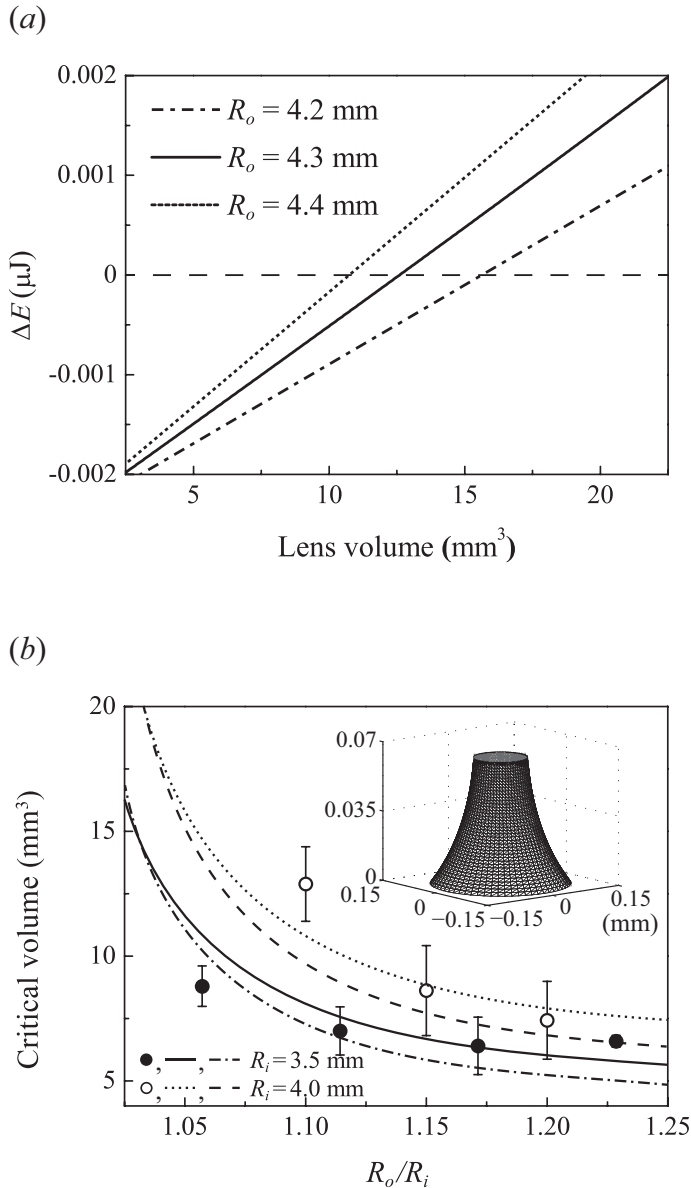


Figure 2.8: (a)  $\Delta E$  versus the lens volume for  $[R_i, s] = [4, 0.075]$  mm. (b) Critical volumes at which a hole bursts. The solid and dotted lines are the theoretical predictions using the cylindrical hole assumption. The dashed and dot-and-dash lines are the theoretical predictions for the holes satisfying the Young-Laplace equation. Circles are the measurement results. The inset is the hole shape satisfying the Young-Laplace equation for a lens on the annulus pattern with  $[R_i, R_o] = [3.5, 4.1]$  mm.

## 2.4 Film bursting, liquid ejection, and water ring

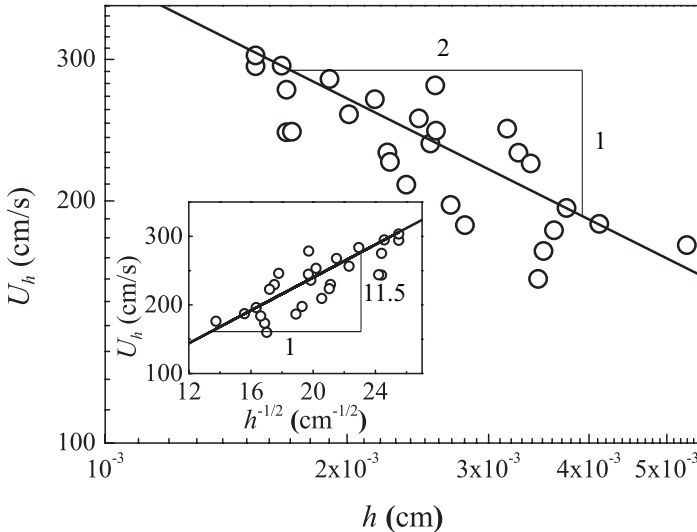


Figure 2.9: Speed of hole expansion  $U_h$  versus  $h$  for various values of initial drop volume,  $R_i$  and  $R_o$ . The inset plots  $U_h$  versus  $h^{-1/2}$  to find the proportionality constant to be 11.5.

Because the film gets thicker toward the centre, corresponding to lower  $U_h$ , the hole opens along the edge first. This causes the central droplet to be completely separated from the surrounding rim adhered to the hydrophilic annulus. As the central part of the lens transforms into a sphere due to surface tension effect, its excess energy, i.e. the difference of the potential energies of the lens and the sphere, is partly converted to the translational kinetic energy. This allows the droplet to disengage from the water-repellent surface, or jump.

We note that the path of the liberated droplet projected on the solid surface is exactly overlapped with a line  $\Gamma$  that connects the hole nucleation site and the centre of the annulus, as illustrated in figure 2.6 (0.1 and 12.3 ms). It is because the hole expansion and resulting film lift is symmetric about the line  $\Gamma$  before it loses contact with the intersection of the line  $\Gamma$  and the annulus. The take-off angle  $\beta$  is closely associated with the relative speed of hole opening to film flotation. As shown in figure 2.10(a), when the lens is relatively flat for its large area of inner circle (large  $R_i$ ) or wide

## **2.4 Film bursting, liquid ejection, and water ring**

annulus (large  $R_o/R_i$ ), the hole opening along the edge and the retraction of the film occur almost at the same rate because of relatively uniform thickness throughout the lens. Thus, the droplet is ejected almost parallel to the solid surface, yielding a very low  $\beta$ ,  $7^\circ$ . On the other hand, for a highly curved lens with a small area of inner circle (small  $R_i$ ) or narrow annulus (small  $R_o/R_i$ ), figure 2.10(b), the hole opening is much faster than the film retraction toward the centre. The difference in the speeds of hole opening and film retraction is caused by a relatively large difference of the film thicknesses near the wettability boundary and at the centre. Thus, the central film is quickly separated from the rim before being lifted in the air. Then the isolated liquid mass jumps off the surface forming a spherical droplet with a high  $\beta$ ,  $31^\circ$ . We plot the experimentally measured values of  $\beta$  versus the characteristic slope,  $\kappa R_i$ , of the lenses assumed as a truncated sphere in figure 2.10(c), to find that  $\beta$  is strongly correlated with  $\kappa R_i$ . Here  $\kappa$  is the curvature of the bursting lens.

By comparing the surface energy change of a liquid mass associated with separation from the rim and its kinetic energy at take-off, it is possible to evaluate how much energy is dissipated during the droplet ejection process. The reduction of the surface energy as liquid transforms from a sessile film to a floating sphere corresponds to  $\Delta E_s = \pi R_i^2 \gamma (1 - \cos \theta_C) - 4\pi r_d^2 \gamma$ , where  $r_d$  is the radius of the spherical droplet ejected from the lens. Here, the surface area of the spherical lens exposed to air,  $A_u = \pi R_i^2 [1 + (H-h)^2/R_i^2]$ , is simply approximated to be  $A_u \approx \pi R_i^2$  because  $(H-h)^2/R_i^2$  is of the order of  $10^{-2}$ . With the take-off speed of the droplet  $v_d$ , the kinetic energy is written as  $\Delta E_k = (2\pi/3)\rho r_d^3 v_d^2$ . In our experiments,  $r_d$  varies from 0.80 to 1.24 mm and  $v_d$  from 0.68 to 1.45 m s<sup>-1</sup>. Figure 2.10(d) plots the energy conversion ratio,  $\Delta E_k/\Delta E_s$ , versus the characteristic slope  $\kappa R_i$ . Unlike the take-off angle, the energy conversion ratio tends to decrease with  $\kappa R_i$ . It is attributed to the shape of ejected droplets that depends on the take-off angle or  $\kappa R_i$ . The droplet shape is highly irregular upon take-off for high  $\kappa R_i$ , e.g. the one in 9.8 ms in figure 2.10(b), while it is close to spherical for low  $\kappa R_i$ , e.g. the one in 16.4 ms in figure 2.10(a).

## **2.4 Film bursting, liquid ejection, and water ring**

Therefore, the surface energy of droplets ejected from highly curved lenses is converted into vibrational and viscous energy in addition to translational kinetic energy (Biance *et al.*, 2006), lowering the ratio  $\Delta E_k/\Delta E_s$ , from approximately 0.3 to 0.2.

The jumping of drops on superhydrophobic surfaces has been reported in several other situations as well. Drops impacting on a uniformly superhydrophobic surface rebound vertically (Richard & Quéré, 2000). Whereas, those colliding with nonuniform wettability would rebound obliquely because of the difference in dewetting speeds around the rim of squeezed drops. Reyssat, Pardo & Quéré (2009) observed the oblique rebound of water drops hitting micropillar arrays with gradients of pillar density, where the take-off angle could be varied from  $90^\circ$  to approximately  $60^\circ$  (Reyssat *et al.*, 2009). In addition, tiny droplets undergoing coalescence (Boreyko & Chen, 2009) and melting (Habenicht *et al.*, 2005) can jump off water-repellent surfaces. The high-speed imaging of Boreyko & Chen revealed that condensate water drops with a diameter of the order of  $10^2 \mu\text{m}$  merge and almost vertically jump off a superhydrophobic surface with a velocity of the order of  $0.1 \text{ m s}^{-1}$ . Comparing with those previous investigations of droplet jumps off the surface, we find that the current work achieves the lowest take-off angle, which may be useful where violent droplet behavior needs to be avoided, e.g. within a small lab-on-a-chip system.

Next we consider the volume and stability of the ring that remains after film burst. We assume that the cross-section of the ring is a truncated circle because the Bond number,  $Bo = \rho g b^2 / \gamma \sim 10^{-5}$ , where  $b$  is the maximum thickness within the ring. Then the volume of the ring,  $V_r$ , is related to the apparent contact angle of the ring,  $\theta_0$ , as

$$V_r = \frac{\pi}{2} (R_i + R_o) \left( \frac{R_o - R_i}{2 \sin \theta_0} \right)^2 (2\theta_0 - \sin 2\theta_0) \quad (2.3)$$

Our experiments reveal that  $\theta_0$  ranges between  $2^\circ$  and  $28^\circ$ . We found qualitatively that  $V_r$  and  $\theta_0$  tend to increase with the decrease of  $\kappa R_i$  (or decrease of  $\beta$ ). The tendency is because a stretched liquid bridge trailing the ejected droplet, as shown at 12.6 ms in figure 2.10(a), partly recoils

## 2.4 Film bursting, liquid ejection, and water ring

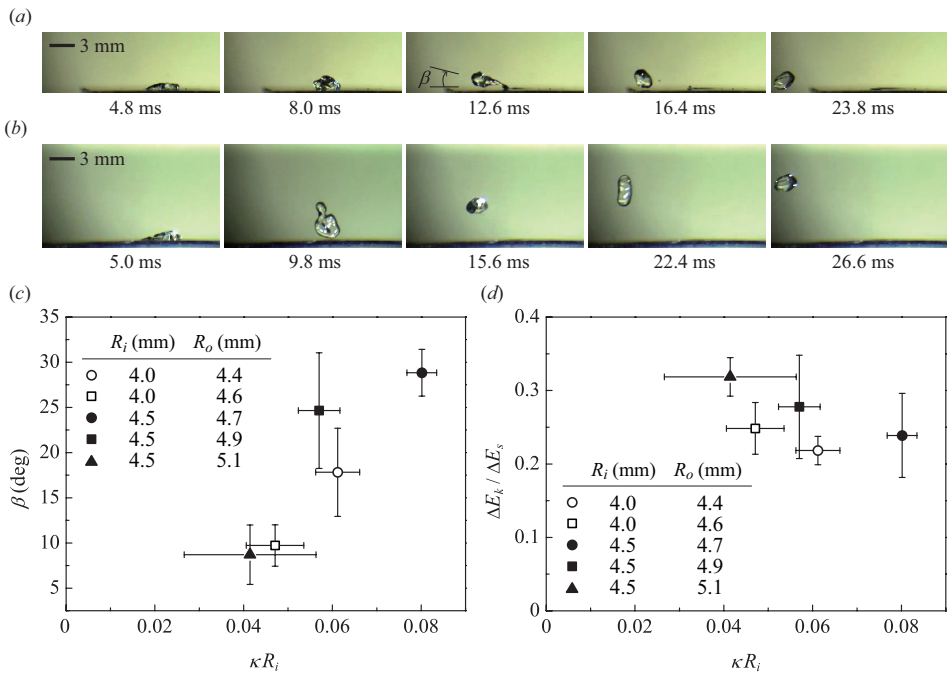


Figure 2.10: (a) Ejection of a droplet from a relatively flat liquid lens.  $[R_i, R_o] = [4.0, 4.6]$  mm. (b) Ejection of a droplet from a relatively curved liquid lens.  $[R_i, R_o] = [4.5, 4.7]$  mm. (c) The take-off angle ( $\beta$ ) versus the lens slope ( $\kappa R_i$ ). (d) The kinetic to surface energy ratio versus the lens slope.

## 2.4 Film bursting, liquid ejection, and water ring

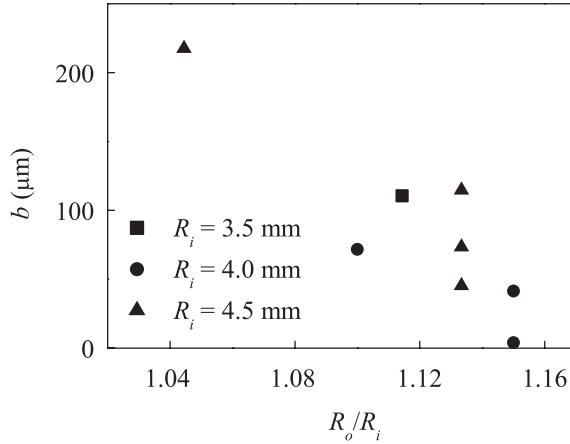


Figure 2.11: Maximum thickness of liquid ring  $b$  versus  $R_o/R_i$ .

back to the ring at low  $\beta$ . Such recoiling of the bridge increases the volume of remaining ring. When the liquid ring is bound by the pre-defined hydrophilic annulus, the contact line is pinned, and thus the ring is stable, i.e. no beading occurs, for  $\theta_0 < \pi/2$  (Davis, 1980; Schiaffino & Sonin, 1997), which is consistent with our observations. For  $\theta_0 > \pi/2$ , the liquid thread is known to be subjected to capillary instability. Because of the low contact angle of the rings produced in this work, the rings remain stable until they are dried off and dry spots appear.

Finally we measure the maximum thickness of the ring, as shown in figure 2.11. For small  $R_o/R_i$ , The maximum thickness of the ring reaches to the same order of ring width while it is significantly smaller than ring width for large  $R_o/R_i$ . Despite being aforementioned mass loss or increase, we assume that  $V_r$  is proportional to the volume difference between the entire lens and film on the superhydrophobic inner circle. Then the maximum thickness of the ring  $b$  can be written as the following.

$$b \sim \frac{V_{cr}^2}{R_o^2} \left[ 1 - \frac{1 - R_i/R_o}{(R_o/R_i)^2 - 1} \right]. \quad (2.4)$$

Here we assume that the cross-section of the ring is a triangle, because of small  $\theta_0$  and  $V_{cr}$  is the critical volume of rupture.  $1 - (1 - R_i/R_o)/(R_o/R_i)^2 -$

## 2.5 A practical implication

---

1) ranges between 0.53 and 1 and thus the previous scaling model is summarized into  $b \sim V_{cr}/R_o^2$ , which is consistent with the experimental tendencies in figure 2.11 although we does not consider mass variation and exact ring profile.

## 2.5 A practical implication

The wettability contrast can be explored to generate liquid patterns on solid surfaces for rapid printing of electronic circuits (Russo *et al.*, 2011) and biological fluids (Roth *et al.*, 2004). As shown in figure 2.12, liquid lines and curves can be easily drawn by impacting a liquid drop on a tilted substrate. Starting from a photomask with a desired pattern, figure 2.12(a), we perform photolithography on a uniformly superhydrophobic surface in the same manner as figure 2.1. Then the hydrophobic substrate is selectively treated to turn hydrophilic in desired areas. Upon drop impact, while the liquid is rapidly drained down the substrate, the contact lines are arrested on hydrophilic patterns thereby allowing the liquid to be patterned along the pre-defined hydrophilic areas as shown in figure 2.12(b). Although being a promising method to print functional liquids on solids, this method may cause a serious problem in drawing closed curves if the liquid covering the inner region fails to be drained. The behavior of a liquid film investigated in this work provides a viable solution to this problem - thin films arrested by hydrophilically treated closed curves are unstable thus spontaneously rupture to expose the hydrophobic inner regions as shown in figure 2.12(c). The liquid ejection behavior from the rectangular wettable loop is similar to what is observed for the circular loops.

It is noted that most functional liquids, including conducting liquids and biological fluids, may have higher viscosity and lower surface tension than pure water, providing more resistance and less driving forces to the film rupture. By testing the bursting behavior of water-glycerine mixtures (36 wt% glycerine,  $\mu = 3.1$  mPa·s,  $\gamma = 68.2$  N/m) on an annulus pattern with  $R_i = 4.0$  and  $R_o = 4.4$  mm, the liquid film is found to still burst when

## 2.6 Conclusions

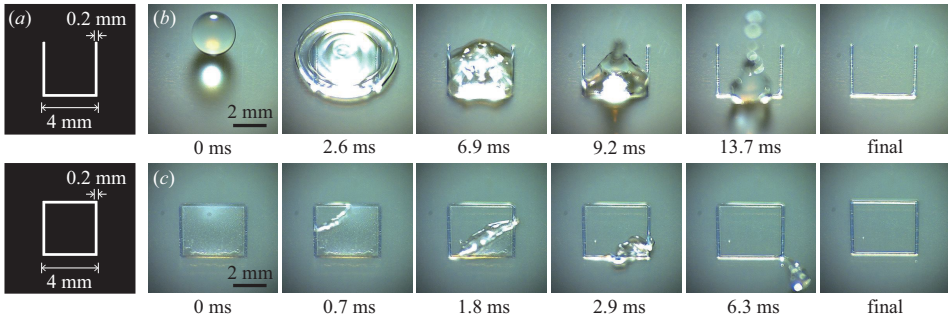


Figure 2.12: Rapid printing of a liquid deposit using wettability-contrast patterns. (a) Photomask pattern used to print liquid on solids. (b) Printing of water on the wettability-patterned surface that is tilted  $16^\circ$  from the horizontal. The drop is easily removed from the hydrophobic region when the hydrophilic curve is open. (c) Printing of closed curves using spontaneous film rupture.

its volume is decreased by evaporation just as a pure water deposit does. However, the threshold volume for the burst is measured to be 71% that of water, implying that water-glycerine films burst at a smaller thickness than water films. Also the film rupture speed is found to be only 16% that of water, hinting a retardation effect of increased  $\mu$  and decreased  $\gamma$  on bursting.

## 2.6 Conclusions

We have shown that drops impacting on super-wettability-contrast annular patterns exhibit novel dynamic behaviors that are distinguished from ones on surfaces with uniform wettability. The liquid film covering the superhydrophobic region as arrested by the hydrophilic annulus is spontaneously ruptured to completely disengage from the surface leading to the formation of a water ring. The critical volume of the film for hole formation and the take-off angle and energy conversion ratio of the ejected droplet have been quantified. The practical implication that this phenomenon has in association with the printing of functional liquids has been demonstrated.

## 2.6 Conclusions

---

The jumping of drops on superhydrophobic surfaces, reported here and in several other situations (Boreyko & Chen, 2009; Habenicht *et al.*, 2005; Richard & Quéré, 2000), are commonly due to a severe difference of the surface energy of a deposit on a solid surface and that of a floating drop of the identical mass. The surface energy difference is released in the form of the translational and vibrational kinetic energy. The ejection of a part of liquid lens as observed in this work serves as another novel example of strong water repulsion dynamics. Also, the ejection of water controlled by the liquid film mass (varied via evaporation in this work) provides a novel pathway to achieving jetting of liquids resting on solids, which was mainly explored using electrohydrodynamic effects so far (Collins *et al.*, 2008; Kim *et al.*, 2011).

# Chapter 3

## Liquid spreading along wettable rails

### 3.1 Introduction

In contrast to the deposition of liquid on hydrophobic surface, liquid usually spreads on the hydrophilic surface because of intimate contact between the liquid and solid surface, leading to a positive spreading parameter (de Gennes et al. 2004). Thus, the wetting velocities on the hydrophilic surface have been the subject of intense study for many decades. Tanner (1979) first showed that spreading was driven by capillary force and resisted by viscous force, resulting in the following power law of film expansion,  $R \sim t^{1/10}$ , where  $R$  and  $t$  are spreading radius of deposited drop and time, respectively. Later, several power laws have been proposed to describe different driving, resisting force (Biance *et al.*, 2004; Ehrhard, 1993; Huppert, 1982; Lopez & Miller, 1976). When the spreading drop is driven by gravitational force, the spreading radius of the drop differently increases with time depending on whether the viscous resisting forces are exerted on an entire drop or on contact line, resulting in  $R \sim t^{1/7}$  (Ehrhard, 1993) and  $R \sim t^{1/8}$  (Huppert, 1982; Lopez & Miller, 1976), respectively. For the spreading driven by capillary force and resisted by inertial force, the power law was shown to be  $R \sim t^{1/2}$ , which was generally observed in the early

### 3.1 Introduction

---

stage of spreading (Biance *et al.*, 2004).

Recently, spreading on the mechanically and chemically patterned surfaces have been employed thanks to the recent development in microelectromechanical systems (MEMS). When the deposited solid surface is mechanically patterned, different dynamics and corresponding power laws are observed due to the magnified intrinsic wettability (Chandra & Yang, 2011; Kim *et al.*, 2011a). As a result, the liquid starts to penetrate onto the gaps of patterned pillars, thus forming a relatively thin fringe film in addition to a relatively thick bulk film (Kim *et al.*, 2011a). The spreading dynamics differs depending on whether or not the bulk part exists. For the spreading coupled to bulk flow, the advancing front of the fringe film grows like  $t^{1/2}$  (Kim, 2011b; Kim *et al.*, 2011a) that is similar to the Washburn's law (Washburn, 1921), but for the spreading without bulk flow, the expansion of the fringe film accompanies lateral zipping phenomena, leading to a power law ( $t^{1/4}$ ) (Kim *et al.*, 2011a). Mechanical patterns of substrate also show an intriguing shape of liquid deposit. Liquid can be deposited on the microtextured surface through the zipping mechanism in the late stage of the spreading, and the shape of liquid deposit can be manipulated by controlling the spacing, dimensions, and the shape of the pillars, thus resulting in a polygonal liquid deposit (Bico *et al.*, 2001; Courbin *et al.*, 2007; Kim *et al.*, 2011a; Sbragaglia *et al.*, 2007). When the solid surface is chemically modified in such a way that a hydrophilic stripe is surrounded by a hydrophobic background, liquid spreads only along the wettable stripe, thus lead to formation of a liquid filament (Darhuber *et al.*, 2001; Ledesma-Aguilar *et al.*, 2011). Darhuber *et al.* (2001) showed that the rate of the filament increase was still governed by Washburn's law, despite being a difference in the deposited solid surface compared to the mechanical pattern surface, as mentioned earlier.

Here we discuss the spreading on the chemically patterned surface whose geometries are the same as mentioned in Darhuber *et al.* (2001), but has nanoscale roughness on it to enhance its intrinsic wettability. we find that the increase rate of the liquid filament on the nanoroughness surface is

### 3.2 Experimental apparatuses

	Liquid	$\rho$ (kg/m <sup>3</sup> )	$\gamma$ (N/m)	$\mu$ (Pa·s)
A	Water	998	0.072	0.001
B	Glycerine 60 wt%	1151	0.067	0.009
C	Ethanol	789.5	0.022	0.0014

Table 3.1: Liquid properties at about 23°C.

much higher than that on the flat surface and a variety of power laws can be observed in addition to Washburn’s power law. In the following, we first discuss experimental apparatuses and show the spreading abilities depending on the width of hydrophilic stripe. Then, we provide several power laws of the spreading front, which differ depending on the exerted force. Finally, we construct regime map based on the developed models.

## 3.2 Experimental apparatuses

We use silicon wafer substrates to fabricate super-water-repellent surfaces with wettable annular patterns. We first clean the substrate with Ar gas and then follow the steps illustrated in Kim *et al.* (2013). We create nanoscale roughness on the surface through O<sub>2</sub> etching in a plasma-assisted chemical vapour deposition (PACVD) chamber for 60 min. Then it is coated with an amorphous C<sub>6</sub>H<sub>18</sub>Si<sub>2</sub>O film using hexamethyldisiloxane (HMDSO) gas via PACVD process. The resulting surface is covered with nanograsses as shown in figure 3.1(a), and the surface roughness, defined as the ratio of the actual surface area to the projected area, is 1.8. By adopting the method in Kim *et al.* (2013), we selectively hydrophilicize an line pattern on the superhydrophobic background and we vary the width of the hydrophilic line pattern so that the width  $w$  ranges between 200 and 2000 μm. By imaging water drops of 2 μl volume, the equilibrium contact angle  $\theta_e$  of the superhydrophilic and the superhydrophobic surface is measured to be nearly zero and 160 ± 2°, respectively.

We put deionized water inside the capillary tube, whose inner and outer

### **3.3 Liquid spreading along microstripes**

---

radius are 0.59 and 0.78 mm, respectively, by touching the free surface of water on tilted tubes so that the height of water column inside the tube ranges between 30 and 40 mm, which is larger than Jurin's height,  $h_J$ . Beside water, we also use 60 wt.% aqueous glycerince, and ethanol as illustrated in 3.1. After we insert the liquid into a capillary tube, the liquid hanging from the tube is gently touched by the superhydrophilic microstripes. The shape evolution of spreading liquid is recorded by a high-speed camera (Photron Fastcam SA1.1) at a rate ranging between 60 and 5000 frames per second with the pixel resolution of  $512 \times 512$ .

## **3.3 Liquid spreading along microstripes**

When a liquid hanging from a capillary tube is deposited on the hydrophilic microstripes with nanoroughness, the spreading behaviors differ depending on the width of the hydrophilic rails and height of the liquid column inside the tube, as shown in figure 3.2. For the narrow stripes, a bulk part of liquid does not penetrate into the gap between hydrophilic edges, but the thin film spreads as shown in figure 3.2(a). For the wide stripes, the bulk liquid can penetrate into the gap, thus showing relatively fast spreading behavior, as shown in figure 3.2(b). The experimental spreading extents  $x$  are measured from imaging analysis and we plot  $x$  versus time, as shown in figure 3.2(c). Figure 3.2(c) shows the dependencies of  $x$  on  $w$ ,  $h_{L,o}$ , where  $h_{L,o}$  is the height of initial liquid column. Figure 3.2(d) shows the various power law of liquid spreading. According to our experiments, the thin film like figure 3.2(a) spreads like  $t^{1/7}$ , but the thick film like figure 3.2(b) spreads with different power laws, which differ depending on the spreading extents. For the sufficiently high  $w$ ,  $h_{L,o}$ , an inertial force is dominant at the early stages of liquid spreading, as shown in figure 3.2(d). In this regime,  $Re$  is larger than 1, thus implying consideration of inertial force, rather than viscous force. When the hydrophilic rails with small width are wetted by liquid,  $Re$  is usually less than 1 and viscous resisting force should be considered, thus resulting in different power laws as delineated above.

### 3.3 Liquid spreading along microstripes

---

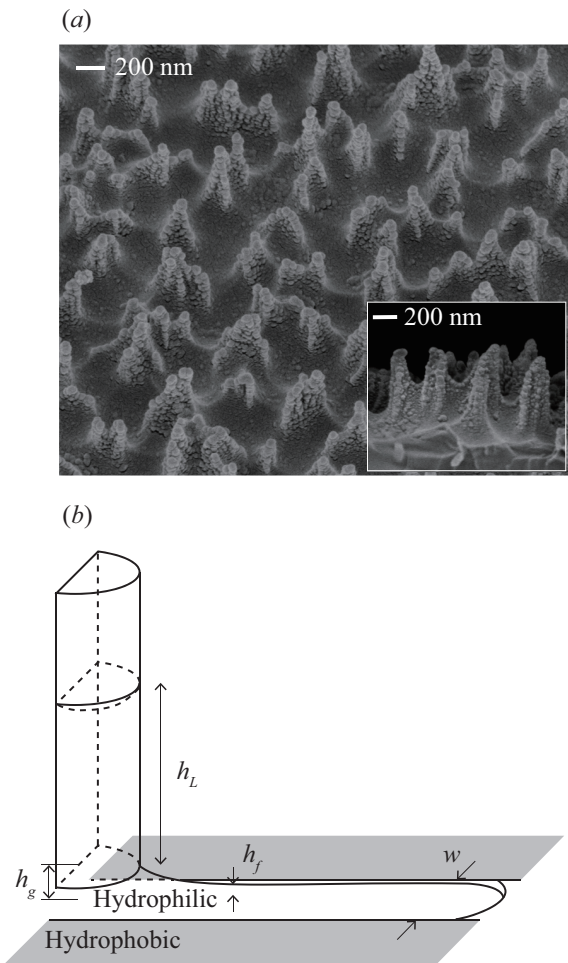


Figure 3.1: (a) Scanning electron microscopy (SEM) image of nanograsses formed on a silicon wafer. The inset is a side view of the substrate. (b) Experimental apparatuses for letting a liquid flow along a hydrophilic rail.

### 3.4 Spreading with thin precursor film

---

In this regime, liquid spreads with  $x \sim t^{1/4}$  at the early stages and  $x \sim t^{1/2}$  at the late stages and the onset of the relation  $x \sim t^{1/2}$  is triggered by  $w$  and  $h_{L,o}$ .

## 3.4 Spreading with thin precursor film

When the liquid is brought into contact with the narrow superhydrophilic microstripes, a bulk part of liquid cannot spreads along the stripes and become stationary at short time, as shown in the second panel of figure 3.3(a). It is because the hydrostatic force exerted by the height of liquid column does not sufficiently high to overcome high resistance at the entrance due to the highly curved meniscus of bulk liquid on the surface. After pinning of the bulk part, very thin precursor film is emitted from the bulk part (the third panel of figure 3.3(a)). Figure 3.3(b) shows that the precursor film penetrate into the gaps of nanopillars by forming sharp intrusions, thus showing capillary imbibition phenomena.

The increase in the surface energy related to the increase of the spreading extents from  $x$  to  $x + \delta x$  is given by:  $\delta E = \gamma w \delta x + (\gamma_{SL} - \gamma_{SG}) f w \delta x = -\gamma(f-1)w \delta x$ . By considering imbibition force  $F_w$  as  $-\delta E / \delta x$ , thus hemi-wicking force can be written as  $F_w \sim \gamma(f-1)w$ . As mentioned earlier, this driving force  $F_w$  is resisted by viscous force exerted by the spacing and height of the pillars and the resisting force can be modeled as following:  $F_{v,r} \sim (f\mu U/h_p)wx$ . Balancing the driving and resisting force, we write  $xU \sim [(f-1)\gamma/(f\mu)]h_p$  and integrating previous equation is given by  $x - x_b \sim \sqrt{(f-1)\gamma h_p/(f\mu)}t^{1/2}$ , where the previous model can be nondimensionalized by using capillary-viscous time scale  $T_{p,v} = \mu h_p/\gamma$  and we can write

$$\frac{x - x_b}{h_p} \sim \sqrt{\frac{f-1}{f}} \frac{t}{T_{p,v}}, \quad (3.1)$$

where the  $x_b$  and  $h_p$  is the spreading extents of bulk part and pillar height of nanograsses, respectively. By plotting the scaled spreading extents of precursor film  $(x - x_b)/h_p$  versus  $\sqrt{[(f-1)t/(fT_{v,p})]}$ , where  $T_{v,p}$  is

### 3.4 Spreading with thin precursor film

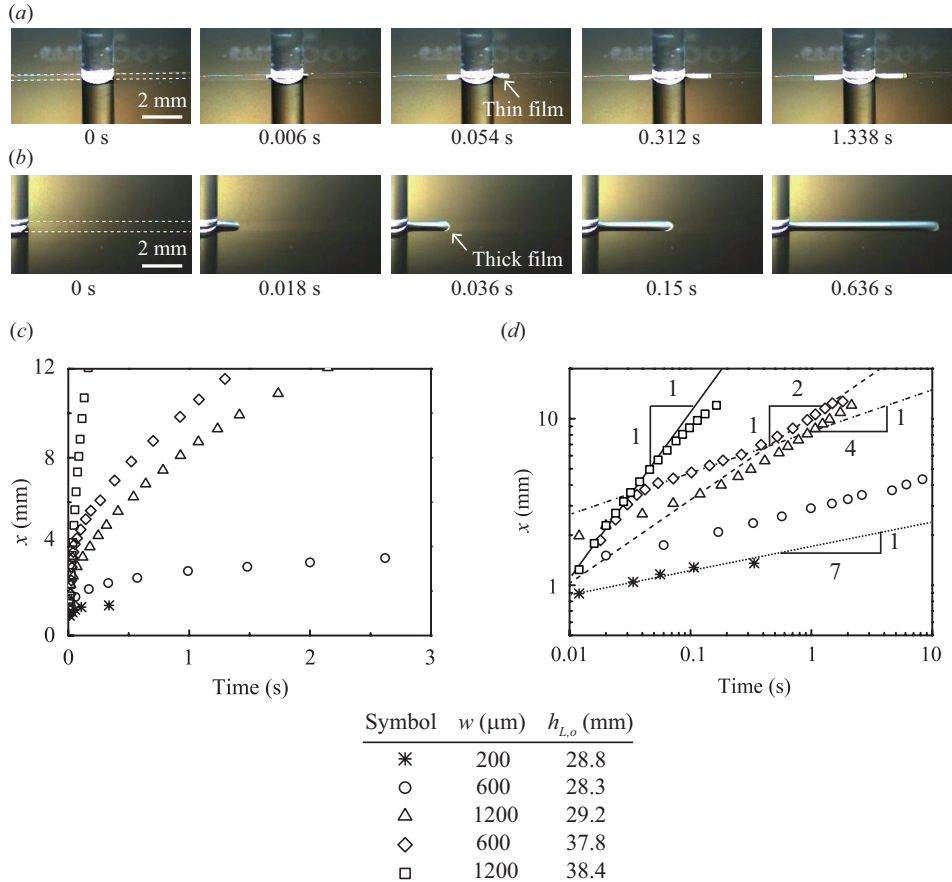


Figure 3.2: Liquid spreading on superhydrophilic rails. (a) Thin film spreading for  $[w, h_{L,o}] = [0.4, 28.5]$  mm. (b) Thick film spreading for  $[w, h_{L,o}] = [0.8, 33.2]$  mm. In the first panels of (a, b), The dashed lines correspond to the edges of hydrophilic rails. The liquid front spreads along the predefined hydrophilic rail when the liquid hanging from a capillary tube is brought into contact with a hydrophilic surface. (c) Linear and (d) log-log plot of experimentally measured spreading extents  $x$  versus time  $t$ .

### 3.4 Spreading with thin precursor film

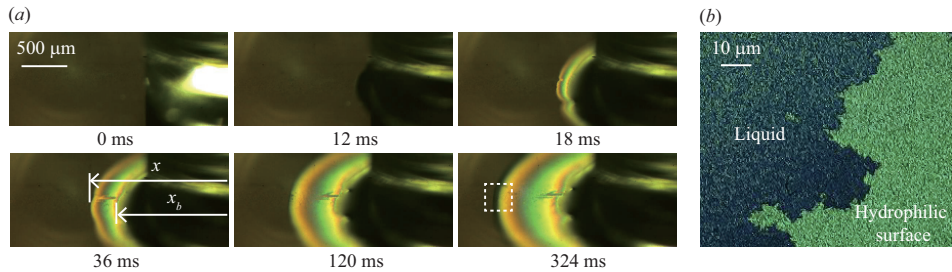
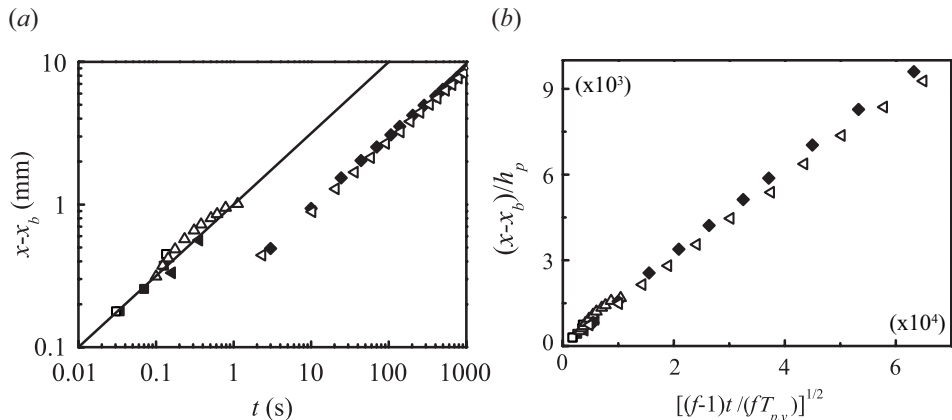


Figure 3.3: (a) Propagation of a thin precursor film emerging from a bulk liquid beneath the capillary tube. (b) Magnified view of the precursor film spreading corresponding the dashed box in the sixth panel of *a*. The liquid front penetrates into the gaps of the nanopillars by forming sharp protrusions at the contact line.



Symbol	Liquid	$w$ ( $\mu\text{m}$ )	$h_{L,o}$ (mm)
■	A	200	28.7
□	A	200	33.1
△	A	2000	10.0
◀	A	4000	10.0
◆	B	1000	10.0
▷	B	1000	10.0

Figure 3.4: (a) Log-log plot of experimentally measured spreading extents of a precursor film  $x - x_b$  versus time  $t$ . (b) The scaled spreading distance,  $(x - x_b)/h_p$  plotted according to the scaling law. Here,  $T_{p,v}$  is the viscous-capillary time scale, which is defined as  $\mu h_p/\gamma$  by using the characteristic length of hemi-wicking,  $h_p$ .

### 3.5 Spreading with bulk film

---

characteristic time of capillary-viscous force,  $\mu h_p/\gamma$ , we collapse the experimental data onto a single master curve. For the narrow superhydrophilic microstripes, the spreading front does not depend on the hydrophilic stripe width and supplying pressure and it is solely determined by properties of liquid and solid such as surface tension, viscosity, and the size of the surface roughness.

Next, we model a boundary between the precursor and bulk spreading. A pressure exerted by hemi-wicking force  $p_h$  is given by:  $\gamma(f - 1)/h_p$ , which is derived by dividing wicking force over effective area  $wh_p$ , and a hydrostatic pressure beneath the tube  $p_s$  is scaled by  $\rho g(h_{L,o} - h_J)$  and the resisting pressure due to the highly curved liquid front  $p_r$  is scaled by  $\gamma/w$  by assuming the shape of liquid front as a half circle. Comparing  $p_h$  and  $p_r$ , we figure out  $p_h$  is always larger than  $p_r$  in our experimental conditions, and thus hemi-wicking consistently occurs. Balancing  $p_s$  and  $p_r$ , we obtain  $(h_{L,o} - h_J)/l_c \sim l_c/w$ , which corresponds to the upper limit of the precursor film spreading because the bulk entirely spreads above this limit. Figure 3.5 shows that the separation between the bulk and precursor spreading is divided by the linear relationships between  $(h_{L,o} - h_J)/l_c$  and  $l_c/w$ . Thus, for the region below the critical line, imbibition drive the spreading and thin film with thickness being a order of pillar height. On the other hand, bulk film is entrained along the hydrophilic microstripe because of the small entrance resistance.

## 3.5 Spreading with bulk film

As shown earlier, Bulk film spreading are separated into three different regimes depending on the principal driving and resisting forces. We first start with early stage of bulk spreading, where the inertial force is dominant if  $w$  or  $h_L$  is sufficiently large. we term this spreading phase as "Inertial regime".

### 3.5 Spreading with bulk film

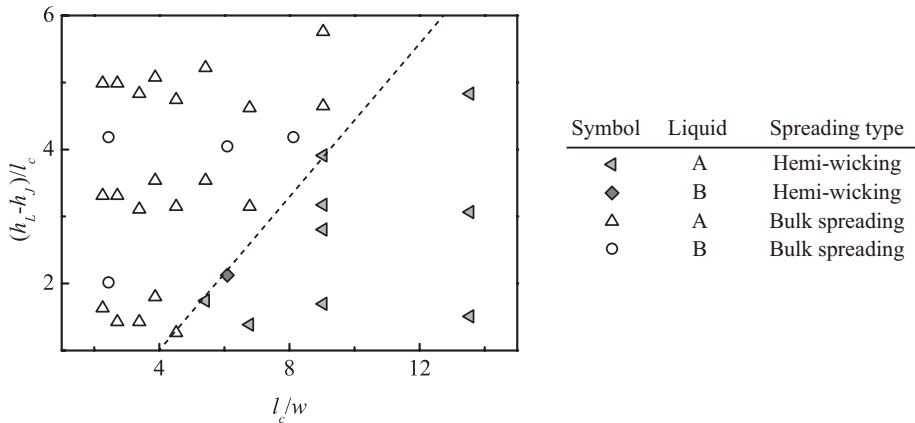


Figure 3.5: Critical boundary between thin precursor film and bulk film spreadings.

#### 3.5.1 Inertial regime

Figure 3.6 shows that the bulk film is stretched upon contact with hydrophilic rail and the inertial spreading disappears in short time scale. To predict the spreading rate in inertial regime, we model a shape of liquid film as a wedge, as illustrated in figure 3.7. The pressure force exerted on the contact line is given by:  $\gamma(f - 1)/h_p$  by dividing wicking force over effective area, and thus the gradient of pressure inside the stretched film is written by:  $\gamma(f - 1)/(xh_p)$ , which is resisted by inertial force of the film. Entrained mass is sum of the liquid on the rail and inside the capillary tube, but we neglect the inertia inside the tube because the vertical direction of the resisting force does not contribute the direction of spreading. Thus the inertial force can be written as following:  $[\rho h_g w]d(xU)/dt$ . Balancing the capillary force and inertial resisting force, we obtain the following equation:  $x \sim \sqrt{(\gamma(f - 1))/(\rho h_p)}t$ , where the previous model can be nondimensionalized by using capillary-inertia time scale  $T_{p,i} = \sqrt{\rho h_p^3/\gamma}$  and we can write

$$\frac{x}{h_p} \sim \frac{t}{T_{p,i}}. \quad (3.2)$$

We validate this model by plotting the scaled spreading distance  $x/h_p$  according to the scaling model (equation 3.2). The dispersed experimental

### 3.5 Spreading with bulk film

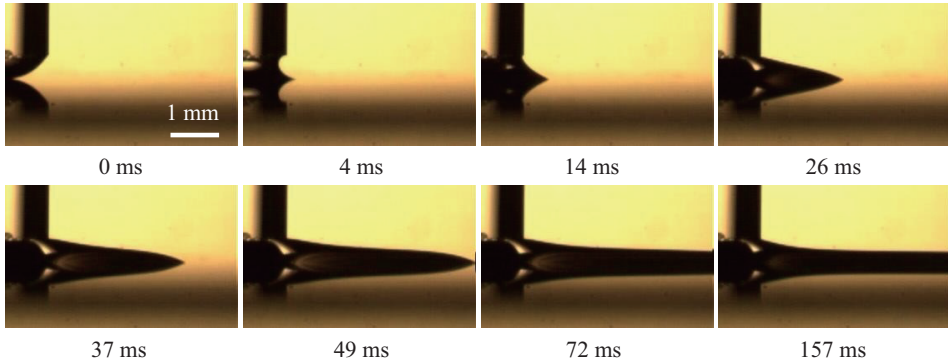


Figure 3.6: Side view of early film spreading in an inertia dominant stage for  $[w, h_{L,o}] = [1.0, 38.4]$  mm.

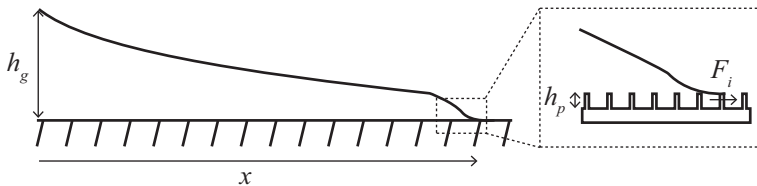


Figure 3.7: Schematic model for describing inertial film spreading.

data in figure 3.8(a) is collapsed onto a single master curve in figure 3.8(b), regardless of liquid properties. The time scale of inertial regime is generally small compared to other regimes, but this regime is important because of the high spreading rate.

#### 3.5.2 Capillary bending regime

As mentioned earlier, the relation  $x \sim t^{1/4}$  is found in early spreading for the narrow stripes. In this situation, the curvature near the tube end is slowly changed with increase of  $x$ , as shown in the dashed circle of figure 3.10. The liquid film is abruptly pulled by the superhydrophilic rail and the highly curved meniscus is formed. To match such a highly curved meniscus around the the tube, the meniscus shape of the liquid front should be microscopically bended. Thus, it implies that the bended meniscus is gradually relaxed as time elapses, thus resulting in variation of advancing

### 3.5 Spreading with bulk film

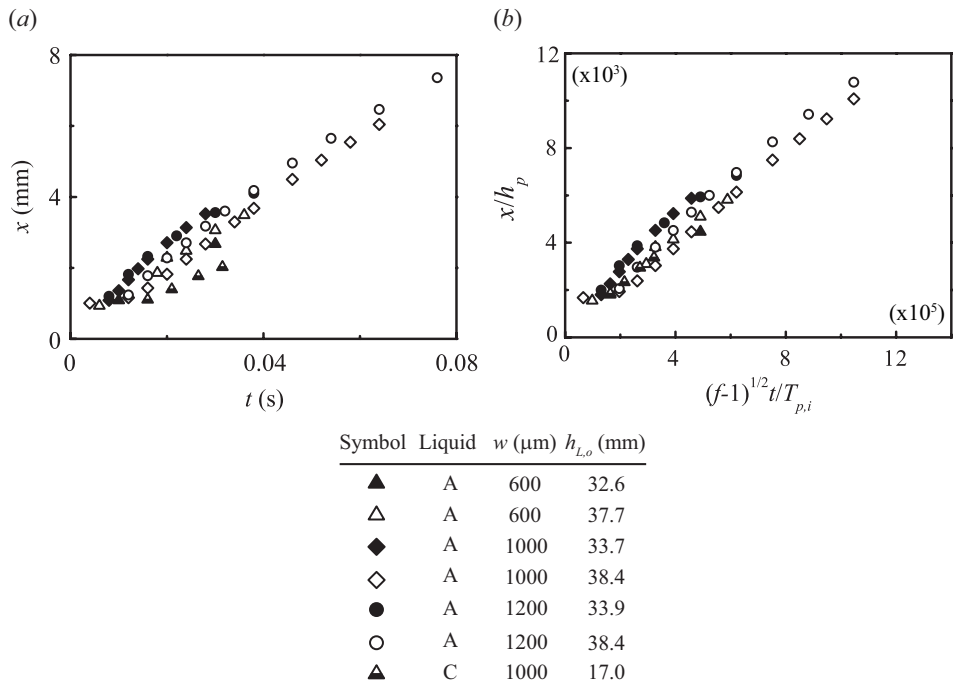


Figure 3.8: Spreading extents of bulk film  $x$  versus time  $t$  (a) Linear plot. (b) Scaled spreading extents  $x/h_p$  versus scaled spreading time  $(f - 1)^{1/2}t/T_{p,i}$  plotted according to the scaling law, where  $T_{p,i}$  is the inertial-capillary time scale, which is defined as  $(\rho h_p^3/\gamma)$ .

### 3.5 Spreading with bulk film

---

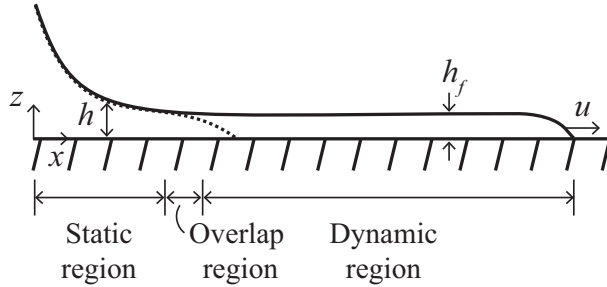


Figure 3.9: Schematic profile of spreading film. The capillary tube influences the film profile near the tube, thus forming highly curved meniscus region (static region). Above the static region, the film is stretched by advancing front, thus leading to relatively constant film thickness (dynamic region).

contact angle  $\theta_a$ , whose value is given by Hoffman-Tanner (Tanner 1979),  $U \sim (1/\ln(R/\lambda))(\gamma/\mu)\theta_a^3$ , where  $R$  and  $\lambda$  are macroscopic and microscopic length scale, respectively and  $\ln(R/\lambda)$  is defined as  $\Gamma$ . In this scaling equation,  $\theta_a$  is scaled by  $h_f/x$  by assuming small  $\theta_a$ , and thus we should know the magnitude of  $h_f$  to complete the previous scaling model.

$h_f$  can be derived by mathematically considering film profile, as illustrated in figure 3.9. Here, we adopt Landau-Levich approaches, which have intensively studied on analysis of film thickness for withdrawing wettable solid surface from stationary liquid (Derjaguin, 1943; Landau & Levich, 1942, 1962; Maleki *et al.*, 2011). Then the film profile can be divided into three different region depending on  $x$ . For small  $x$ , the meniscus is highly curved because the tube strongly affects the film profile, and thus the shape of the meniscus remains relatively constant even if the velocity of the spreading front is zero. For large  $x$ , its relatively flat profile is achieved by the motion of film. Then, for intermediate  $x$ , two region should be overlapped, where the slopes of both regions are smoothly connected. On the static region, the meniscus profile can be written by

$$-\frac{z''}{(1+z'^2)^{3/2}} + \frac{2z}{w} - \frac{\rho g}{\gamma}(h_L - h_J) + \frac{\rho g}{\gamma}z = 0, \quad (3.3)$$

### 3.5 Spreading with bulk film

---

which is derived by considering Young-Laplace equation. On the dynamic region, the profile of the film is relatively flat, thus leading to  $z' \rightarrow 0$ . Then we apply the following asymptotic matching condition.

$$\left(\frac{dz}{dx}\right)_{static}^{x \rightarrow \infty} = \left(\frac{dz}{dx}\right)_{dynamic}^{x \rightarrow 0} = 0. \quad (3.4)$$

Then we can derive the following scaling model of  $h_f$ .

$$h_f \sim \left(\frac{w}{l_c}\right)^2 (h_L - h_J). \quad (3.5)$$

Thus, the scaling model shows that  $h_f$  remains unchanged during the spreading. Experimentally,  $h_f$  varies with  $x$ , but the magnitude of the variation in  $h_f$  is significantly smaller than that of  $h_f$ , and thus  $h_f$  is assumed to be constant. The variation tendencies will be discussed in appendix. The previous scaling model of  $h_f$  can be physically understood by comparing the magnitude of the viscous dissipation and that of the supplying energy. The viscous stress  $\mu\partial^2 u/\partial y^2$  is scaled by  $\mu(U/h_f^2)x$ , and thus we determine the magnitude of the viscous stress, which is much less than the hydrostatic pressure force exerted by the height of liquid column. For this reason, we assume the hydrostatic pressure remains constant in the spreading film, thus leading to  $h_f \sim (w/l_c)^2(h_L - h_J)$  during the spreading phase, which is the exactly same form of the previous mathematical model. Together with this scaling model, the previous scaling law of spreading is given by  $x \sim [\gamma/(\Gamma\mu)]^{1/4}(h_L - h_J)^{3/4}(w/l_c)^{3/2}t^{1/4}$ , where the previous model can be nondimensionalized by using capillary-viscous time scale exerted on  $h_f$ ,  $T_f = \mu h_f / \gamma$  and we can write

$$\frac{x}{h_f} \sim \left(\frac{t}{\Gamma T_f}\right)^{1/4}. \quad (3.6)$$

When we plot the scaled spreading extent  $x/h_f$  according to the scaling law (equation 3.7), the experimental data in figure 3.11(a) are collapsed onto a single master curve, as shown in figure 3.11(b).

By the process of deriving scaling model 3.7, we can figure out the effects of the hydrostatic pressure, which is exerted by the height of liquid column

### 3.5 Spreading with bulk film

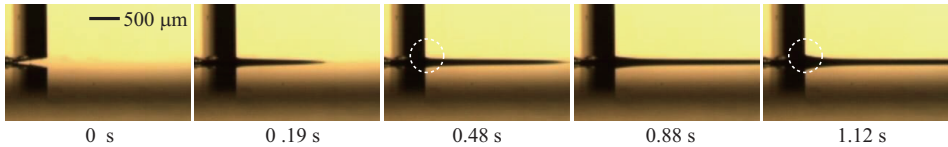


Figure 3.10: High-speed imaging results of film spreading in the capillary bending regime. As time elapses, the curvature near the capillary tube end (dashed circle) is relaxed by forming smooth meniscus between a ridge of liquid film and the tube end.

inside the capillary tube. The hydrostatic force induced by liquid column height does not bring about additional force of pressure gradient inside the spreading film. Instead, the hydrostatic force determines the magnitude of  $h_f$ , as mentioned earlier, and thus plays critical role in relieving viscous shear stress by alleviating the thickness of the spreading film, thus resulting fast spreading for high  $h_L$ .

Next, we compare wetting characteristic depending on the substrate to figure out the effects of  $\Gamma$ . Here we conduct the wetting experiments on the smooth surface and on the prewetted surface, where the same liquid of deposited liquid is precoated by superhydrophilic surface. Figure 3.12(a) shows that the rate of spreading with  $t^{1/4}$  on the prewetted surface is higher than spreading on the superhydrophilic surface and the region of such spreading on the prewetted surface is also longer than spreading on the superhydrophilic rail. Furthermore,  $1/4$  power could not be found in spreading on smooth surface. We attribute these phenomena to  $\Gamma$  in previous scaling model, where the microscopic length, cutoff length, may differs depending on the wetted surface due to the slip length. Based on previous studies, microscopic length on the smooth surface is assumed to be 0.1 nm (de Gennes *et al.*, 2004). For the spreading on the surface with nanoroughness, the liquid spreads not only on the top surface of the pillar (liquid-solid contact) but also on the precursor film between the nanopillars (liquid-liquid contact). Thus, When the liquid is wetted on the precursor part, effective slip occurs during the spreading, thus assuming  $\lambda$  as  $h_p$ . For

### 3.5 Spreading with bulk film

---

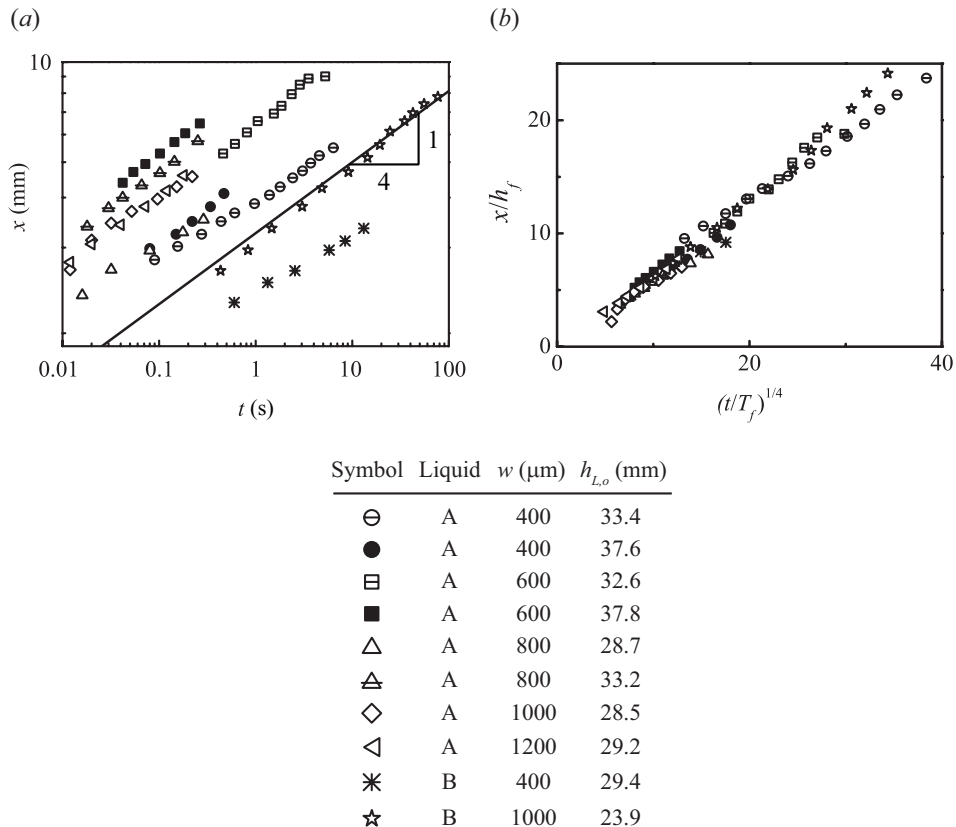


Figure 3.11: Spreading extents of bulk film in capillary bending regime. (a) Log-log plot. (b) The scaled spreading distances  $x/h_f$  plotted according to the scaling law, where  $T_f$  is viscous-capillary time scale,  $\mu h_f/\gamma$ .

### 3.5 Spreading with bulk film

---

the spreading on the prewetted surface, we assume  $\lambda$  as the thickness of prewetted layer, along the same line as mentioned before. When we plot the scaled spreading extents  $x/a$  according to the our model, dispersed data in figure 3.12(b) is reasonably collapsed onto the single curve in figure 3.12(c). Thus, we validate our previous scaling model.

#### 3.5.3 Viscous spreading regime

In this spreading regime, the spreading front is prewetted by the precursor film emitted from the bulk part of the front, as shown in the inset of figure 3.14(a), and the meniscus beneath the tube remains unchanged, which is different aspect of previous regime in bulk film spreading. Thus, we assume that the liquid spreads by balancing capillary pressure and viscous resisting force in the liquid film region, which is shown in the arrow line in the last panel of figure 3.13. Navier-stokes equation associated with lubrication approximation is given by:  $\partial p/\partial x \sim \mu(\partial^2 U/\partial y^2)$ . By considering  $x \gg w$ , the transverse curvature is much higher than the longitudinal curvature, and thus the gradients of capillary pressure is scaled by  $\gamma h_f/(xw^2)$ . Together with aforementioned  $h_f$  relation, we can write the following scaling law by balancing the driving force with the viscous force exerted on  $h_f$ :  $x \sim (\gamma/\mu)^{1/2}(h_L - h_J)^{3/2}(w^2/l_c^3)t^{1/2}$ , where the previous model can also be nondimensionalized by using aforementioned  $T_f$ . Then we can write

$$\frac{xw}{h_f^2} \sim \left( \frac{t}{T_f} \right)^{1/2}. \quad (3.7)$$

When we plot the scaled spreading extents  $xw/h_f^2$  according to the our model, dispersed data in figure 3.14(a) is fairly collapsed onto the single master curve in figure 3.12(b). Although the wetting characteristic differs depending on the deposited surface, we show that the spreading of late stage also seems to be the same, as shown in figure 3.12(a). Clearly, the scaled spreading distance  $xw/h_f^2$  is reasonably collapsed onto single curve, as shown in figure 3.15. Thus it validates our previous assumption and it

### 3.5 Spreading with bulk film

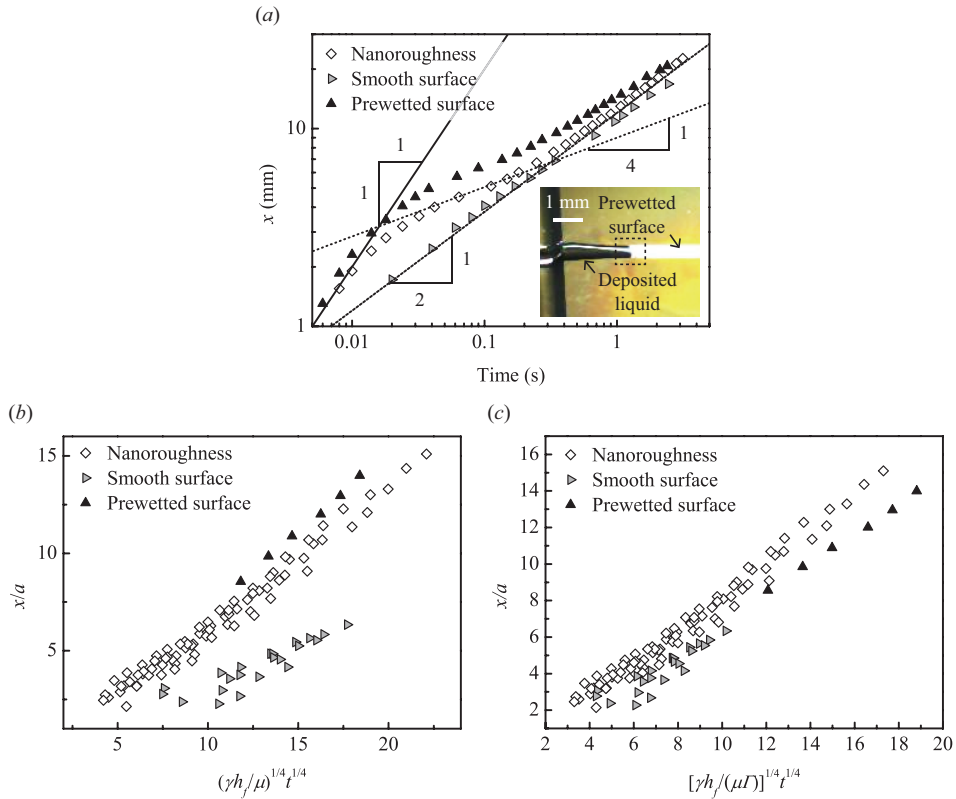


Figure 3.12: Comparison of spreading behaviors depending on the types of substrates. (a) The spreading extents  $x$  versus time for  $[w, h_{L,o}] = [0.8, \sim 35]$  mm. The inset shows spreading of film on a prewetted surface whose thickness is measured to be  $\sim 4 \pm 2 \mu\text{m}$ . The scaled spreading extents  $x/a$  plotted according to the scaling law (b) without considering  $\Gamma$  and (c) with considering  $\Gamma$ .

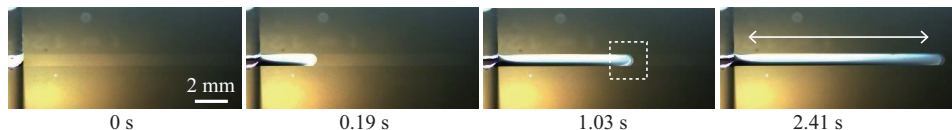


Figure 3.13: High-speed imaging results of film spreading in the viscous spreading regime for  $[w, h_{L,o}] = [1.2, 29.2]$  mm. A bulk film is prewetted by a precursor film, as shown in the dashed box in the third panel. The distance between the bulk and precursor film can be neglected due to the its small length and growth rate.

### 3.5 Spreading with bulk film

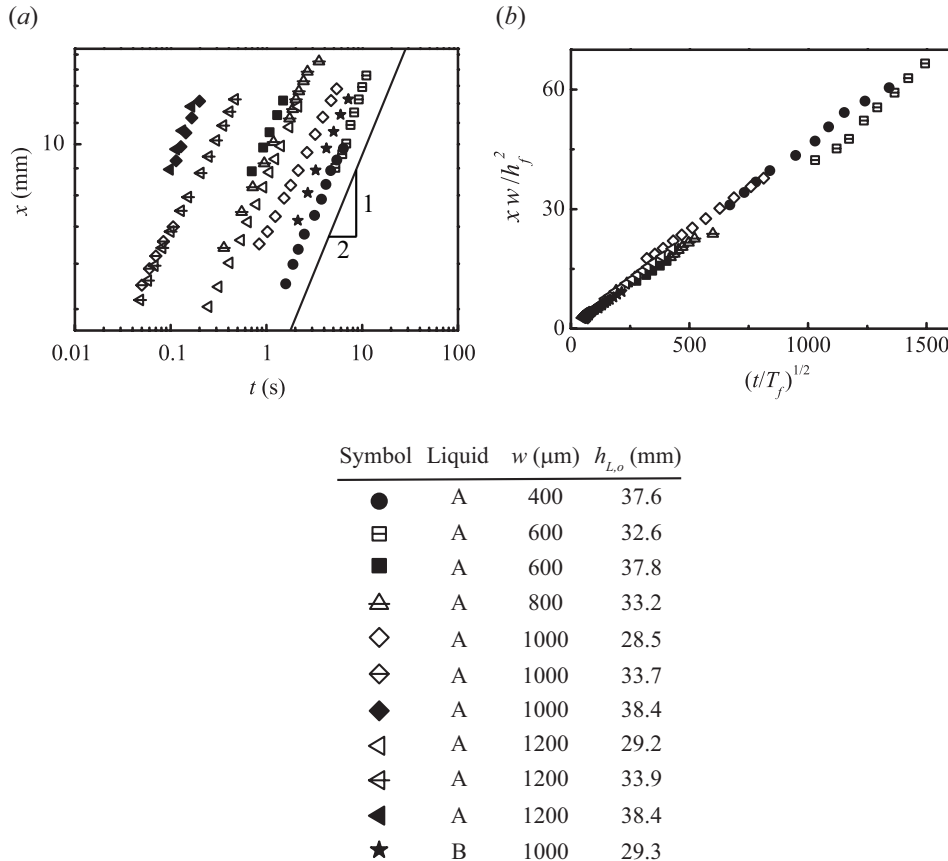


Figure 3.14: (a) Log-log plot of spreading extents  $x$  versus time  $t$  in viscous spreading regime. (b) The scaled spreading extents  $xw/h_f^2$  plotted according to the scaling law.

### 3.5 Spreading with bulk film

---

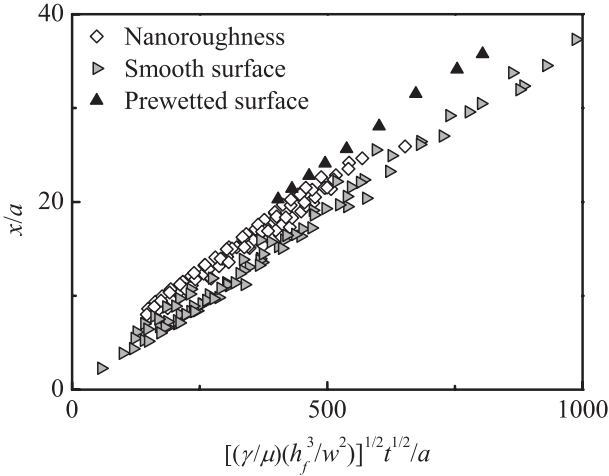


Figure 3.15: The scaled spreading extents  $x/a$  plotted according to the scaling law depending on the characteristic of surfaces.

implies that the contact line does not contribute the driving and resisting force and  $\theta_a$  become a critical value, which remains to be determined.

#### 3.5.4 Characteristic time of bifurcation

The liquid spreadings are fairly described as delineated above, thus there should be crossover points between each regime. Experimentally, inertial regime is always ahead of other regimes because of fast spreading tendencies and the capillary bending regime is followed by the viscous spreading regime. Thus, we analyze characteristic transition time between inertial and capillary bending regime,  $\tau_{i,b}$ , and between capillary bending and viscous spreading regime,  $\tau_{b,s}$  and between the inertial and viscous spreading regime,  $\tau_{i,s}$ . Finally, we can write

$$\frac{\tau_{i,b}}{T_{i,b}} \sim \left( \frac{1}{\Gamma Oh} \right)^{1/3} \frac{h_f}{R_m}, \quad (3.8)$$

where  $T_{i,b}$ ,  $Oh$  are the capillary-inertia time scale and Ohnesorge number, respectively, and scaled by  $\sqrt{\rho R_m^3/\gamma}$  and  $\mu/\sqrt{\rho\gamma R_c}$ , respectively.

In the view of the same approach, we write

$$\frac{\tau_{b,s}}{T_{b,s}} \sim \frac{1}{\Gamma} \left( \frac{w}{h_f} \right)^4, \quad (3.9)$$

### 3.5 Spreading with bulk film

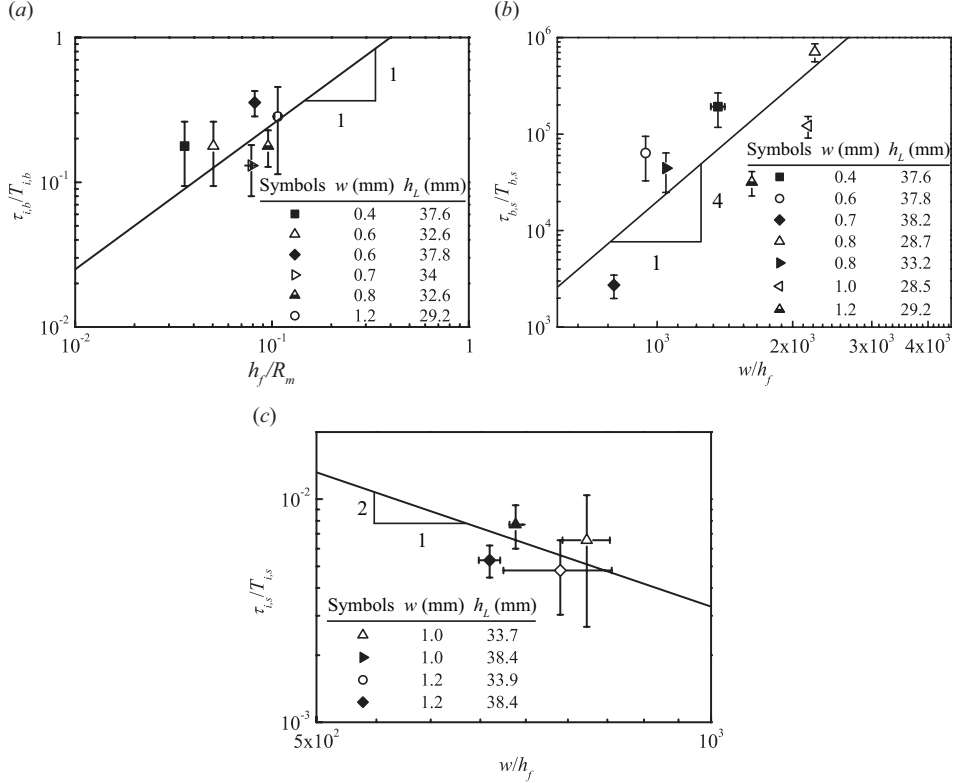


Figure 3.16: Log-log plots of (a) the scaled characteristic inertia-bending time  $\tau_{i,b}/T_{i,b}$  versus dimensionless film thickness  $h_f/R_c$  and (b) the scaled characteristic bending-spreading time  $\tau_{b,s}/T_{b,s}$  versus aspect ratio of film  $w/h_f$  and (c) the scaled characteristic inertia-spreading time  $\tau_{i,s}/T_{i,s}$  versus aspect ratio of film  $w/h_f$ .

where  $T_{b,s}$  is the capillary-viscosity time and scaled by  $\mu h_f/\gamma$ .

We also write

$$\frac{\tau_{i,s}}{T_{i,s}} \sim \left( \frac{h_f}{w} \right)^2, \quad (3.10)$$

where  $T_{i,s}$  is the inertia-viscosity time and scaled by  $\rho R_m h_f/\mu$ . We validate the dependencies of variables in equation 3.8, 3.9, and 3.10 by plotting the scaled characteristic transition time  $\tau/T$  according to the scaling laws, as shown in figure 3.16.

Based on the previous research, we construct regime map, as shown in figure 3.17. Figure 3.17 shows inertial regime can be easily observed

### 3.6 Conclusions

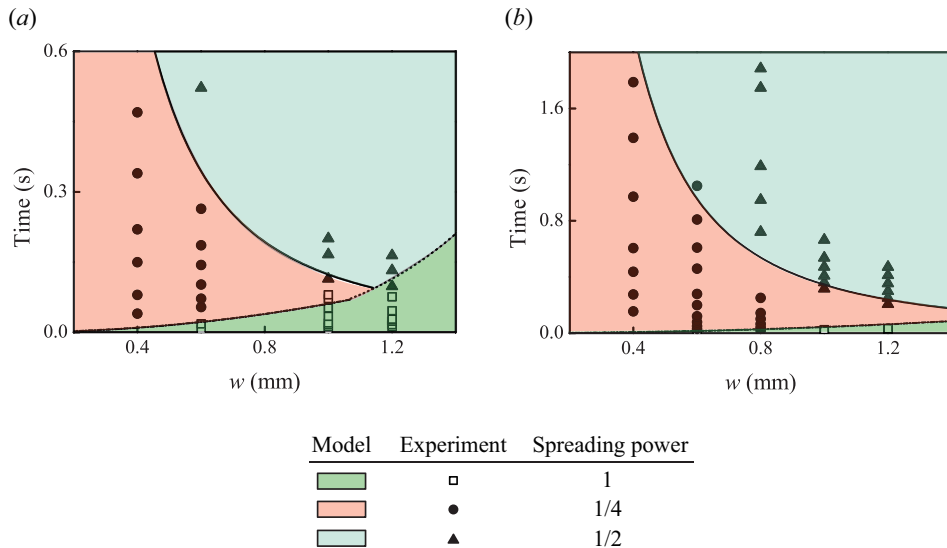


Figure 3.17: The dependence of  $w$  on time scale of characteristic spreading. (a)  $h_{L,o} = 37$  mm. (b)  $h_{L,o} = 33$  mm. As  $w$  decreases, viscous spreading is retarded.

with increase of  $w$ . For narrow stripes, the time scale of inertial regime is so small that we cannot detect such a small time scale spreading and capillary bending is easily achieved and lasted a long time, but it is limited by spreading of precursor film. For wide stripes, inertial force is dominant at the early stage and the spreading eventually falls into viscous spreading regime. When we increase liquid viscosity, the time scale of inertial regime is decreased. Indeed, we cannot be found in inertial spreading by use of aqueous glycerine. Inertial spreading is limited to a short time scale but the resulted spreading distance is sufficiently long due to the fast spreading. Thus, when we draw pattern of liquid by the method introduced in this research, it is important to let  $h_{L,o}$  increase to induce fast spreading.

## 3.6 Conclusions

In this research, we have revealed the hydrodynamics of liquid spreading, which is induced by depositing liquid hanging from a capillary tube.

### 3.6 Conclusions

---

Based on high-speed imaging analysis, the spreading behaviors falls into different regime depending on the thickness of deposited film, which is strongly associated with the width of the superhydrophilic rails and height of the liquid column inside the tube. For the narrow stripes, the resistance due to the small width of the rail does not allow a bulk liquid to penetrate into an entrance of the rail, but a thin precursor film emitted from a stationary the bulk liquid spreads in a such way that the liquid front is imbibed in the gaps of nanopillars, following Washburn's law (Washburn, 1921). By combining experimental and theoretical studies, we present a model for predicting spreading rate of thin precursor film, which is slightly different from classical Washburn's rule. The spreading behaviors are differ depending on the width of superhydrophilic microstripe. For the wide stripes, the bulk liquid entirely spreads along the rails because of the small entrance resistance. In contrast to the spreading of the precursor film, the bulk film spreads with different power laws depending on the spreading extents, which is strongly affected by the liquid column height. Darhuber *et al.* (2001) did not show the dependency of penetration of bulk liquid on the width of hydrophilic microstripes, where they used liquid with low surface tension, thus lowering entrance resisting pressure according to the our previous analysis. When the width of patterns and height of liuiqd column is sufficiently high, the liquid spreads with very fast speed, which results from capillary driving force due to the microscopic curvature at the contact line and it is resisted by inertia force on the spreading film. After this phase, liquid spreads with  $t^{1/4}$  or  $t^{1/2}$ , which are determined from the width of pattern, hydrostatic pressure beneath the tube, and the spreading extents, and we term each regime as capillary bending regime and viscous spreading regime, respectively. Finally, based on the developed model in each regime, we predict the characteristic transition time and construct regime map for predicting spreading behaviors when liquid is brought into contact with superhydrophilic microstripes. Liquid on the hydrophilic microstripes spreads in absence of gravity, and thus this research can be adopted in research field of meniscus climbing at early stage, which is subjected to small

### **3.6 Conclusions**

---

gravity force and also in spreading of drop, whose thickness is below the capillary length of the spreading drop.

# Chapter 4

## Dewetting of liquid film via vapor-mediated Marangoni effect

### 4.1 Introduction

The dewetting of a liquid film on solid surfaces has been the subject of intense study for many decades (Becker *et al.*, 2003; Gabriele *et al.*, 2006; Keller, 1983; Mitlin, 1993; Péron *et al.*, 2012; Redon *et al.*, 1991). The majority of these researches have been conducted on hydrophobic surfaces, where the deposited film easily dewets when a small disturbance is applied to the film. On the other hand, the liquid film intimates with the hydrophilic surface, and thus high disturbance need to cause dewetting motions on the hydrophilic surface. One of such dewetting motions arises from depositing liquid with low surface tension on a lining liquid film with high surface tension, and then a Marangoni stress exerted by mixing of two different liquid leads to the dewetting of deposited film (Gaver, 1990; Jensen & Grotberg, 1992; Troian *et al.*, 1990; Warner *et al.*, 2004). Here, we find that alcohol liquid can induce the Marangoni stress on a deposited water film without mixing of two liquids, thus enabling remotely driven dewetting motion on the wettable solid surface. Remote dewetting motions are

## 4.1 Introduction

---

attributed to the Marangoni effect caused by the alcohol vapor, which we term a "vapor-mediated Marangoni effect".

This vapor-mediated Marangoni effect has been discussed for the droplet movements. Bangham & Sawyer (1938) showed that the water drop can be moved by an acetone drop and they insisted that thin invisible film emitted from the acetone drop changed the solid-gas interfacial tension of the water drop so that the imbalance of the solid-gas interfacial tension around the water drop make the motion of the water drop. Carles & Cazabat (1989) showed that a trans-decaline (TD) drop can be repelled by a polydimethylsiloxane oil (PDMS) drop. They argued that the evaporated TD vapor condenses into the PDMS drop, and thus the gradient of the liquid-gas interfacial tension can be generated, leading to the motion of PDMS drop. The former opinion was supported by Bahadur *et al.* (2009), but these previous studies did not fully present detailed experimental data to validate their assumption. Recently, Cira *et al.* (2015) proposed a different mechanism grounded on the variation in the liquid-gas interfacial tension. They suggested that the vapors evaporated from drops affect the liquid-gas interfacial tension of each other's films formed around the drops, resulting in drop motions due to the nonhomogeneous interfacial tensions of the films. They successfully described the mechanism by visualizing the thin films and flow field inside the drops, but limitations exist in analyzing our observations of vapor-mediated film dewetting, which divided into two different regimes, depending on the deposited film thickness. For a thin film, the vapor allows a bulk of the film to recede by leaving a nanoscale fringe film, which is then dried, thus giving continuous growth of a hole. For a thick film, the dewetting film does not separate into two parts, and the hole grows only to a certain radius.

In the following, we explain the experimental procedures and then show the variation in the interfacial tensions of water with respect to the alcohol concentration. We then report on our observation of two different types of dewetting, which are divided by the film thickness, and consider the crite-

## 4.2 Experiments

---

rion for dewetting behaviors. Finally, we analyze the dynamics of dewetting phenomena by developing corresponding dewetting models.

### 4.2 Experiments

Figure 4.1(a) shows the experimental devices used to observe the dewetting phenomena of a liquid film driven by the Marangoni effect. In this experiment, we first prepared a silicon wafer. The substrate was subsequently immersed in a piranha solution and treated with air plasma to make a hydrophilic surface. The static contact angle  $\theta_e$  of the surface was visually zero even though the surface did not consist of micro- or nano-structures. After we deposited water on top of the substrate, we shook the substrate to make the water spread all over the surface, and we measured the mass of the substrate with a precision balance (Mettler Toledo XS205). The mass was determined from the thickness of the water film on the wafer. The shape was assumed to be cylindrical, and the initial thickness of the water film used in all experiments ranged from 30  $\mu\text{m}$  to 370  $\mu\text{m}$ . A capillary tube containing isopropyl alcohol (IPA) was hung above the water film, where the distance between the capillary end and water film is denoted by  $h_g$ . We observed the following dewetting phenomena which were recorded with a high-speed camera (Photron Fastcam SA1.1) at a frame rate of 60 fps with a resolution of 896  $\times$  896 pixels. The distance from the capillary end to the water interface  $h_g$  ranged from 1 mm to 6 mm. By imaging the geometry of the capillary tubes, the inner radius  $a$  and outer radius  $b$  were determined to be 0.58 mm, and 0.79 mm, respectively.

When we inserted IPA into the capillary tubes, we slightly touched it to the free surface of the IPA enclosed in a large vessel. In all of the experiments, we made the height of IPA in the capillary tubes nearly approach Jurin's height  $h_I = 2\gamma_I \cos \theta_I / (a\rho_I g) = 1 \text{ cm}$  so that the curvature at the bottom of the capillary tubes was almost zero. Thus, we avoided varying the vapor pressure at the bottom region (Butt *et al.*, 2006) to yeild a nearly constant driving force for Marangoni-driven dewetting. Here  $\gamma_I$ ,  $\theta_I$ ,  $\rho_I$ , and

### 4.3 Variation in interfacial tension with alcohol vapor

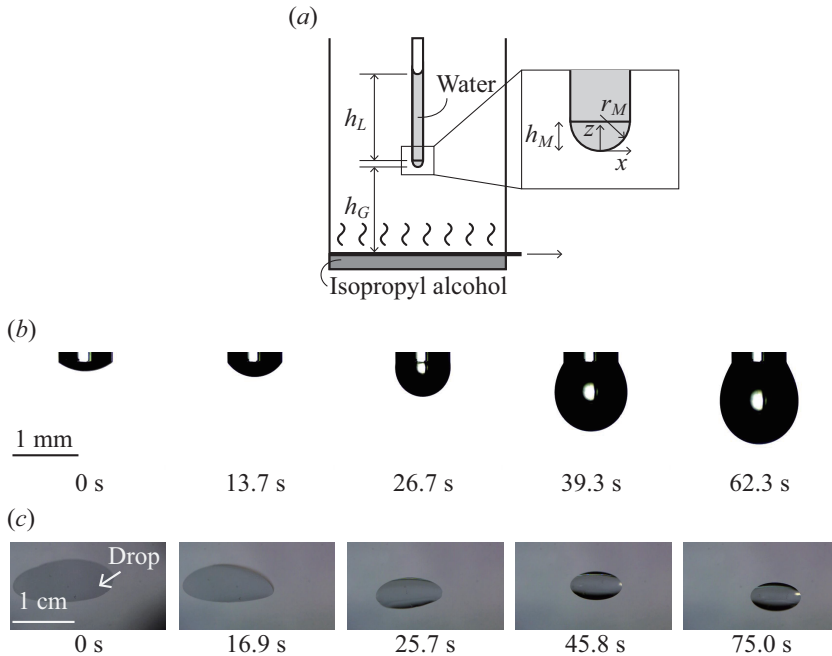


Figure 4.1: (a) Experimental devices to measure the interfacial tension between liquid and gas with different IPA vapor concentrations, where  $h_G$  is the gap distance between the IPA free surface and water surface. (b) Swelling of the water balloon with increasing IPA vapor concentration at  $h_G = 22$  mm. (c) Shrinking of water drop on the substrate at  $h_G = 35$  mm

$g$  are the IPA liquid-gas interfacial tension, contact angle between the IPA and capillary tubes, radius of the capillary tubes, IPA density, and gravitational acceleration, respectively. The corresponding values are 21.7 mN/m,  $0^\circ$ ,  $784$  kg/m<sup>3</sup>, and  $9.8$  m/s<sup>2</sup>, respectively.

### 4.3 Variation in interfacial tension with alcohol vapor

Before considering the Marangoni-driven dewetting phenomena, we analysed how the interfacial tensions varied with the alcohol vapor in order to scrutinise the phenomena discussed in the following sections.

First, we estimated the variation in the liquid-gas interfacial tension

### 4.3 Variation in interfacial tension with alcohol vapor

---

with the alcohol vapor. We placed the IPA liquid and capillary tube containing water into a large vessel and closed valve to keep the IPA vapor from escaping from the bottom of the vessel, as shown in figure 4.1(a). After we opened the valve, the IPA vapor was emitted from the bottom of the vessel and affected the bottom liquid surface of the capillary tube. This changed the interfacial tension between the liquid and gas, which changed the shape of the meniscus. The amount of evaporated IPA vapor increased with the elapsed time, and thus the meniscus shape at the capillary end changed in correspondence, as shown in figure 4.1(b). The change in shape of the meniscus was induced by the competition between the driving force due to the gravitational force and the resisting force due to the surface tension force. In terms of the pressure at the capillary end, the driving force is represented by  $\Delta P_d \sim \rho g h_L$  and the resisting force is given by  $\Delta P_r \sim \gamma/r_M$ . Here  $\rho$ ,  $h_L$ ,  $\gamma$  and  $r_M$  are the water density, water column height inside the capillary tube, water-air interface tension with IPA vapor and radius of curvature at the meniscus for each time step, respectively. Balancing the two terms with a continuity results in  $\gamma \sim \rho g a^{2/3} h_L^{4/3}$ . Thus,  $\gamma$  decreases as the IPA vapor concentration increases because  $h_L$  decreases as the water balloon swells.

Next, we solved the one-dimensional Fick's second law to obtain the concentration of the IPA vapor  $c$  and applied the Young-Laplace equation to predict  $\gamma$ . Then, we related  $c$  to  $\gamma$ , as discussed in appendix A. By using non-dimensional parameters, we plotted  $\gamma/\gamma_o$  and  $c/c_s$  (figure 4.2a), where  $\gamma_o$  and  $c_s$  are the liquid-gas interfacial tension of pure water and the saturated concentration of the IPA vapor, respectively. Figure 4.2(a) shows that  $\gamma/\gamma_o$  abruptly decreased with increasing  $c/c_s$  at a low  $c/c_s$  ( $c/c_s < 0.05$ ). Then  $\gamma/\gamma_o$  reached a relatively constant value at intermediate  $c/c_s$  ( $0.05 < c/c_s < 0.7$ ). This explains that a saturated value of  $c/c_s$  existed, like the critical micelle concentration for surfactant molecules in an aqueous solution. We supposed that the IPA molecules achieved a certain directionality along the water-air interface when they contacted the interface. More

### 4.3 Variation in interfacial tension with alcohol vapor

---

wettable hydroxyl groups of IPA came in contact with the water, which produced less wettable alkyl groups of IPA adjacent to air until the number of IPA molecules was saturated at the water-air interface in the same manner as surfactant monomers. The experiments indeed showed the propagation of tiny waves along the water meniscus which was partly due to the local variation in the liquid-gas interfacial tension on the water-air interface. We represented the IPA-saturated concentration at the water-air interface as the critical concentration  $c_{lg}$ , thus yielding  $c_{lg}/c_s < 0.05$ .

At high  $c/c_s$  ( $c/c_s > 0.7$ ), figure 4.2(a) shows a sharp decline in  $\gamma/\gamma_o$  with increasing  $c/c_s$ . We assumed that the IPA vapor changed the components of air, which caused the water-air interface to collapse and led to  $\gamma \approx 0$ . In this high  $c/c_s$  range, the size of the water balloon did not instantly shrink when we eliminated the IPA vapor. However, at low  $c/c_s$ , the water balloon was promptly restored to its original size as soon as we removed the IPA vapor. We determined that the IPA molecules penetrated the water-air interface and accumulated in the water. Thus, more time was required for restoration at a high  $c/c_s$ .

Figure 4.2(a) shows clear evidence of the decrease in the liquid-gas interfacial tension in the presence of alcohol vapor. This was the first attempt at estimating  $\gamma$  variation when the water-air interfacial tension is affected by IPA vapor.

Next, we conducted experiments to estimate how the solid-gas and solid-liquid interfacial tensions vary with time. We performed the same experiment given above except that we deposited a water drop on the substrate instead of using a capillary tube containing water. The interfacial tensions could not be distinguished individually because they always coexist with a liquid surface. Thus, we compared the contact angle of the water drop  $\theta$  to  $c$ .

Figure 4.2(b) shows that  $\theta$  abruptly increased with  $c/c_s$  at low  $c/c_s$  values. Then, the value of  $\theta$  became relatively constant, much like the early variation shown in figure 4.2(a). This resulted in  $c_{lgs}/c_s \ll 0.01$  and

### 4.3 Variation in interfacial tension with alcohol vapor

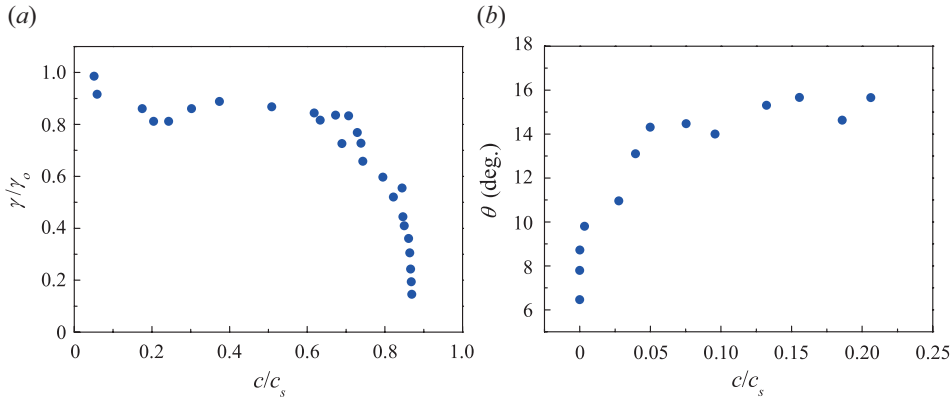


Figure 4.2: (a) Liquid-gas interfacial tension  $\gamma/\gamma_o$  versus IPA vapor concentration  $c/c_s$ . (b) Contact angle  $\theta$  of water drop within mixture of IPA vapor and air  $\theta$  versus IPA vapor concentration  $c/c_s$ .

the saturated contact angle  $\theta_s = 16^\circ$ . Because the solid-liquid and solid-gas interfacial tensions were involved with the increase in  $\theta$ , the critical concentration for  $\theta$  saturation  $c_{lgs}$  differs from  $c_{lg}$  of the water balloon phenomenon. The growth of  $\theta$  can be explained by using Young's equation,  $\gamma \cos \theta = \gamma_{SG} - \gamma_{SL}$ . Here  $\gamma_{SG}, \gamma_{SL}$  are the IPA vapor-affected solid-gas, solid-liquid interfacial tensions, respectively. The variations in  $\gamma_{SG}, \gamma_{SL}$  may be induced from a process similar to that delineated above. Because the substrate was originally covered with a hydrophilic surface, the IPA molecules were also rearranged. To satisfy Young's equation, we should consider not only  $\gamma$ , but also  $\gamma_{SG}$ , and  $\gamma_{SL}$  because only considering the effect of  $\gamma$  results in decreasing contact angle. The experimentally observed variations in  $\gamma$  and  $\theta$  resulted in a decrease of  $\gamma_{SG} - \gamma_{SL}$  and a corresponding reduction in the spreading parameter. Here, we evaluated all of the interfacial tensions at the same time. This is a different approach compared to earlier studies (Bahadur *et al.*, 2009; Bangham & Sawyer, 1938; Carles & Cazabat, 1989), which focused on variations of either  $\gamma$  or  $\gamma_{SG}, \gamma_{SL}$  but not both.

Further increasing the  $c/c_s$  value induced no further increase in  $\theta$ , but we observed oscillation behaviour of the water drop because of small fluctu-

## 4.4 Types of dewetting behavior

---

ations in the local IPA concentration around the drop. When we deposited a pure water drop near the IPA vapor-affected water drop at high  $c/c_s$ , we found that a repulsive motion occurs between the pure water drop and IPA vapor-affected water drop. This implies that the IPA molecules can penetrate the water-air interface, which changes the interfacial tensions of the water.

### 4.4 Types of dewetting behavior

Figure 4.3 shows that the water film can dewet on an extremely hydrophilic surface. In general, a water film cannot recede on a hydrophilic surface because the critical dewetting thickness  $h_c = 2l_c \sin(\theta_s/2)$ , where the capillary length  $l_c = \sqrt{\gamma/(\rho g)}$ , is so small that dewetting phenomena on the hydrophilic surface do not occur spontaneously (de Gennes *et al.*, 2004). It is the gradients of the alcohol vapor that cause the water film to dewet on an extremely hydrophilic surface, where the profile of the IPA molecules can be numerically obtained by solving an unsteady diffusion equation in 3-dimension. Here, we considered all of the geometries including three-dimensional structures, as shown in figure 4.3.

Figure 4.4(a) shows the diffusion of IPA molecules emitted from the inner radius of the tube end  $2a$ . The corresponding initial condition was  $c = 0$ , except for the region of the inner radius of the tube end where the concentration was  $c = c_s$ . Zero concentration and zero flux boundary conditions were imposed at the far-field regions and solid surface of the capillary tube, respectively. We ignored the difference in the receding water film thickness because of the small thickness of the water film and treated the water surface as a solid surface because the diffusion coefficient of IPA in water is much less than that of IPA vapor in air. The diffusion coefficient of IPA in water ranged between  $10^{-6}$  and  $10^{-5} \text{ cm}^2/\text{s}$  (Pratt & Wakeham, 1975) and the diffusion coefficient of IPA in air was measured to be  $0.1 \text{ cm}^2/\text{s}$  at  $25^\circ\text{C}$  Lugg (1968). The diffusion profile of IPA molecules can also be derived by analytically solving Fick's second law in spherical coordinates.

#### 4.4 Types of dewetting behavior

---

By assuming that the emission source of the alcohol vapor is a sphere with a radius of  $R_s$ , we can write

$$c = c_s \frac{R_s}{R} \operatorname{erfc} \left( \frac{R - R_s}{2\sqrt{D_{IPA}t}} \right), \quad (4.1)$$

where  $R$  and  $D_{IPA}$  are the radial distance from the source centre and the diffusion coefficient of IPA vapor in air, respectively. The detailed calculation is presented in the appendix. Figure 4.4(b) compares the numerically obtained IPA molecules profile (markers) with the analytical calculations (lines). These demonstrated reasonable agreement despite the discrepancies between the boundary conditions of the two models. Here,  $r$  is the radial distance along the water film, which leads to  $R^2 = r^2 + h_g^2$ . The fitting parameter  $R_s$  was taken to be 0.46 mm, which was slightly less than the inner radius of the tube.

Figure 4.4(b) presents the variations in the concentration profile with time  $t$  and radial distance  $r$ . Initially, the concentration profile rapidly varied with time. However, figure 4.4(b) shows no significant variation in the concentration profile after 5 s. For low  $r$ , the IPA concentration abruptly decreased with increasing  $r$ . In this low  $r$  range, the interfacial tensions remain unchanged because  $c$  was higher than  $c_{lg}$  and  $c_{lgs}$ , thereby leading to a constant Marangoni driving force during the dewetting of the water film. At high  $r$ , the variation in the IPA concentration became relatively constant, and the IPA concentration eventually fell to zero. In these ranges, we should permit variation in the Marangoni driving force because  $c < c_{lg}$  and  $c_{lgs}$ . However, we can treat the value of the Marangoni driving force as a constant. We explain the conditions that this treatment takes place under the following sections.

When an IPA drop hanging from a capillary tube was situated over a water film deposited on the hydrophilic substrate, we could observe dewetting phenomena which differed depending on the thickness of the initial water film  $h_o$ . For the thin water film ( $h_o$  was on the order of 10  $\mu\text{m}$ ), figure 4.3(a) shows that the thickness of the dewetting water film separated into two different parts, where the bulk part of the dewetting film receded

#### 4.4 Types of dewetting behavior

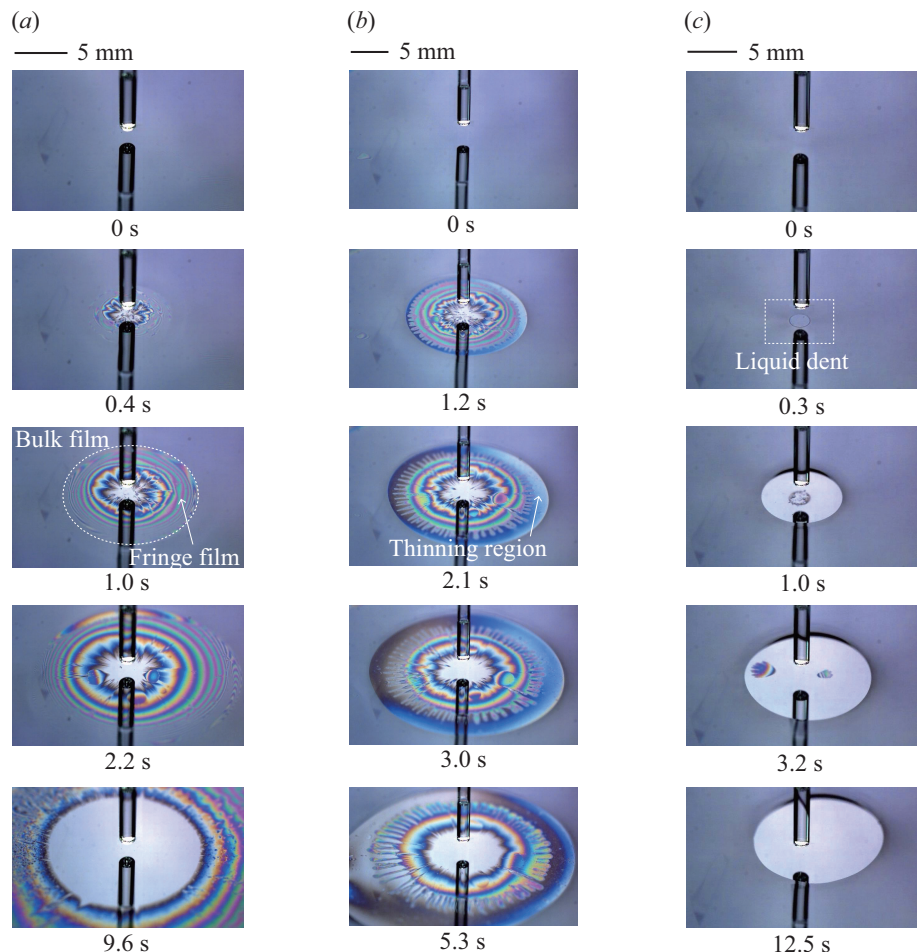


Figure 4.3: Different types of film dewetting driven by Marangoni effect (a)  $h \approx 30 \mu\text{m}$ . (b)  $h \approx 50 \mu\text{m}$ . (c)  $h \approx 270 \mu\text{m}$ .

#### 4.4 Types of dewetting behavior

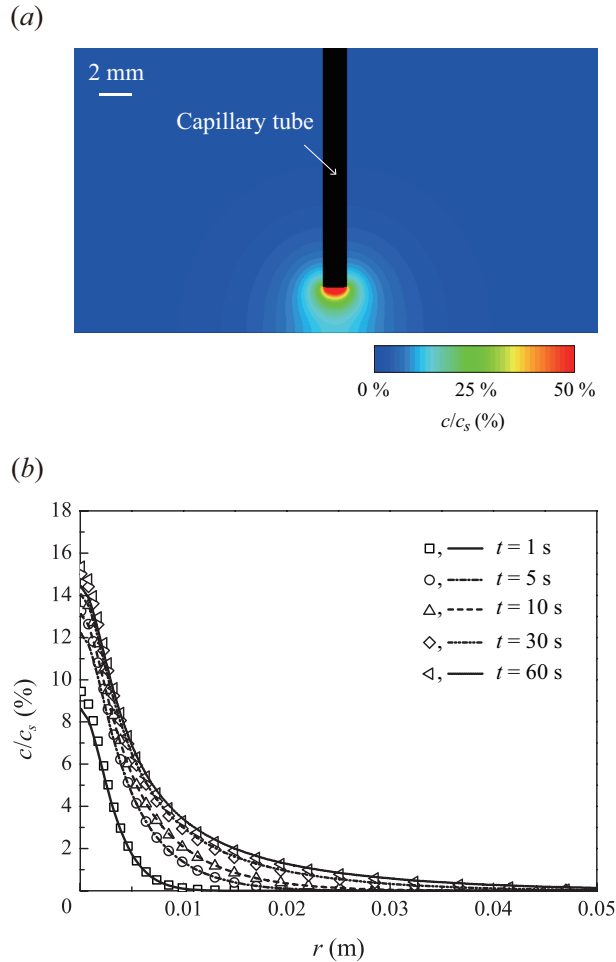


Figure 4.4: (a) Diffusion contour of IPA molecules emitted from tube end at  $[t, h_G] = [5 \text{ s}, 3 \text{ mm}]$ . The time was measured after the IPA molecules were allowed to diffuse out of the tube end. (b) Comparison between diffusion profiles calculated with numerical and theoretical models.

#### 4.4 Types of dewetting behavior

---

immediately (0.4–2.2 s in figure 4.3a). After the sweeping of the bulk part, the fringe film remained because of the strong viscous resisting force. It was spontaneously dewetted by evaporation, which is explained in §4.5.

At the late stage of the thin film dewetting, fingering patterns manifested at the edge of the fringe film. The generation of the finger patterns emerged after formation of a thinning region between the fringe and bulk film, which seems to have been caused by a hydrostatic force from the increased water film thickness during the dewetting process. Figure 4.3(b) shows that such a thinning region could be observed earlier when the initial thickness of the water film increased. This led to the early onset of fingering patterns at large  $h_o$  and the thinning region and length of the fingers grew with the elapsed time. The fingering instability and thinning region induced by IPA vapor have close analogies with a surfactant spreading on thin liquid films (Gaver, 1990; Jensen & Grotberg, 1992; Troian *et al.*, 1990; Warner *et al.*, 2004). In addition to the presence of a thinning region and fingering instability in both phenomena, a similarity was also found on the onset time of finger patterns, which is on order of a few shear time in surfactant spreading (Matar & Troian, 1999a,b). The thinning region eventually ruptured because of evaporation, as shown in the last panel of figure 4.3(b). The thinning region and fingering instability driven by IPA vapor are worthy of further study, but were not further investigated here.

For the thick water film ( $h_o$  was on the order of 100  $\mu\text{m}$ ), the dewetting phenomena not only did not occur as two different films but also took place continuously, as shown in figure 4.3(c). By situating the capillary tube above the water film, we were able to observe the hole nucleation and growth after the delay time (1.0 s in figure 4.3c), which slightly differed depending on  $h_o$ . The radius of the hole was allowed to grow only to a certain radius, where the Marangoni force was balanced with the gravitational force and the hole oscillated with differing the centre of the hole, which is partly due to small fluctuations in the local IPA concentration. When the film thickness was too thick, we could not observe the dewetting phenomena, and we could only see dim liquid dent at the bottom of the capillary tube.

## 4.5 Thin film regime

---

Here, we predict the order of the transition film thickness between the thin and thick film regimes. When the dewetting film belongs to the thin film regime, the bulk part ahead of the fringe film is driven by the difference in the liquid-gas interfacial tension between the IPA vapor-contaminated and -uncontaminated regions. For thick film dewetting, variation in the liquid-gas interfacial tension is not able to dewet the water film, and the water film recedes because of the additional variations in the solid-liquid and solid-gas interfacial tensions. These become involved because of the rupture of the thinning region, as shown in the third panel of figure 4.3(c). Thus, the order of the transition film thickness  $h_{tr}$  can be approximated by balancing the variation in the liquid-gas interfacial force  $\Delta\gamma r$  and the gravitational force  $\rho gh_{tr}^2 r$ , thereby resulting in  $h_{tr} \sim \sqrt{\Delta\gamma/(\rho g)}$ . Considering that  $\Delta\gamma \sim 10^{-2}$  N/m and  $\rho = 10^3$  kg/m<sup>3</sup>, we can obtain  $h_{tr} \sim 100$  μm, which is in reasonable agreement with the experimentally observed transition film thickness. In §4.5, §4.6, we explain the detailed dewetting dynamics in the thin film regime ( $h_o < h_{tr}$ ) and thick film regime ( $h_o > h_{tr}$ ).

## 4.5 Thin film regime

When  $h_o < h_{tr}$ , the dewetting of the water film is separated into two different regimes depending on the water film thickness, as mentioned earlier. The dewetting velocity of the bulk film  $u_b$  is much greater than that of the fringe film  $u_f$ , as shown in figure 4.5. Thus, the fringe film starts receding after sweeping of the bulk film, and thus the fringe film has a delay time  $t_d$  for a hole to open in the film. Figure 4.5(b) shows that  $t_d$  increases with  $h_g$ , which suggests that the hole apparently opens with a certain amount of IPA vapor, whose concentration is larger than  $c_{lg}$ , as shown in figure 4.4(b). After the hole opens on the fringe film, the hole radius (i.e. radius of the contact line  $r_f$ ) continues to increase with  $t - t_d$  and the exponent of the power law is 5/8.

We first consider dewetting dynamics of the bulk film. At the scale of bulk film dewetting velocities, the Reynolds number based on the film thick-

## 4.5 Thin film regime

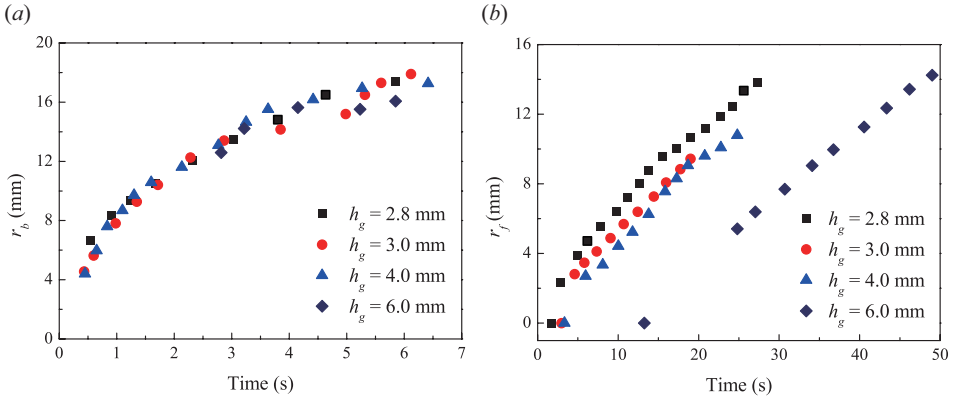


Figure 4.5: Dewetting of thin film regime with  $h_o \simeq 30 \mu\text{m}$ . Temporal evolution of dewetting radius of bulk film (a) and fringe film (b).

ness is much less than unity, and the gravitational effects can be ignored due to  $h_o < h_{tr}$ . Thus, we predicted that the the bulk film dewetting are driven by the Marangoni force and resisted by the viscous force. The bulk part of the dewetting film immediately recedes upon supplying IPA vapor. Despite the disparity in  $h_g$ , the dewetting radius of the bulk film  $r_b$  follows almost the same trajectory as time elapses, as shown in figure 4.5(a). This can be attributed to the nearly constant Marangoni driving force, which is related to the IPA concentration. Figure 4.4(b) suggests that  $c/c_s$  around  $r_b$  stays below 1% at  $h_g = 3$  mm, while  $r_b$  increases to  $\sim 8$  mm at 1 s and  $\sim 15$  mm at 5 s. Equation 4.1 shows that  $c/c_s$  just above  $r_b$  at  $h_g = 3$  mm and at  $h_g = 6$  mm differs by 0.2% at most with  $r_b$  expansion. Thus, we assumed that  $\gamma$  of the fringe film end (i.e. in front of  $r_b$ ) is changed to a nearly constant value regardless of the variation in  $h_g$ , even though  $c$  at the junction of the bulk film and fringe film is less than  $c_{lg}$  as the bulk film recedes. Therefore, we supposed that the fringe film is stretched by the nearly constant Marangoni force with the bulk film dewetted, where the Marangoni force is defined as the difference between the liquid-gas interfacial tension of the IPA vapor-contaminated and -uncontaminated interfaces:  $\Delta\gamma(2\pi r_b) = (\gamma_o - \gamma)(2\pi r_b)$ . Balancing the Marangoni force with the viscous resisting force on the fringe film gives  $u_b \sim 2\Delta\gamma h_f r_b / [\mu(r_b^2 - r_f^2)]$ , where

## 4.5 Thin film regime

---

$r_f$  is the radius of the fringe film. Here, we neglect the viscous resisting force on the bulk part because the shear stress in the fringe film is much higher than that in the bulk film to satisfy continuity equation. The preceding equation can be summarized as  $u_b \sim 2\Delta\gamma h_f / (\mu r_b)$  because  $r_b \gg r_f$  at the same time. Based on the interference patterns on the fringe film, the thickness difference in each blue annulus  $\tilde{h}_f$  in figure 4.3(a) can be scaled as  $\lambda_b / (2n_w)$ , where  $\lambda_b$  and  $n_w$  is a wavelength of blue light and a refractive index of water and the corresponding values are 470 nm and 1.3, respectively. The blue annulus repeated approximately 5 times and thus we deduced that  $h_f$  ranges between 0 and 1  $\mu\text{m}$ , and thereby  $h_f$  was taken to be an average value: 500 nm, where the detailed profile of fringe film will be discussed in this chapter. With  $r_b \in [10^{-3} - 10^{-2}] \text{ mm}$ , as shown in figure 4.5(a),  $u_b$  was estimated to range between 0.9 and 9 mm/s. The experimentally observed  $u_b$  was measured to be  $\sim 3$  mm/s in figure 4.5(a) and fell within the predicted range. Integrating the above equation for  $u_b$  leads to

$$r_b \sim \sqrt{\frac{\Delta\gamma h_f}{\mu}} t^{1/2}, \quad (4.2)$$

where we hypothesized that the Marangoni force is sufficient to reduce the thickness of the water film left by sweeping of the bulk film to a minimum  $h_f$ , which is similar to that suggested by Jensen & Grotberg (1992). Thus, the prefactor  $\sqrt{\Delta\gamma h_f / \mu}$  was taken to be constant regardless of  $h_g$ , thus giving  $r_b \sim t^{1/2}$ . Indeed, our experiments revealed that  $r_b$  scaled as  $t^{1/2}$ , as shown in figure 4.6. Interestingly, the power-law was also found to be applicable to the surfactant spreading Borgas & Grotberg (1988); Lee & Starov (2009), despite being differences between IPA vapor- and surfactant-mediated Marangoni phenomena. The bulk film almost receded to wafer end, but the resultant hole was asymmetry because irregularities took place in the film thickness and the contact line was locally pinned.

Next, we investigate the dewetting dynamics of the fringe film. As mentioned earlier, the fringe film is dewetted like  $(t - t_d)^{5/8}$ , as mentioned earlier, and we cannot find any significant difference in the trajectory of  $r_f$

## 4.5 Thin film regime

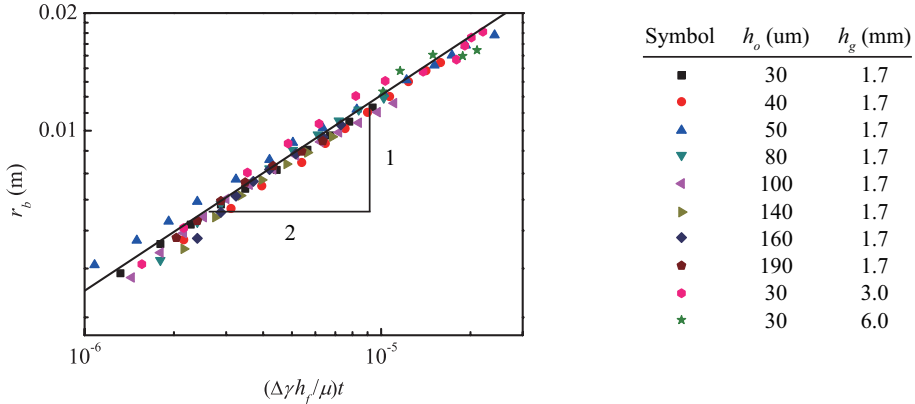


Figure 4.6: The radius of bulk film,  $r_b$  versus time plotted according to our scaling law.

although we change  $h_o$  and  $h_g$ . We assume that it is attributed from self-similarity of fringe film profile and our experimental measurements of fringe film thickness with respect to the radial direction  $r$  do indeed reveal that the thickness profile of fringe film is similar regardless of the variation in  $h_o$  and  $h_g$ , provided that  $t - t_d$  is the same, as shown in figure 4.7. Here, the fringe film profiles are achieved by measuring the color of the interference pattern and corresponding gap distance and thickness (Isenberg, 1992; Kitagawa, 2013).

Except for the dewetting in the very early stages, e.g. the dewetting of the very center, we assumed that the fringe film dewetting is driven by its spontaneous evaporation, in addition to the Marangoni force. We estimated the effective time of evaporation  $t_e$  at which the amount of evaporation of the fringe film becomes comparable to that of dewetting on the film. The evaporative flux is approximately scaled as  $D_w \Delta c_w / \delta_w$ , where  $\Delta c_w$  and  $\delta_w$  are the concentration difference of water vapor across a diffusion boundary and the diffusion boundary thickness given by  $\sqrt{D_w t}$ . Then, the loss of evaporation during the effective time is represented by  $\int_0^{t_e} [(D_w \Delta c_w / \delta)(\pi r_e^2)] dt$ , resulting in  $2\Delta c_w \pi r_e^2 \sqrt{D_w t_e}$ . By balancing the evaporative loss with the amount of a few millimeters dewetting  $\rho \pi r_e^2 \tilde{h}_f$ , we get  $t_e \sim (1/D_w)[\rho \tilde{h}_f / (2\Delta c_w)]^2$ . Here,  $D_w$  and  $r_e$  are the diffusion

#### 4.5 Thin film regime

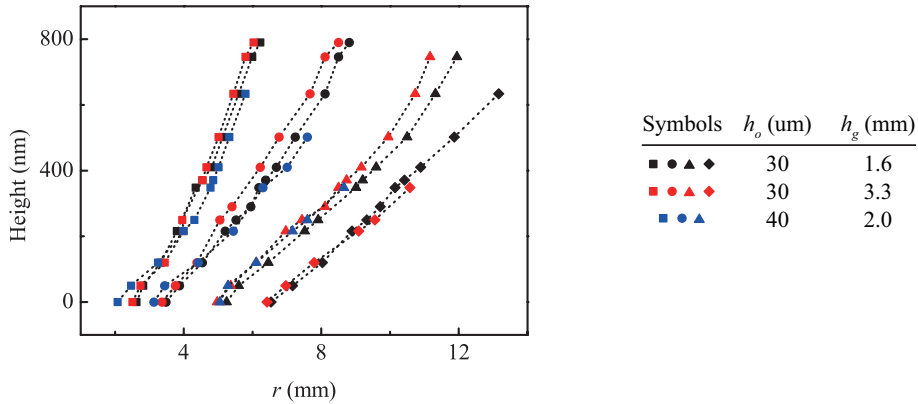


Figure 4.7: The profile of fringe film corresponding to  $t - t_d = 1.0$  s (squares), 2.3 s (circles), 5.0 s (triangles), and 7.5 s (diamonds).

coefficient of water vapor in air and the effective radius of evaporation, respectively. By using the properties of water  $D_w \approx 2.6 \times 10^{-5} \text{ m}^2/\text{s}$  and  $\Delta c_w \approx 7 \times 10^{-3} \text{ kg/m}^3$  (Incropera *et al.*, 2007),  $t_e$  was calculated to be 6 s. The experimental time scale for the dewetting of the fringe film exceeded  $t_e$ , which justifies the argument that the mobility of the fringe film dewetting is based on evaporation.

The diffusion boundary thickness  $\delta_w$  can be scaled by  $\sqrt{D_w(t - t_d)}$ , where  $t_d$  arises from the regrowth of water diffusion boundary layer because the initial boundary layer is convected away from the center during receding of bulk film. As shown in figure 4.7, the fringe film is wedge-shaped in cross-section and thus the height at the distance from the contact line  $dL$  can be scaled by  $dx\theta_R$ , where  $dx$  and  $\theta_f$  are the distance from the contact line and contact angle, respectively. Thus the time to decrease interface level via evaporation  $dt$  can be expressed by  $\rho_w\theta_f\sqrt{t}dx/(\sqrt{D_w}\Delta c_w)$ . Viscous force exerted on the wedge-shaped fringe film can be scaled by  $\mu u_f/\theta_f$ . By balancing the viscous force and Marangoni force, we can obtain the following  $\theta_f$  relation,  $\theta_f \sim (\mu u_f/\Delta\gamma)^{1/3}$ . By combining two equation, we can write

## 4.6 Thick film regime

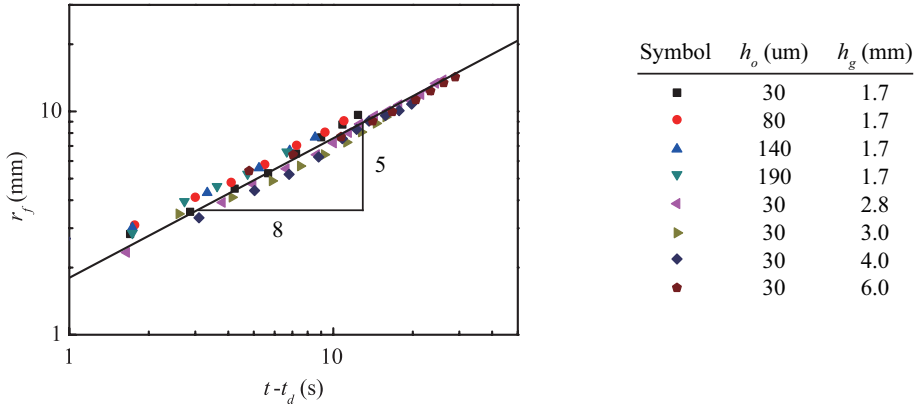


Figure 4.8: The radius of bulk film,  $r_f$  versus time plotted according to the our scaling law.

$$r_f \sim \left( \frac{\Delta\gamma}{\mu} \right)^{1/4} \left( \frac{\sqrt{D_w} \Delta c_w}{\rho_w} \right)^{3/4} (t - t_d)^{5/8}. \quad (4.3)$$

The exponent  $5/8$  is in good agreement with the experimental data, as shown in figure 4.8, but sophisticated verifications of our assumption remain to be revealed.

## 4.6 Thick film regime

Once we attached the source of the IPA vapor, we immediately observed the liquid dent on the center of the water film (0.3 s in figure 4.3c), which was resultant from the variation in the liquid-gas interfacial tension. Then, a junction between the liquid dent and thick film ruptured in a similar manner to the breakup of the thinning region in the thin film regime. The rupture was followed by the hole opening, thus allowing IPA vapor to change the solid-gas and solid-liquid interfacial tensions.

Once the hole emerged, figure 4.3(c) shows that the hole grew with different velocities that differed depending on not only initial thickness, but also time, as shown in figure 4.9. As the size of hole increases, the liquid is pushed away from the center, thus forming a ridge at the rear-side of the hole front. For the early stage of hole growth, the shape of

## 4.6 Thick film regime

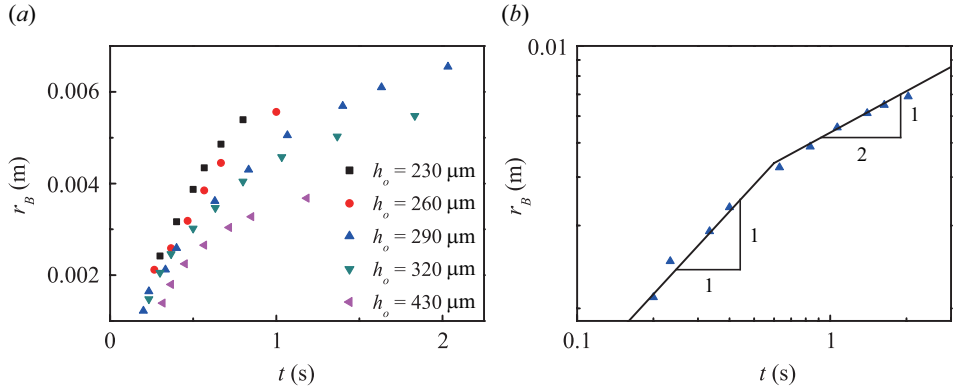


Figure 4.9: The growth of hole radius  $r_B$  versus time. (a) The differences of hole growth depending on the initial film thickness. (b) Hole growth at  $h_o = 290 \mu\text{m}$ , where the power laws of hole radius change from  $r_B \sim t$  to  $r_B \sim t^{1/2}$ .

ridge maintains its circular shape, but, for the late stage of hole growth, the maximum height of the ridge exceeds the critical height  $h_c$ , which is defined as  $h_c = 2l_c \sin(\theta_e/2)$ , and thus the ridge flattens. Previously, we show that IPA vapor alter the inherent contact angle  $\theta_e$ , and thus initially fully wetting surface is changed into partial wetting ( $\theta_e \simeq 15^\circ$ ), resulting in  $h_c \simeq 700 \mu\text{m}$ .

We first consider the early stage of hole growth. Here, we follow the description of Redon *et al.* (1991) and then we derive the following relation,  $\mu \dot{r}_B / \theta_d \sim \gamma (\theta_e^2 - \theta_d^2)$ , where  $r_B$  and  $\theta_d$  are the front radius of the hole and dynamic contact angle of the ridge. This equation is valid at the front of the ridge. Similarly, we can get the relation satisfying force balance at the rear end of the ridge,  $\mu(r_B + l) / \theta_d \sim \gamma \theta_d^2 - \rho g h_o^2$ , where  $l$  is the horizontal length of the ridge. By assuming  $\dot{r}_B \gg l$  and summing the previous two equations, we can write

$$r_B \sim \frac{\rho g}{\mu} (h_c^2 - h_o^2) \theta_e t. \quad (4.4)$$

When we plot the radius of the hole  $r_B$  according to the our model, dispersed data in figure 4.9(a) is fairly collapsed onto the single master

## 4.6 Thick film regime

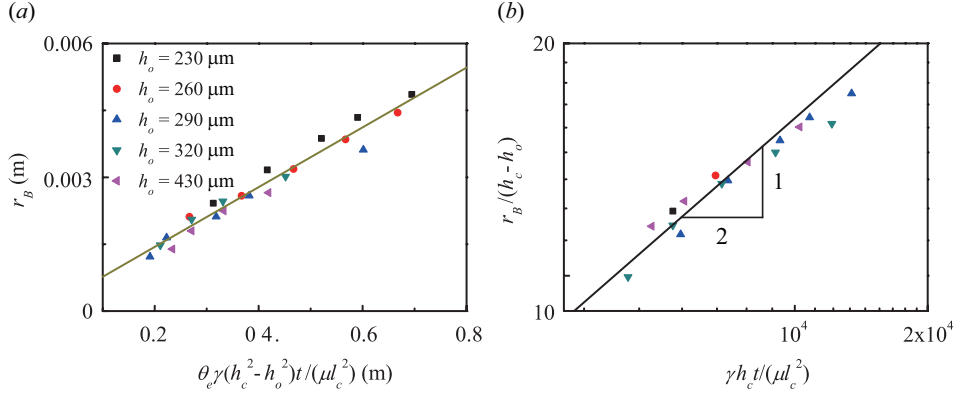


Figure 4.10: (a) Early-stage growth of hole radius  $r_B$  versus time plotted according to the our scaling law. (b) Late-stage growth of the scaled hole radius  $r_B / (h_c - h_o)$  versus time plotted according to the our scaling law.

curve in figure 4.10(a).

Next, we analyze the late stage of hole growth. The driving force can be scaled by  $\gamma \theta_e^2$ , which is derived in a similar way to the process delineated above while the resisting force differs from the previous model. For this stage, ridge eventually flattens, as mentioned earlier, and thus the viscous resisting force is scaled by  $\mu(l/h_c)r_B$ . Then, total resisting force can be obtained by considering the gravitation force exerted by thick  $h_o$ . By balancing the driving and resisting force together with volume conservation law,  $l = r_B h_o / (h_c - h_o)$ , we can get

$$\frac{r_B}{h_c - h_o} \sim \sqrt{\frac{\gamma h_c}{\mu l_c^2}} t^{1/2}. \quad (4.5)$$

When we plot the scaled radius of the hole  $r_B / (h_c - h_o)$  according to the our model, dispersed data in figure 4.9(a) is fairly collapsed onto the single master curve in figure 4.10(b).

The size of hole continuously grows until its radius reached a certain distance that differed depending on the thickness of the water film, as shown in figure 4.11(a). Then it oscillated continuously as its center simply varied (3.2-12.5 s in figure 4.3c), where the amplitude was much less than the

## 4.6 Thick film regime

---

maximum radius of the hole. This oscillatory behavior seems to have been due to the local variation in the IPA vapor. Here, the maximum radius of the hole  $r_{B,m}$  was adopted by averaging the radius of the oscillated hole. When the radius of the hole approached  $r_{B,m}$ , the hole radius maintained a relatively constant value despite further changes in  $h_g$  because the IPA concentration became relatively constant at such a high radius and the critical concentration was already exceeded. Therefore, our experiments showed no strong relationship between  $h_g$  and  $r_m$ . When we removed the source of the IPA vapor, the IPA vapor disappeared on the water film because it diffused into the region with a lower concentration. The interfacial tensions, therefore, were restored to the original properties of water, and thus the force of gravity immediately closed the hole, as shown in figure 4.11(a).

To estimate  $r_m$ , we compared the Marangoni forces and the gravitational force of the film when the radius of the expanding hole reached  $r_m$ . For this static motion, we can adapt Young-Laplace equation, where the capillary term is exerted by radial and circumferential curvature of the hole meniscus and the pressure term arises from the hydrostatic force. This yielded  $\rho gh \sim \gamma(h/\Delta^2 - 1/r_{B,m})$ , where  $h$  and  $\Delta$  are the film thickness increased by hole expansion and length of the hole meniscus in the radial direction, respectively. By summarizing the scaling model, we can get

$$\frac{l_c}{r_{B,m}} \sim \left( \frac{l_c^2}{\Delta^2} - 1 \right) \frac{h}{l_c}. \quad (4.6)$$

Experimentally,  $\Delta$  was relatively constant regardless of  $h_o, r_{B,m}$  and calculated to be on the order of  $10^{-3}$  m, which was confirmed by imaging the width of the meniscus in figure 4.3(c). When we plot the scaled maximum radius of the hole  $l_c/r_{B,m}$  according to the our model, we can show that experimentally observed power law of hole radius is in good agreement with theoretical scaling model, as shown in figure 4.11(b). For small  $r_{b,m}$ , hole was abruptly closed. It seems to occur when the contact angle exceed the advancing angle.

When  $h_o$  was larger than  $\sim 380 \mu\text{m}$ , we could not observe the dewetting phenomena because of the large gravitational resisting force of the water

## 4.7 Conclusions

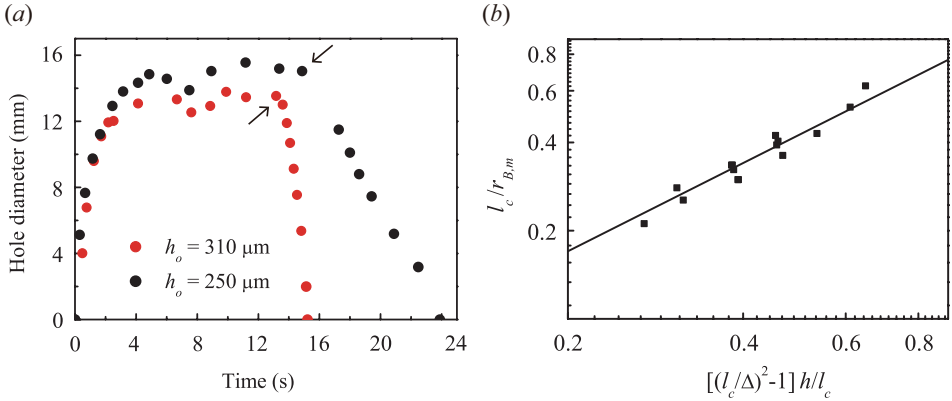


Figure 4.11: (a) Dewetting of thick film with  $h_g = 2 \text{ mm}$  for different initial film thicknesses. The arrows indicate the moment that the source of the IPA vapor was detached. (b) Log-log plot of the scaled maximum hole radius  $l_c/r_{B,m}$  versus film thickness plotted according to the our scaling law.

film. We could only see dim liquid dent just below the source of the IPA vapor, which resulted from the Marangoni force  $\Delta\gamma$  and whose thickness was close to the original thickness of the uniform film. The lowest  $h$  was measured to be  $\sim 100 \mu\text{m}$  in figure 4.11(b), which is in agreement with  $h_{tr}$ .

## 4.7 Conclusions

We showed that film dewetting driven by the Marangoni effect reveals novel dynamic behaviour that differs from that on a hydrophobic surface. The thin film is continuously ruptured by the IPA vapor; the bulk part is dewetted by the IPA vapor, but the fringe part is dewetted by spontaneous evaporation. The thick film also recedes when the source of the IPA vapor is situated over the water film, thereby making a hole in it. However, the hole only grows to a certain radius, at which point the gravitational force is balanced with the interfacial forces and capillary forces. By obtaining the diffusion profile of the IPA vapor, we analysed the relationships between the IPA concentration and interfacial tensions to suggest scaling laws that predict the rate of the bulk film dewetting in the thin film regime and the

## 4.7 Conclusions

---

dependence of the film thickness on the maximum radius of the hole in the thick film regime. It is noteable that the variation in the magnitude of the interfacial tensions can be increased by decreasing the chain length of the alcohol (Jin *et al.*, 2012), thus implying a higher Marangoni stress for light weight alcohols. Indeed, Our experiments showed that the maximum radius mediated by ethanol vapor was found to be increased by 23% compared to the maximum radius mediated by IPA vapor at  $h = 300 \mu\text{m}$ .

The vapor-mediated Marangoni effect also causes other interesting phenomena. We found that water drops seated on superhydrophobic pillars undergo a transition from the Cassie-Baxter to Wenzel states, thus lowering their contact angles. On the hydrophilic surface, we also found that the water drops move away from the source of the alcohol vapor when the alcohol source is hung millimeters over the water drops, which is similar to the phenomenon of chasing drops (Bahadur *et al.*, 2009; Carles & Cazabat, 1989; Cira *et al.*, 2014). Bahadur *et al.* (2009) attributed this phenomenon to a very thin invisible film emitted from one drop, and thus the chasing phenomenon does not take place when each drop is closely placed but located on separated substrates. Here, we demonstrated that the chasing phenomenon occurs even if each liquid is separated, thus elucidating the correct physical origin of the vapor-mediated motions.

In summary, we suggest that it is important to consider the variation in all interfacial tensions to understand vapor driven-Marangoni phenomena. Our research is potentially applicable to water removal industries. By suppressing viscous effects, alcohols can remove water drops and films without requiring any strong flow or physical contact.

# Chapter 5

## Concluding remarks

### 5.1 Conclusions

In this thesis, we have presented the salient characteristics of thin liquid film and the hydrodynamics under the gradient of interfacial energy. Parametric study and scaling analysis have been performed to figure out the physics of thin film. Based on the understanding, we showed that the shape of the deposited film was precisely controlled. The first two chapters mentioned thin film hydrodynamics under the gradient of the liquid-solid interfacial energy, and the remaining chapter did of the liquid-gas interfacial energy.

In chapter 2, we presented the high-speed imaging results of the motion of impacting drops on a superhydrophilic annulus surrounded by a superhydrophobic area. It was found that when a drop having a volume larger than a critical value maintained a spherical cap shape on the wettability-contrast pattern, which we term a liquid lens. Spontaneous morphological transition could be triggered by letting the drop evaporate on the surface, leading to reduction of liquid lens volume. The lens burst because the evaporating lens became unstable when its volume reached a certain threshold value, which we estimated in the previous section. Once hole emerged, it expanded until liquid film on the inner superhydrophobic region bounced off the solid surface by transforming into a drop. Here we provided hydro-

## 5.1 Conclusions

---

dynamic analysis for bursting speed on inner superhydrophobic region and take-off angle of jumping drop.

In chapter 3, we suggested an alternative liquid patterning method where liquid was written by spreading phenomena. When a liquid hanging from a capillary tube was deposited on the superhydrophilic microstripe, a variety of spreading behaviors could be obtained depending on the width of the wettable stripe and supplying pressure. For very narrow stripes, the resistance due to the small width of the rail did not allow a bulk liquid to enter the rail. Instead, a thin film penetrated into the gaps of nanopillars, following Washburn's law. For relatively wide stripes, the bulk liquid entirely spread along the stripe because of the small entrance resistance. The bulk spread with power laws different from Washburn's law, where the spreading rate depended on the liquid column height. By combining experimental and theoretical studies, we presented various spreading models for predicting spreading rate on superhydrophilic microstripe. Based on the developed models, we constructed regime map for predicting spreading behaviors. Thus, we could manipulate spreading rate by controlling the width of superhydrophilic microstrips and supplying pressure.

In chapter 4, we showed that a hole was punctured on the liquid film via IPA vapor, which generated the gradient of the liquid-gas interfacial energy. The size of the hole was strongly affected by the thickness of deposited film, and thus the dynamic behaviors were differed depending on the film thickness. The thin film was continuously ruptured by the IPA vapor; the bulk part was dewetted by leaving the fringe part, which was dewetted by spontaneous evaporation. The thick film also receded when the source of the IPA vapor was placed over the water film, thereby making a relatively stationary hole whose size was determined from the thickness of the deposited film. By analyzing the relationships between the IPA concentration and the interfacial tensions, we developed scaling laws for predicting the increase rate of the hole for the thin film and the size of relatively motionless hole for the thick film.

## 5.1 Conclusions

---

Based on these researches, we can precisely control not only the morphologies of thin liquid film by manipulating the liquid-solid interfacial energy, but also size of punctured hole by varying the liquid-gas interfacial energy. Still, limitations exist in extending ranges of liquids. For patterning a certain morphology of thin film under gradient of the liquid-solid interfacial energy, high viscous liquid, including conducting liquids, biological fluids, and polymers, cause a problem with generating the desired film shape. Patterning followed by film rupture, as shown in chapter 2, failed to the engagement of the liquid film on the inner hydrophobic region due to the viscous dissipation in rupture process. The spreading, as shown in chapter 3, was retarded, and thus we need more time to obtain the desired liquid pattern. For puncturing the hole in thin film under gradient of the liquid-gas interfacial energy, as shown in chapter 4, a liquid with low surface tension was ineffective for the hole patterning. Therefore, this method is limited to the liquid with high surface tension, such as water and other aqueous liquids.

These researches can be applied to the industry of patterning electronic circuit. In this field, the patterning conventionally require photolithography process, which cause the increase of production cost due to the significant expense of raw materials and management of toxic effects. To remove the deteriorating process, patterning via direct printing has been developed, but many studies have usually focused on inkjet-based technologies (Huang *et al.*, 2011; Kim *et al.*, 2009). Here, we presented novel methods of direct patterning, which can be adapted in alternative ways of direct printing, in addition to the inkjet-based patterning.

Our studies can also be used to analyze the rupture dynamics of a tear film, which protects invasion of dust particles in the air onto an ocular surface (Dilly, 1994). The tear film with the thickness less than a few nanometer can be stable, but the film can be ruptured above the thickness larger than several hundreds micrometer when the hydrophilic corneal surface becomes hydrophobic due to contamination of the mucin layer, leading to dry eye syndrome (Holly, 1973; Johnson & Murphy, 2004). The contamination

## **5.2 Future work**

---

seems to occur nonuniformly and thus we attribute the tear film rupture to the local hydrophobicity of corneal surface. We revealed the threshold thickness of film rupture on the nonhomogeneous wettability surface and our studies will therefore be helpful in analyzing the dynamics of tear film rupture.

## **5.2 Future work**

In this thesis, we have focused on the behaviors of thin film on the solid surface under the gradient of the interfacial energies. For the thin film studies under the gradient of the liquid-solid interfacial energy, we have analyzed thin film dynamics on the high gradient of the liquid-solid interfacial energy. Although the energy gradient is slightly diminished, we find that the novel dynamics such as bursting and spreading still occurs and thus more studies are needed to clarify film behaviors on the low wettability gradient surface and critical gradient value. For the thin film studies under the gradient of the liquid-gas interfacial energy, our analysis is mainly based on the macroscopic view, thus failing to interpreting emergence of thinning region and fingering. Because of film with thickness less than a few hundreds nanometer, disjoining pressure such as van der Waals force should be involved. Thus, microscopic approaches remain to be pursued in the future.

## Appendix A

# Dynamic thickness of bulk film

As mentioned in chapter 3, the thickness of spreading film consist three different regions, as shown in figure A.1, and the film thickness of dynamic region  $h_f$  changes with the spreading extents  $x$ . Here, we discuss the dynamic thickness of  $h_f$ .

By combining continuity equation and stokes equation applied by Young-Laplace equation can be written as

$$\frac{\gamma}{3\mu} h^3 \frac{d^3 h}{dh^3} = u(h + C), \quad (\text{A.1})$$

where  $\gamma$ ,  $\mu$ ,  $h$ ,  $u$ , and  $C$  are surface tension, viscosity, film thickness in the overlap region, coefficient of reflecting flow deficiency between the contact line and film. When  $h \rightarrow h_f$ ,  $d^3 h / dh^3$  goes to zero, and thus  $C$  is calculated to be  $-h_f$ . We can define the following nondimensional variable,  $\eta = h/h_f$  and  $\xi = x/h_f(3Ca)^{1/3}$ , where  $Ca$  is capillary number,  $Ca = \mu u / h_f$ . Then we write the previous equation as the nondimensionalized equation,

$$\frac{d^3 \eta}{d\xi^3} = \frac{\eta - 1}{\eta^3}. \quad (\text{A.2})$$

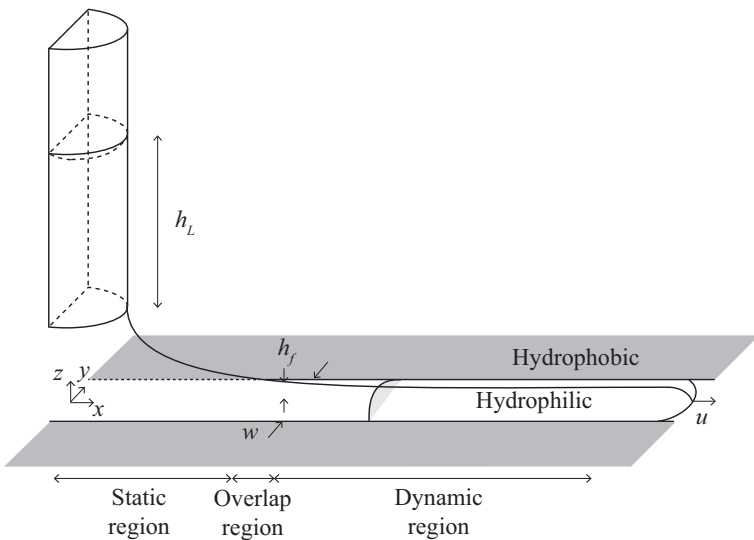


Figure A.1: Schematic of spreading film emitting from a tube on hydrophilic microstripe. A curved and relatively flat meniscus are formed depending on a spreading extents  $x$ , and thus static, dynamic, and overlap region is existed.

---

We use asymptotic matching condition in a similar way to the process delineated in chapter 3, but, here, we match the second derivative as the following:

$$\left(\frac{d^2\eta}{d\xi^2}\right)_{static}^{\eta \rightarrow \infty} = \left(\frac{d^2\eta}{d\xi^2}\right)_{dynamic}^{\eta \rightarrow 0} = \alpha, \quad (\text{A.3})$$

where the curvature of the static and dynamic region is assumed to be a certain value,  $\alpha$ .  $z''$  at  $\eta \rightarrow \infty$  can be given by  $z'' \sim (h_L - h_J)/l_c^2$ , which is obtained from film profile equation in chapter 3.  $z''$  at  $\eta \rightarrow 0$  can be written as  $z'' = (1/h_f)(3Ca^{2/3})d^2\eta/d\xi^2$ . Then, we can obtain the final formula of  $h_f$ .

$$h_f \sim \frac{l_c^2}{h_L - h_J} Ca^{2/3}, \quad (\text{A.4})$$

which is slightly different from the classical Landau-Levich-Derjaguin formula (Derjaguin, 1943; Landau & Levich, 1942, 1962). The dispersed experimental data in figure A.2(a) is collapsed onto a single master curve in figure A.2(b) even if  $h_f$  varies with  $x$ .

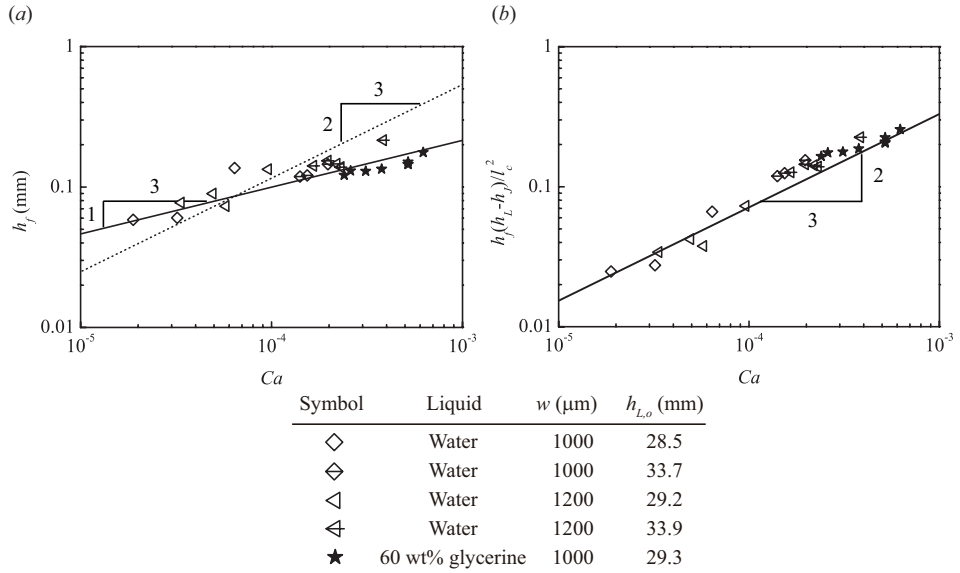


Figure A.2: Log-log plot of (a) dimensional film thickness  $h_f$  plotted according to capillary number  $Ca$ , and (b) the scaled film thickness  $h_f(h_L - h_J)/l_c^2$  plotted according to the scaling law. Plot legends as in the bottom.

## Appendix B

# Relation between alcohol vapor and liquid-gas interfacial tension

By solving the one-dimensional Fick's second law with Dirichlet boundary conditions defining  $c = c_s$  at the free surface of IPA and  $c = 0$  at the infinite distance from the free surface, we can write

$$c = c_s \left[ 1 - \operatorname{erf} \left( \frac{h_G}{2\sqrt{D_{IPA}t}} \right) \right], \quad (\text{B.1})$$

where  $h_G$  is the distance from the free surface of the IPA liquid to the water meniscus. Then, we can solve the Young-Laplace equation to obtain the meniscus profile at each time step, as shown in figure 4.1(b). The governing equation is represented as

$$\frac{d^2z}{dx^2} = \frac{\rho g}{\gamma} (h_L + h_M - h_J - z) \left[ 1 + \left( \frac{dz}{dx} \right)^2 \right]^{3/2} - \frac{1}{x} \frac{dz}{dx} \left[ 1 + \left( \frac{dz}{dx} \right)^2 \right], \quad (\text{B.2})$$

where  $h_J$  is Jurin's height of water, and we use the boundary conditions  $z = 0$  and  $dz/dx = 0$  at  $x = 0$  because of the symmetry of the meniscus. By

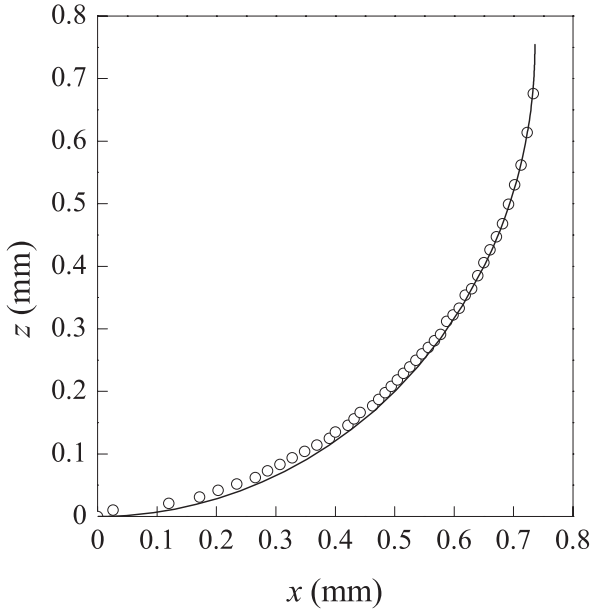


Figure B.1: Comparison between meniscus profiles from image analysis (solid lines) and Young-Laplace equation (circles).  $[h_G, h_L, c/c_s] = [20.3 \text{ mm}, 34.0 \text{ mm}, 0.44]$ .

assuming  $\gamma$ , we can compare the experimentally obtained meniscus profile with the calculated values as shown in figure B.1. The experimental and calculated values showed good agreement.

In each time step,  $\gamma$  is assumed so that the maximum differences between the experimental and calculated values over the outer radius of the capillary tube are less than 7%. The largest errors take places near  $dz/dx \simeq \infty$ .

## Appendix C

# Distribution of alcohol vapor emitted from source in spherical coordinates

Consider a spherical source emitting alcohol vapour, where the radius of the source is  $R_s$  and the surface concentration maintains the saturated concentration  $c_s$ . The concentration is initially zero at  $R > R_s$ . The diffusion equation in spherical coordinates is

$$\frac{1}{R^2} \frac{\partial}{\partial R} \left( R^2 \frac{\partial c}{\partial R} \right) = \frac{1}{D_{IPA}} \frac{\partial c}{\partial t}, \quad (\text{C.1})$$

and the corresponding boundary conditions are  $c(R, 0) = c(\infty, t) = 0$ ,  $c(R_s, t) = c_s$ . By applying the Laplace transform. we can write

$$\frac{1}{R^2} \frac{\partial}{\partial R} \left( R^2 \frac{\partial c^*}{\partial R} \right) = \frac{s c^*}{D_{IPA}}, \quad (\text{C.2})$$

and the transformed boundary conditions are  $c^*(R = R_s) = c_s/s$ ,  $c^*(R = \infty) = 0$ . Here,  $s$  is the transform parameter, and  $c^* = \int_0^\infty \exp(-st) c dt$ . When we apply  $c^*$ , which is assumed by  $R^{\alpha_1} \exp(-R^{\alpha_2})$  with  $\alpha_1$  and  $\alpha_2$

---

being fitting parameters, to the above equation, the solution that satisfies the above equation is

$$c^* = \frac{A_1}{R} \exp(-\sqrt{s/D_{IPA}}) + \frac{A_2}{R} \exp(\sqrt{s/D_{IPA}}), \quad (\text{C.3})$$

where  $A_1$  and  $A_2$  are integration constants. By applying the boundary conditions, we obtain  $A_1$  as  $(c_s/s)R_s \exp(\sqrt{s/D_{IPA}}R_s)$  and  $A_2$  as 0. Thus,

$$c^* = \frac{c_s}{s} \frac{R_s}{R} \exp[-\sqrt{s/D_{IPA}}(R - R_s)]. \quad (\text{C.4})$$

$c(R, t)$  can be obtained by an inversion process to result in

$$c(R, t) = c_s \frac{R_s}{R} \operatorname{erfc} \left( \frac{R - R_s}{2\sqrt{D_{IPA}t}} \right). \quad (\text{C.5})$$

# References

- BAHADUR, P., YADAV, P.S., CHAURSASIA, K., LEH, A. & TADMOR, R. (2009). Chasing drops: Following escaper and pursuer drop couple system. *J. Colloid Interface Sci.*, **332**, 455–460.
- BANGHAM, D.H. & SAWERIS, Z. (1938). The behaviour of liquid drops and adsorbed films at cleavage surfaces of mica. *Trans. Faraday Soc.*, **34**, 554–570.
- BECKER, J., GRÜN, G., SEEMANN, R., MANTZ, H., JACOBS, K., MECKE, K.R. & BLOSSEY, R. (2003). Complex dewetting scenarios captured by thin-film models. *Nat. Mater.*, **2**, 59–63.
- BIANCE, A.L., CLANET, C. & QUÉRÉ, D. (2004). First steps in the spreading of a liquid droplet. *Phys. Rev. E*, **69**, 016301.
- BIANCE, A.L., CHEVY, F., CLANET, G., C. LAGUBEAU & QUÉRÉ, D. (2006). On the elasticity of an inertial liquid shock. *J. Fluid Mech.*, **554**, 47–66.
- BICO, J., TORDEUX, C. & QUÉRÉ, D. (2001). Rough wetting. *Europhys. Lett.*, **55**, 214–220.
- BLAKE, T.D. & RUSCHAK, K.J. (1979). A maximum speed of wetting. *Nature*, **282**, 489–491.
- BOREYKO, J.B. & CHEN, C.H. (2009). Self-propelled dropwise condensate on superhydrophobic surfaces. *Phys. Rev. Lett.*, **103**, 184501.

## REFERENCES

---

- BORGAS, M.S. & GROTBORG, J.B. (1988). Monolayer flow on a thin film. *J. Fluid Mech.*, **193**, 151–170.
- BUTT, J.B., GRAF, K. & KAPPL, M. (2006). Physics and chemistry of interfaces. *Wiley*.
- CARLES, P. & CAZABAT, A.M. (1989). Spreading involving the marangoni effect: Some preliminary results. *Colloids Surf.*, **41**, 97–105.
- CASSIE, A.B.D. & BAXTER, S. (1944). Wettability of porous surfaces. *Trans. Faraday Soc.*, **40**, 546–551.
- CHANDRA, D. & YANG, S. (2011). Dynamics of a droplet imbibing on a rough surface. *Langmuir*, **27**, 13401–13405.
- CIRA, N.J., BENUSIGLIO, A. & PRAKASH, M. (2014). Dancing droplets: Autonomous surface tension-driven droplet motion. *Phys. Fluids*, **26**, 091113.
- CIRA, N.J., BENUSIGLIO, A. & PRAKASH, M. (2015). Vapour-mediated sensing and motility in two-component droplets. *Nature*, **519**, 446–450.
- CLANET, C., BÉGUIN, C., RICHARD, D. & QUÉRÉ, D. (2004). Maximal deformation of an impacting drop. *J. Fluid Mech.*, **517**, 199–208.
- COLLINS, R.T., JONES, J.J., HARRIS, M.T. & BASARAN, O.A. (2008). Electrohydrodynamic tip streaming and emission of charged drops from liquid cones. *Nature Phys.*, **4**, 149–154.
- COURBIN, L., DENIEUL, E., DRESSAIRE, E., ROPER, M., AJDARI, A. & STONE, H.A. (2007). Imbibition by polygonal spreading on microdecorated surfaces. *Nature Mater.*, **6**, 661–664.
- CUBAUD, T. & FERMIGIER, M. (2001). Faceted drops on heterogeneous surfaces. *Europhys. Lett.*, **55**, 239–245.
- CULICK, F.E.C. (1960). Comments on a ruptured soap film. *J. Appl. Phys.*, **31**, 1128–1129.

## REFERENCES

---

- DARHUBER, A.A., TROIAN, S.M., DAVIS, J.M., MILLER, S.M. & WAGNER, S. (2000). Selective dip-coating of chemically micropatterned surfaces. *J. Appl. Phys.*, **88**, 5119–5126.
- DARHUBER, A.A., TROIAN, M. & REISNER, W.W. (2001). Dynamics of capillary spreading along hydrophilic microstripes. *Physical Review E*, **64**, 031603.
- DAVIS, S.H. (1980). Moving contact lines and rivulet instabilities. part 1. the static rivulet. *J. Fluid Mech.*, **98**, 225–242.
- DE GENNES, P.G., BROCHARD-WYART, F. & QUÉRÉ, D. (2004). Capillarity and wetting phenomena: Drops, bubbles, pearls, waves. *Springer*.
- DE RYCK, A. & QUÉRÉ, D. (1996). Inertial coating of a fiber. *J. Fluid Mech.*, **311**, 219–237.
- DERJAGUIN, B.V. (1943). On the thickness of the liquid film adhering to the walls of a vessel after emptying. *Acta. Physicochim. USSR*, **20**, 349–352.
- DILLY, P.N. (1994). Lacrimal gland, tear film, and dry eye syndromes. *Springer US*.
- DUEZ, C., YBERT, C., CLANET, C. & BOQUET, L. (2007). Making a splash with water repellency. *Nature Phys.*, **3**, 180–183.
- EGGERS, J. (2004). Hydrodynamic theory of forced dewetting. *Phys. Rev. Lett.*, **93**, 094502.
- EHRHARD, P. (1993). Experiments on isothermal and non-isothermal spreading. *J. Fluid Mech.*, **257**, 463–483.
- GABRIELE, S., DAMMAN, P., SCLAVONS, S., DESPREZ, S., COPPÉE, S., REITER, G., HAMIEH, M., AKHRASS, S.A., VILMIN, T. & RAPHAËL, E. (2006). Viscoelastic dewetting of constrained polymer thin films. *J. Polym. Sci. Part B*, **44**, 3022–3030.

## REFERENCES

---

- GAVER, J.B., D. P. & GROTBURG (1990). The dynamics of a localized surfactant on a thin film. *J. Fluid Mech.*, **213**, 127–148.
- GOUCHER, F.S. & WARD, H. (1922). The thickness of liquid films formed on solid surfaces under dynamic condition. *Phil. Mag.*, **44**, 1002–1014.
- HABENICHT, A., OLAPINSKI, M., BURMEISTER, F., LEIDERER, P. & BONEBERG, J. (2005). Jumping nanodroplets. *Science*, **309**, 2043–2045.
- HOLLY, F.J. (1973). Formation and rupture of the tear film. *Exp. Eye Res.*, **15**, 515–525.
- HUANG, L., HUANG, Y., LIANG, J., WAN, X. & CHEN, Y. (2011). Graphene-based conducting inks for direct inkjet printing of flexible conductive patterns and their applications in electronic circuits and chemical sensors. *Nano Res.*, **4**, 675–684.
- HUPPERT, H.E. (1982). The propagation of two-dimensional and axisymmetric viscous gravity currents over a rigid horizontal surface. *J. Fluid Mech.*, **121**, 43–58.
- INCROPERA, F.P., DEWITT, D.P., L., B.T. & LAVINE, A.S. (2007). Fundamentals of heat and mass transfer. *John Wiley & Sons*.
- ISENBERG, C. (1992). The science of soap films and soap bubbles. *Dover*.
- ISHINO, C., REYSSAT, M., REYSSAT, E., OKUMURA, K. & QUÉRÉ, D. (2007). Wicking within forests of micropillars. *Europhys. Lett.*, **79**, 56005.
- JENSEN, O.E. & GROTBURG, J.B. (1992). Insoluble surfactant spreading on a thin viscous film: shock evolution and film rupture. *J. Fluid Mech.*, **240**, 259–288.
- JIN, H., MARMUR, A., IKKALA, O. & RAS, R.H.A. (2012). Vapour-driven marangoni propulsion: continuous, prolonged and tunable motion. *Chem. Sci.*, **3**, 2526–2529.

## REFERENCES

---

- JOHNSON, M.E. & MURPHY, P.J. (2004). Changes in the tear film and ocular surface from dry eye syndrome. *Progress in Retinal and Eye Research*, **23**, 449–474.
- JOKINEN, V., SAINIEMI, L. & FRANSSILA, S. (2008). Complex droplets on chemically modified silicon nanograss. *Adv. Mater.*, **20**, 3453–3456.
- KATAOKA, D.E. & TROIAN, S.M. (1999). Patterning liquid flow on the microscopic scale. *Nature (London)*, **402**, 794–797.
- KELLER, J.B. (1983). Breaking of liquid films and threads. *Phys. Fluids*, **26**, 3451–3453.
- KIM, H.S., KANG, J.S., PARK, J.S., HAHN, H.T., JUNG, H.C. & JOUNG, J.W. (2009). Inkjet printed electronics for multifunctional composite structure. *Compos. Sci. Technol.*, **69**, 1256–1264.
- KIM, H.Y., C., F.Z. & CHUN, J.H. (2000). Instability of a liquid jet emerging from a droplet upon collision with a solid surface. *Phys. Fluids*, **12**, 531–541.
- KIM, M.M.W.L.K.R.M.L..K.H.Y., J. (2011b). Hydrodynamics of writing with ink. *Phys. Rev. Lett.*, **107**, 264501.
- KIM, P., DUPRAT, C., TSAI, S.S.H. & STONE, H.A. (2011). Spreading and jetting of electrically driven dielectric films. *Phys. Rev. Lett.*, **107**, 034502.
- KIM, S., MOON, M.W. & KIM, H.Y. (2013). Drop impact on superwettability-contrast annular patterns. *J. Fluid Mech.*, **730**, 328–342.
- KIM, S.J., MOON, M.W., LEE, K.R., LEE, D.Y., CHANG, Y.S. & KIM, H.Y. (2011a). Liquid spreading on superhydrophilic micropillar arrays. *J. Fluid Mech.*, **680**, 477–487.
- KITAGAWA, K. (2013). Thin-film thickness profile measurement by three-wavelength interference color analysis. *Appl. Opt.*, **52**, 1998–2007.

## REFERENCES

---

- LANDAU, L. & LEVICH, B. (1942). Dragging of liquid by a plate. *Acta Physicochim URSS*, **17**, 42–54.
- LANDAU, L. & LEVICH, B. (1962). Physical hydrodynamics. *Prentice-Hall*.
- LEDESMA-AGUILAR, R., NISTAL, R., HERNÁNDEZ-MACHADO, A. & PAG-ONABARRAGA, I. (2011). Controlled drop emission by wetting properties in driven liquid filaments. *Nat. Mater.*, **10**, 367–371.
- LEE, A., MOON, M.W., LIM, H., KIM, W.D. & KIM, H.Y. (2012). Water harvest via dewing. *Langmuir*, **28**, 10183–10191.
- LEE, K.S. & STAROV, V.M. (2009). Spreading of surfactant solutions over thin aqueous layers at low concentrations: Influence of solubility. *J. Colloid Interface Sci.*, **329**, 361–365.
- LEE, M., CHANG, Y.S. & KIM, H.Y. (2010). Drop impact on microwetting patterned surfaces. *Phys. Fluids*, **22**, 072101.
- LI, R.Z., HU, A., ZHANG, T. & OAKES, K.D. (2014). Direct writing on paper of foldable capacitive touch pads with silver nanowire inks. *ACS Appl. Mater. Interfaces*, **6**, 21721–21729.
- LOPEZ, J. & MILLER, C.A. (1976). Spreading kinetics of liquid drops on solids. *J. Colloid Interface Sci.*, **56**, 460–468.
- LUGG, G.A. (1968). Diffusion coefficients of some organic and other vapors in air. *Anal. Chem.*, **40**, 1072–1077.
- MALEKI, M., REYSSAT, M., RESTAGNO, F., QUÉRÉ, D. & CLANET, C. (2011). Landau-levich menisci. *J. Colloid Interface Sci.*, **354**, 359–363.
- MATAR, O.K. & TROIAN, S.M. (1999a). Spreading of a surfactant monolayer on a thin liquid film: Onset and evolution of digitated structures. *Chaos*, **9**, 141–153.

## REFERENCES

---

- MATAR, O.K. & TROIAN, S.M. (1999b). The development of transient fingering patterns during the spreading of surfactant coated films. *Phys. Fluids*, **11**, 3232–3246.
- MITLIN, V.S. (1993). Dewetting of solid surface: Analogy with spinodal decomposition. *J. Colloid Interface Sci.*, **156**, 491–497.
- ONDA, T., SHIBUICHI, S., SATOH, N. & TSUJII, K. (1996). Super-water-repellent fractal surfaces. *Langmuir*, **12**, 2125–2127.
- PADDAY, J.F. (1970). Cohesive properties of thin films of liquids adhering to a solid surface. *Spec. Discuss. Faraday Soc.*, **1**, 64–74.
- PÉRON, N., BROCHARD-WYART, F. & DUVAL, H. (2012). Dewetting of low-viscosity films at solid/liquid interfaces. *Langmuir*, **28**, 15844–15852.
- PRATT, K.C. & WAKEHAM, W.A. (1975). The mutual diffusion coefficient for binary mixtures of water and the isomers of propanol. *Proc. R. Soc. London, Ser. A*, **342**, 401–419.
- QUÉRÉ, D. (1999). Fluid coating on a fiber. *Annu. Rev. Fluid Mech.*, **31**, 347–384.
- QUÉRÉ, D. (2008). Wetting and roughness. *Annu. Rev. Mater. Res.*, **38**, 71–99.
- REDON, C., BROCHARD-WYART, F. & RONDELEZ, F. (1991). Dynamics of dewetting. *Phys. Rev. Lett.*, **66**, 716–718.
- REIN, M. (1993). Phenomena of liquid drop impact on solid and liquid surfaces. *Fluid Dyn. Res.*, **12**, 61–93.
- REITER, G. (1992). Dewetting of thin polymer films. *Phys. Rev. Lett.*, **68**, 75–78.
- REYSSAT, M., PARDO, F. & QUÉRÉ, D. (2009). Drops onto gradients of texture. *Europhys. Lett.*, **87**, 36003.

## REFERENCES

---

- RICHARD, D. & QUÉRÉ, D. (2000). Bouncing water drops. *Europhys. Lett.*, **50**, 769–775.
- RIOBOO, V.M.V.A..D.C.J., R. (2008). Drop impact on porous superhydrophobic polymer surfaces. *Langmuir*, **24**, 14074–14077.
- ROTH, E.A., XU, T., DAS, M., GREGORY, C., HICKMAN, J.J. & BOLAND, T. (2004). Inkjet printing for high throughput cell patterning. *Biomaterials*, **25**, 3707–3715.
- RUSSO, A., AHN, B.Y., ADAMS, J.J., DUOSS, E.B., BERNHARD, J.T. & LEWIS, J.A. (2011). Pen-on-paper flexible electronics. *Adv. Mater.*, **23**, 3426–3430.
- SBRAGAGLIA, M., PETERS, A.M., PIRAT, C., BORKENT, B.M., LAMMERTINK, R.G.H., WESSLING, M. & LOHSE, D. (2007). Spontaneous breakdown of superhydrophobicity. *Phys. Rev. Lett.*, **99**, 156001.
- SCHIAFFINO, S. & SONIN, A.A. (1997). Formation and stability of liquid and molten beads on a solid surface. *J. Fluid Mech.*, **343**, 95–110.
- SEIWERT, J., CLANET, C. & QUÉRÉ, D. (2011). Coating of a textured solid. *J. Fluid Mech.*, **669**, 55–63.
- SHARMA, A. & RUCKENSTEIN, E. (1989). Dewetting of solids by the formation of holes in macroscopic liquid films. *J. Colloid Interface Sci.*, **133**, 358–368.
- SHIN, B., LEE, K.R., MOON, M.W. & KIM, H.Y. (2012). *Soft Matter*, **8**, 1817–1823.
- TANNER, H., L (1979). The spreading of silicone oil drops on horizontal surfaces. *J. Phys. D.: Appl. Phys.*, **12**, 1473–1484.
- TAYLOR, G.I. (1959). The dynamics of thin sheets of fluid. iii. disintegration of fluid sheets. *Proc. R. Soc. London. Ser. A.*, **253**, 313–321.

## REFERENCES

---

- TAYLOR, G.I. & MICHAEL, D.H. (1973). On making holes in a sheet of fluid. *J. Fluid Mech.*, **58**, 625–639.
- TELETZKE, G., DAVIS, H.T. & SCRIVEN, L.E. (1988). Wetting hydrodynamics. *Rev. Phys. Appl.*, **23**, 989–1007.
- TROIAN, S.M., HERBOLZHEIMER, E. & SAFRAN, S.A. (1990). Model for the fingering instability of spreading surfactant drops. *Phys. Rev. Lett.*, **65**, 333–336.
- TSAI, P., PACHECO, S., PIRAT, C., LEFFERTS, L. & LOHSE, D. (2009). Drop impact upon micro- and nanostructured superhydrophobic surfaces. *Langmuir*, **25**, 12293–12298.
- WARNER, M.R.E., CRASTER, R.V. & MATAR, O.K. (2004). Fingering phenomena associated with insoluble surfactant spreading on thin liquid films. *J. Fluid Mech.*, **510**, 169–200.
- WASHBURN, E.W. (1921). The dynamics of capillary flow. *Phys. Rev.*, **17**, 273–283.
- WENZEL, R.N. (1936). Resistance of solid surfaces to wetting by water. *Ind. Eng. Chem.*, **28**, 988–994.
- WORTHINGTON, A.M. (1877). On the forms assumed by drops of liquid falling on a horizontal plate. *Proc. R. Soc. London*, **25**, 261–272.
- YARIN, A.L. (2006). Drop impact dynamics: Splashing, spreading, receding, bouncing.. *Annu. Rev. Fluid Mech.*, **38**, 159–192.
- ZHANG, Z.Y.Y.B..F.Q., Y. (2011). Nanolitre droplet array for real time reverse transcription polymerase chain reaction. *Lab Chip*, **11**, 1545–1549.
- ZHAO, B., MOORE, J.S. & BEEBE, D.J. (2001). Surface-directed liquid flow inside microchannels. *Science*, **291**, 1023–1026.

# 국 문 초 록

## 계면 에너지 구배로 발생하는 얇은 액막 역학에 대한 연구

서울대학교 대학원

기계항공공학부

김 승 호

### 요 약

본 연구에서는 고체 표면 위에서 계면 에너지 구배로 발생하는 얇은 액막의 거동에 대한 유체역학적 해석 연구를 수행하였다. 이러한 계면 에너지 구배는 고체 표면의 적심성을 패터닝하거나 액체 표면의 마랑고니 스트레스를 유발하여 얻을 수 있는데, 본 연구에서는 이를 통해 고체 표면 위에 놓여진 액막의 형상을 제어할 수 있을 뿐 아니라, 액막 파열, 폴짐, 후퇴에 대한 새로운 액막 유동 양상을 발견할 수 있었고 이를 실험과 이론을 접목하여 해석하는 연구를 수행하였다.

먼저, 한 고체 표면에 이종의(친수, 소수) 적심성이 특정 형상으로 패터닝 된 표면에 대한 액막 거동 연구를 수행하였다. 친수성이 개곡선 형태로 패터닝 된 표면에 액적 충돌 시, 액체는 친수, 소수성 영역의 고체-액체 계면 에너지 높은 차이로 인해 고체-액체 계면 에너지가 낮은 친수성 영역에만 선택적으로 도포되는 데 반해, 친수

성이 폐곡선 형태로 패터닝 된 표면에서는 액체의 접촉선이 친수한 폐곡선 영역에 고정되어 폐곡선 안 쪽 소수성 영역까지 액체가 덮여 얇은 액막이 형성됨을 발견하였다. 본 연구에서는 소수성 고체 표면과 액체 계면에서 발생하는 강한 반발력을 이용하여 소수성 영역 위 액막의 자발적인 파열을 유도하였고, 이를 통해 친수성 영역에만 액막을 선택적으로 도포하는 메커니즘을 개발하였다. 관찰된 결과를 바탕으로 기존에 보고되지 않은 액막의 형성, 파괴 및 후퇴 현상에 대한 검증된 이론 모델을 제공하였으며, 다양한 형태의 친수 폐곡선 형상에도 적용 가능함을 보였다.

다음으로, 적심성 패턴 표면에 대해 액체의 공급 방법을 변경하여 액막의 형상을 제어하는 연구를 수행하였고, 액체를 친수 영역에 살짝 닿게 해주어도 액막이 친수성 영역을 따라 전진하여 전체 친수성 곡선에 액막이 패터닝 됨을 알 수 있었다. 하지만, 친수 곡선의 폭이 작아질 경우, 액막의 퍼짐 속도가 지연되는 것을 알 수 있었고, 이에 대한 원천 연구를 수행하고자 본 연구에서는 친수성이 직선으로 패터닝 된 고체 표면에 대한 액막 퍼짐 연구를 집중적으로 수행하였다. 친수 직선 폭이 작을 경우, 좁은 폭으로 발생하는 높은 저항력으로 인해 액막이 두껍게 코팅되지 않고 고체 표면의 나노사이즈의 요철을 따라 굉장히 얇은 액막이 코팅되는 반면 친수 직선 폭이 클 경우, 나노요철 높이의 수십 수백배 이상의 두꺼운 액막이 코팅되는 것을 발견하였다. 또한 두꺼운 액막 퍼짐은 얇은 액막 퍼짐과 다르게 퍼짐 거리와 시간 관계에 다양한 역할수가 존재한다는 것을 알 수 있었다. 본 연구에서는 얇은 액막 유동에서 일반적으로 고려하는 모세관 힘, 접성력 외에 관성력을 고려하여 친수 직선 폭에 따라 액막의 퍼짐 양상 및 속도에 대한 스케일링 모델을 제시하

였고, 이를 실험적으로 검증하였다.

마지막으로, 표면장력 구배 하에 거동하는 액막에 대한 유체역학적 해석 연구를 수행하였다. 본 연구에서는 알코올의 증기를 이용하여 비접촉식으로 기체-액체 계면장력을 제어하는 방법을 발견하였고, 이를 통해 적심성이 균일한 표면 위에 놓여진 액막에 원격으로 홀을 패터닝하는 메커니즘을 개발하였다. 홀 생성은 액막 후퇴 현상에 따른 산물로, 얇은 액막 영역에서는 후퇴하는 액막 두께에 따라 두 가지 다른 후퇴 양상을 관측하였다. 여기서는 얇은 액막 중 상대적으로 두께가 두꺼운 액막이 먼저 후퇴하고, 고체 표면 위에 남겨진 나노스케일의 두께가 얇은 액막이 연달아 후퇴하는 현상을 관측하였다. 두꺼운 액막 영역에서는 단일한 액막이 후퇴하는 현상을 보였지만, 얇은 액막과는 다르게 홀의 크기가 계속 커지지 않고 어느 한계까지만 성장하는 현상을 관측하였다. 액막에 비접촉식으로 홀을 패터닝하는 것은 기존에 보고되지 않은 현상으로, 본 연구에서는 얇은 액막과 두꺼운 액막에서 성장하는 홀의 사이즈 및 두꺼운 액막의 최대 크기에 대한 스케일링 모델을 제시하고 실험으로 검증하는 연구를 수행하였다.

본 연구에서는 액체-고체, 액체-기체의 계면 에너지 구배 하에 거동하는 액막의 새로운 운동 양상을 발견 및 해석하였다. 이를 통해 고체 표면 위에 놓여진 액막의 형상을 원하는 대로 도포하거나 홀을 패터닝하고 크기 역시 제어할 수 있었다. 본 연구를 확장하여 나노입자 서스펜션, 실버 페이스트 등의 기능성 액체를 고체 표면 위에 직접 프린팅 또는 패터닝 할 수 있다면, 기존 잉크젯 기반 기술에 국한된 인쇄전자산업에 새로운 활력을 제공할 수 있을 것이라

기대한다. 또한, 본 연구에서 개발한 이론 모델은 체내에서 외부 오염입자를 막는 데 중요한 역할을 하는 눈물막과 점액막의 유지 및 거동해석에 적용될 수 있을 것이라 기대한다.

주요어 : 얇은 액막, 모세관, 계면 장력, 마랑고니, 흘, 액막 파열, 적심, 후퇴, 퍼짐

학 번 : 2010 - 20659